Slim Naifar

Model Based Design of a Magnetoelectric Vibration Converter from Weak Kinetic Sources

Scientific Reports on Measurement and Sensor Technology

Volume 9

Prof. Dr.-Ing. Olfa Kanoun (Editor)

Slim Naifar

Model based Design of a Magnetoelectric Vibration Converter from Weak Kinetic Sources

TECHNISCHE UNIVERSITÄT
CHEMNITZ

Universitätsverlag Chemnitz
2019

Impressum

Bibliografische Information der Deutschen Nationalbibliothek

Die Deutsche Nationalbibliothek verzeichnet diese Publikation in der Deutschen Nationalbibliografie; detaillierte bibliografische Angaben sind im Internet über `http://www.dnb.de` abrufbar.

Titelgrafik: Chemnitz School of Metrology
Satz/Layout: Slim Naifar

Technische Universität Chemnitz/Universitätsbibliothek
Universitätsverlag Chemnitz
09107 Chemnitz
`https://www.tu-chemnitz.de/ub/univerlag`

readbox unipress
in der readbox publishing GmbH
Am Hawerkamp 31
48155 Münster
`http://unipress.readbox.net`

ISSN 2509-5102 print - ISSN 2509-5110 online

ISBN 978-3-96100-079-1

`http://nbn-resolving.de/urn:nbn:de:bsz:ch1-qucosa2-327748`

TECHNISCHE UNIVERSITÄT
CHEMNITZ

Model based Design of a Magnetoelectric Vibration Converter from Weak Kinetic Sources

von der Fakultät für Elektrotechnik und Informationstechnik der
Technischen Universität Chemnitz

genehmigte

Dissertation

zur Erlangung des akademischen Grades

Doktor-Ingenieur
(Dr.-Ing.)

vorgelegt von
M.Sc. Dipl.-Ing. Slim Naifar
geboren am 30. Oktober 1988 in Sfax, Tunesien

Gutachter: Prof. Dr.-Ing. Olfa Kanoun (Technische Universität Chemnitz)
Prof. Dr.-Ing. Jörg Himmel (Hochschule Ruhr-West)
Prof. Dr.-Ing. Tarak Bouraoui (Universität Monastir)

Tag der Einreichung: 08. Oktober 2018
Tag der Verteidigung: 19. Dezember 2018

Acknowledgments

The work presented in this dissertation was carried out during my work as a research assistant in the chair for Measurement and Sensor Technology (MST) at Chemnitz University of Technology.

My special thanks are due:

- Prof. Olfa Kanoun, my supervisor at Chemnitz University of Technology, Germany, for providing me the opportunity to pursue my research towards completion of this Ph.D. dissertation. Without her support, motivation and patience, I would never have been able to achieve a work of this quality,
- Prof. Slim Choura, my supervisor at National Engineering School of Sfax (ENIS), Tunisia, for his generous support and patience,
- All my colleagues in the energy autonomous systems working group at MST, especially Bilel Kallel, Sonia Bradai, Issam Chaour, Dr. Christian Viehweger, Martin Götz, Sabrine Kheriji, Dhouha el Hussaini and Ghada Bouattour. They provided a friendly and cooperative atmosphere and also useful feedback and insightful comments on my work,
- All my Ph.D. colleagues for the stimulating discussions and for all the time that we shared together. Very special thanks to Prof. Carlo Trigona, University of Catania, Italy, who was very inspiring to me. Thanks are extended to all the people who contributed in some way to the work described in this thesis.

Last but not the least, I would like to thank my family. I am deeply indebted to my parents for their support and continuous encouragement throughout my years of study. This dissertation stands as a symbol to their unconditional support and encouragement. I thank my lovely wife Ayda Bouhamed for the technical discussions, but even more for her constant encouragement and patience. Thanks to my daughter, the pride and joy of my life, which made me stronger, better and more fulfilled than I could have ever imagined. Thanks are extended to my brother Mohamed Amine and my sister Souhir for supporting me spiritually throughout writing this thesis and my life in general.

Financial support from the German Academic Exchange Service (DAAD), the exchange program InProTUC, the BMBF project "HydroMon" and the AIF-ZIM project "Sensorschraube" are gratefully acknowledged.

Abstract

The main challenge in the design of vibration energy harvesters is the optimization of energy outcome relative to the applied excitation to reach a higher efficiency in spite of the weakness of ambient energy sources. One promising principle of vibration converters is magnetoelectricity due to the outstanding properties of magnetostrictive and piezoelectric laminate composites, which provide interesting possibilities to harvest energy from low amplitude and low frequency vibration with relatively high energy outcome. For these devices, ensuring high deformations in the magnetostricive layers, improvement of the magnto-mechanical and the electro-mechanical couplings are highly required for the optimization of the energy outcome.

This thesis primarily aims to develop a model based harvester design for magnetoelectric (ME) converters. Based on a comprehensive understanding of the complex energy flow in magnetoelectric transducers, several design parameters are investigated.

For instance, magnetostriction in a Terfenol-D plate is investigated by means of atomic force microscopy under similar conditions as within magnetoelectric transducers. A novel measurement approach was successfully developed to detect the evolution of magnetic domains and measure deformations in a Terfenol-D plate in response to externally non-uniform applied magnetic fields.

Furthermore, a finite element model is developed to predict the induced voltage in the ME transducer as a response to the magnet's displacement, corrected based on atomic force microscopy measurements, and used for the design of the harvester. The presented three- dimensional model takes into consideration the nonlinear behaviour of the magnetostrictive and piezoelectric materials. Additionally, three novel converters having different magnetic circuits are designed and analysed analytically based on Lindstedt-Poincaré method. The effects of the structure parameters, such as the nonlinear magnetic forces, the magnetic field distribution and the resonance frequency are discussed, and the electric output performances of the three designed converters are evaluated.

In order to improve both mechanical and electrical coupling between the piezoelectric and the magnetostrictive layers, a bonding technique at room temperature is proposed which uses conductive polymer nanocomposites. Two magnetoelectric transducers are fabricated based on this technique having 1 wt.% and 2 wt.% concentration of multiwalled carbon nanotubes in epoxy resin. Another magnetoelectric transducer is fabricated by a classical technique for comparison purposes.

In order to validate the design, a series of demonstrators are designed and fabricated according to the simulation and optimization results. The proposed design is composed by a cantilever beam, a magnetic circuit with several magnet arrangements and a magnetoelectric transducer, which is formed by a piezoelectric PMNT plate bonded to two magnetostrictive Terfenol-D layers. In this design, external vibrations are converted to magnetic field changes acting on the magnetostrictive layers leading to deformations, which are transmitted directly to the piezoelectric layer.

The converters are tested under harmonic excitations and real vibration profiles reproduced by an artificial vibration source. Different parameters were investigated experimentally including the magnetic forces between the transducer and the magnetic circuit and the used bonding technique. Tuning the resonance frequency of the ME converter is also addressed using a simple screw/nut system, which allows to control the relative position and therefore the magnetic forces between the magnetic circuit and the transducer.

The magnetoelectric transducer bonded with 2 wt.% concentration of multiwalled carbon nanotubes shows better output performances than the two other ME transducers under similar excitations. A maximum power output of 2.42 mW is reached under 1 mm applied vibration at 40 Hz. This performance presents an improvement of minimum 20 % of the reached energy outcome by other magnetoelectric vibration converters using single ME transducer at comparable applied excitations.

Title: Model based Design of a Magnetoelectric Vibration Converter from Weak Kinetic Sources

Keywords: Energy harvesting, Magnetoelectric effect, Magnetostriction, Piezoelectric effect, Laminate composite

Kurzfassung

Die größte Herausforderung bei der Konstruktion von Vibrations-Energiewandlern ist die Optimierung der gewonnenen Energie im Verhältnis zur angewandten Anregung, um trotz schwacher Umgebungsenergiequellen einen hohen Wirkungsgrad zu erreichen. Ein vielversprechendes Prinzip von Vibrationswandlern ist die Magnetoelektrizität aufgrund der hervorragenden Eigenschaften von magnetostriktiven und piezoelektrischen Verbundwerkstoffen, die interessante Möglichkeiten bieten, Energie aus niederfrequenten Schwingungen mit kleinen Amplituden zu gewinnen. Bei diesen Wandlern ist die Sicherstellung hoher Verformungen in den magnetostriktiven Schichten, die Verbesserung der magnetisch-mechanischen und der elektro-mechanischen Kopplungen für die Optimierung des Energieertrages sehr wichtig.
Diese Arbeit zielt in erster Linie auf die Entwicklung eines modellbasierten Entwurfs für magnetoelektrische (ME) Wandler ab. Basierend auf einem umfassenden Verständnis des komplexen Energieflusses in magnetoelektrischen Wandlern werden mehrere Entwurfsparameter untersucht.
So wird beispielsweise die Magnetostriktion in einer Terfenol-D-Platte mittels Rasterkraftmikroskopie unter ähnlichen Bedingungen untersucht wie in magnetoelektrischen Wandlern. Dabei wurde eine neuartige Messmethode erfolgreich entwickelt, um die Entwicklung von magnetischen Domänen zu erfassen und die Deformation in einer Terfenol-D-Platte als Reaktion auf extern ungleichmäßig angelegte Magnetfelder zu messen. Darüber hinaus wird ein Finite-Elemente-Modell entwickelt, um die induzierte Spannung im ME-Wandler als Reaktion auf die Verschiebung des Magneten vorherzusagen, welches auf der Grundlage von Atomkraftmikroskopie Messungen korrigiert und für den Entwurf des Energiewandlers verwendet wird. Das vorgestellte dreidimensionale Modell berücksichtigt das nichtlineare Verhalten der magnetostriktiven und piezoelektrischen Materialien. Zusätzlich werden drei neuartige Wandler mit unterschiedlichen Magnetkreisen nach dem Lindstedt-Poincaré Verfahren konzipiert und analytisch analysiert. Die Auswirkungen der Strukturparameter, wie die nichtlinearen Magnetkräfte, die Magnetfeldverteilung und die Resonanzfrequenz, werden diskutiert und die elektrischen Ausgangsleistungen der drei ausgelegten Wandler ausgewertet.
Um die mechanische und elektrische Kopplung zwischen der piezoelektrischen und der magnetostriktiven Schicht zu verbessern, wird eine bei Raumtemperatur prozessierbare Verbindungstechnik vorgeschlagen, bei der leitfähige Nanokomposite verwendet werden. Zwei magnetoelektrische Wandler werden basierend auf dieser Technik mit einer Konzentration von 1 wt.% und 2 wt.% an mehrwandigen Kohlenstoff-Nanoröhren in Epoxidharz hergestellt. Ein weiterer magnetoelektrischer Wandler wurde zu Vergleichs-

zwecken mit einer klassischen Technik hergestellt. Für die Validierung des Entwurfes wird eine Reihe von Demonstratoren entsprechend den Simulations- und Optimierungsergebnissen konstruiert und gefertigt. Der vorgeschlagene Entwurf besteht aus einem Trägerbalken, einem Magnetkreis mit mehreren Magnetanordnungen und einem magnetoelektrischen Wandler, der aus einer piezoelektrischen PMNT-Platte besteht, die mit zwei magnetostriktiven Terfenol-D-Schichten verbunden ist. Bei dieser Konstruktion werden externe Schwingungen in Magnetfeldänderungen umgewandelt, die auf die magnetostriktiven Schichten wirken und zu Verformungen führen, die direkt auf die piezoelektrische Schicht übertragen werden.

Die Wandler werden unter harmonischen Anregungen und mit realen Schwingungsprofilen getestet, die von einer künstlichen Schwingungsquelle reproduziert werden. Verschiedene Parameter wurden experimentell untersucht, darunter die magnetischen Kräfte zwischen dem Wandler und dem Magnetkreis sowie die verwendete Verbindungstechnik. Die Abstimmung der Resonanzfrequenz des ME-Wandlers erfolgt ebenfalls über ein einfaches Schrauben-Mutter-System, das es ermöglicht, die relative Position und damit die magnetischen Kräfte zwischen Magnetkreis und Wandler zu steuern.

Der magnetoelektrische Wandler, der mit einer Konzentration von 2 wt.% mehrwandiger Kohlenstoff-Nanoröhrchen verbunden ist, zeigt bessere Ausgangsleistungen als die beiden anderen ME-Wandler bei ähnlichen Anregungen. Eine maximale Ausgangsleistung von 2,42 mW wird bei 1 mm angelegter Vibration bei 40 Hz erreicht. Diese Leistung stellt eine Verbesserung von mindestens 20 % im Vergleich zu anderen magnetoelektrischen Schwingungsumrichtern dar, welche mit einem einzigen ME-Wandler bei vergleichbaren Anregungen getestet werden.

Titel: Modellbasierter Entwurf eines magnetoelektrischen Schwingungswandlers aus schwachen kinetischen Quellen

Schlagwörter: Energiegewinnung, Magnetoelektrischer Effekt, Magnetostriktion, Piezoelektrischer Effekt, Laminat-Verbundwerkstoffe

Contents

List of abbreviations and symbols

List of abbreviations

AC	**A**lternating **C**urrent
AFM	**A**tomic **F**orce **M**icroscopy
CNTs	**C**arbon **N**ano**T**ubes
DoF	**D**egree **o**f **F**reedom
FUF	**F**atigue **U**sage **F**actor
FE	**F**inite **E**lement
L-T	**L**ongitudinal-**T**ransversal
L-L	**L**ongitudinal-**L**ongitudinal
ME	**M**agneto**E**lectric
Ms	**M**agneto**S**trictive
MsM	**M**agneto**s**trictive **M**aterial
MWCNTs	**M**ulti-**W**alled **C**arbon**N**anotubes
PE	**P**iezo**E**lectric
Pk-Pk	**P**eak to **P**eak
PMNT	Lead **M**agnesium **N**iobate **T**itanate
PUC	**P**iezoelectric **U**nimorph **C**antilever
SEM	**S**canning **E**lectctron **M**icroscopy
SWCNTs	**S**ingle-**W**alled **C**arbon**N**anotubes
PZT	Lead **Z**irconate **T**itanatee
RMS	**R**oot **M**ean **S**quare
T-L	**T**ransversal-**L**ongitudinal
T-T	**T**ransversal-**T**ransversal
VFM	**V**ariable **F**ield **M**odule
WSNs	**W**ireless **S**ensor **N**etworks

List of symbols

Character	Designation	Unit
a	distance	m
a_c	acceleration	m s^{-2}
B	magnetic flux density	T
B_a	alternating B	T
B_u	average induced B in the two Ms layers	T
B_l	induced B in lower Ms layer	T
B_t	induced B in upper Ms layer	T
B_{rms}	B_a root mean square	T
B_s	static B	T
b_c	width of the cantilever beam	m
C	capacitance	F
c	damping force factor	N s m^{-1}
c^E	elasticity matrix	Pa
C_{ME}	Magnetoelectric coupling coefficient	-
D	electric field displacement	C m^{-2}
d_c	strain-charge coupling matrix	C N^{-1}
E	electric field	N C^{-1} or V m^{-1}
E_m	Young's modulus of the magnetostrictive material	Pa
E_p	Young's modulus of the piezoelectric material	Pa
E_c	Young's modulus of the beam material	Pa
e_c	stress-charge coupling matrix	C m^{-2}
f	frequency	Hz
f_v	volume fraction	
F_c	viscous damping force	N
F_m	interaction force	N
h	position	m
h_c	thickness of the cantilever beam	m
H	magnetic field	A m^{-1} or $\pi 10^{-3}$ Oe
I_c	second moment of area	m^4
k_f	correction factor	-
k_{mc}	ME additional stiffness amplitude	N m^{-1}
k_c	stiffness of the cantilever beam	N m^{-1}
l_c	length of the cantilever beam	m
m	equivalent mass	kg
m_c	mass of the cantilever	kg
M_t	mass of the ME transducer	kg

M	magnetization	A m^{-1}
M_i	magnetization along i	A m^{-1}
p	excitation force	N
P	power	W (Js^{-1})
P_{max}	maximum power	W
P_0	vibration acceleration amplitude	m s^{-2}
P_o	polarisation	C m^{-2}
R	stress ratio	-
R_{eq}	equivalent resistance	$\mathit{\Omega}$
R_L	load resistance	$\mathit{\Omega}$
V	voltage	V
V_0	open circuit voltage	V
V_{eff}	effective voltage	V
z	displacement	m
α_{ME}	magnetoelectric voltage coefficient	V m^{-1} Oe
α_j	magnetization direction cosine	-
ϵ	strain	-
ϵ_p^ϵ	permittivity matrix	F m^{-1}
ϵ_r	relative permittivity	-
$\eta(z)$	arbitrary function of z	-
θ	angle of magnetization	rad
λ	magnetostriction	-
λ_f	ME coefficient adjustment factor	-
λ_s	saturation magnetostriction	-
λ_{kij}	saturation magnetization along <kij>	A m^{-1}
φ_m	coupling factor	-
ν_m	Poisson's ratio of the magnetostritive material	-
ν	Poisson's ratio of the piezoelectric material	-
ϖ	angular frequency	rad s^{-1}
ω_c	angular frequency of the cantilever	rad s^{-1}
ρ_m	density of the magnetostrictive layer	kg m^{-3}
ρ_p	density of the piezoelectric layer	kg m^{-3}
ϱ	electrical conductivity	S m^{-1}
σ	stress	Pa
σ_a	alternating stress	Pa
σ_m	mean stress	Pa
σ_{max}	maximum stress	Pa
σ_{min}	minimum stress	Pa

Physical constants

Gravitational acceleration	g	$=$	9.81	ms^{-2}
Vacuum permittivity	ϵ_0	$=$	8.854187817	Fm^{-1}
Vacuum permeability	μ_0	$=$	$4\pi 10^{-7}$	NA^{-2}

CHAPTER 1

Introduction

1.1 Motivation

The development of low-power electronic devices has reduced power requirements for wireless sensor networks (WSNs), which opens the possibility to develop self-powered autonomous systems supplied from available environmental resources [1, 2]. Powering WSNs directly from ambient energy allows their wide use in many industrial and civilian application areas such as transportation, home automation and internet of things [3, 4]. Batteries can be omitted, and sensor installation becomes very easy by a simple configuration. Among many available environmental sources, ambient vibration is promising because of its availability and the relative high level of energy which can be reached [5]. It has the advantage of small size in comparison with other energy harvesting techniques [6]. In addition, kinetic energy often exists in form of displacements, vibration and forces in moving structures such us air-planes and trains, in most machines and in structures such as bridges and buildings. Diverse transduction mechanisms have been exploited to convert mechanical motion into electrical energy including piezoelectric [7], electromagnetic [8], magnetoelectric (ME) [9], and electrostatic transducers [10].

Integration of materials to harvest energy from low vibration sources for powering wireless sensor networks has been of significant interest and still is [11, 12]. Giant magnetostrictive materials, such as Terfenol-D can realize mechanical deformations up to 2000 ppm and can be therefore interesting for low amplitude vibration [13]. Owing to large displacements and energy density of Terfenol-D, the use of piezoelectric/Terfenol-D composites exhibit great potential for the realization of vibration converters. Most recently, the possibility of using laminate composites formed by magnetostrictive and piezoelectric layers to convert magnetic to electrical energy, has attracted attention when compared to other transduction mechanisms [14].

ME transducers are specially important because they are able to produce higher mechanical stress and power output than piezoelectric cantilever beam generators [15]. For these reasons, ME transducers can significantly contribute to innovations in the field of vibration converters due to their outstanding properties. Nevertheless, there is still need for more efforts aiming to enhance the energy harvesting performance of magnetoelectric composite harvesters in terms of reached output power, converter bandwidth, and robustness. Especially at low frequencies and for low excitation amplitudes, the power outcome has to be enough to ensure the working energy of the wireless sensor.

The transduction mechanism of ME vibration energy harvesting is shown in Figure 1.1.

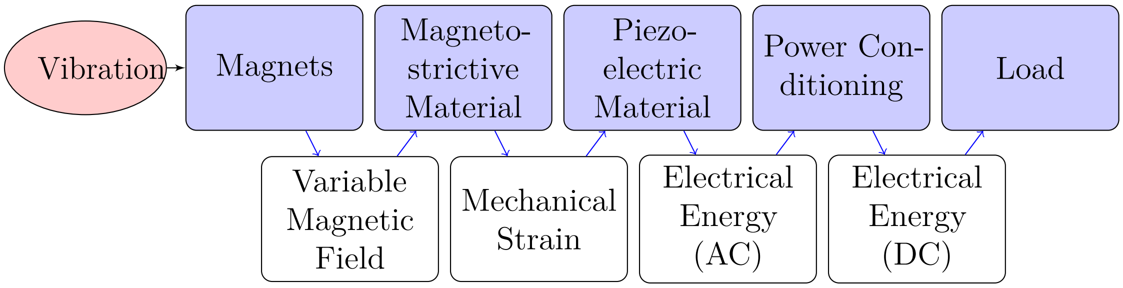

Figure 1.1: Block diagram of magnetoelectric energy harvesting system for autonomous sensors

1.2 Problem statement

In spite of the promising properties of ME transducers formed by magnetostrictive/piezoelectric laminate composites, these materials are highly non-linear and therefore difficult to control. There are still several unsolved problems for the design of magnetoelectric converters. In fact, many interacting effects are presented in these converters, which influence their performance.

In ME converters, the conversion of mechanical energy to electric energy is done based on the magnetoelectric effect as a composite effect in magnetostrictive and piezoelectric materials. The first interacting effect is magnetostriction, which is defined as the change of the shape of the material when it is subjected to a magnetic field. To achieve high output power, it is necessary to have high magnetostriction. This would not be possible without ensuring a good magneto-mechanical coupling between the magnets and the magnetostrictive material. In spite of numerous developed ME converters, a comprehensive understanding of the conduction mechanism of magnetostrictive/piezoelectric laminate composites under different magnetic fields is still lacking. To that end, the induced deformation in the MS layer has to be characterized in function of the magnetic field distribution which serve for the design of an appropriate magnetic circuit.

Additionally, the bonding of the three layers has been a big challenge in the design of ME converters. Since the voltage output is generated by the piezoelectric layer and collected from the two Terfenol-D layers, the adhesive layer has a decisive role to transmit high deformations to the PE layer and to conduct the electrical energy generated by the same layer. Thus, it is highly needed to ensure an excellent electro-mechanical coupling between the PE and the MS layers. Consequently, investigation of the ME transducers performance with different bonding adhesives is required. Furthermore, the transmission mechanism of external vibration has a great importance and may make the converter able to harvest energy from low kinetic sources.

1.3 Thesis objectives and focus

The focus of this thesis is to develop a model based harvester design for a ME converter, which is formed by magnetostrictive and piezoelectric materials.
The primary objective is to characterize magnetostrictive effect of the giant magnetostrictive material, Terfenol-D, under similar conditions as it is used in ME transducers. Thus, measurement of the induced deformation in the Terfenol-D layer should be carried out and correlated to the applied magnetic field. Furthermore, this research aims to develop a simulation model for the magnetoelectric effect in the transducer, which relates the magnetic field variation and the output voltage from the piezoelectric layer. Another objective of this thesis is to investigate the influence of the epoxy resin and its composition on the ME transducer performance. This thesis aims also to evaluate the use of ME converter under ambient vibration.

1.4 Thesis overview

The thesis is structured in seven chapters (Figure 1.2).
In **Chapter 1**, the motivation of using magnetoelectric transducers for vibration energy harvesting is described. This chapter introduces the problem statement, main objectives and focus of the thesis.
Chapter 2 presents an overview of the basic physical principles behind the magnetoelectric effect. Specifically, magnetostrictive and piezoelectric effects are described in detail with focus on laminate composites used in magnetoelectric energy harvesting. In addition, materials, which exhibit these effects are discussed.
In **Chapter 3**, a literature review on recent progress in piezoelectric and magnetoelectric vibration converters is presented. The reported devices are classified according to their coupling architecture, and their energy outcome are discussed. A novel approach for designing magnetoelectric converters is presented. This approach is based on four main elements, which are; investigation of magnetostriction, modelling of ME effect, design of the magnetic circuit, and investigation of the bonding adhesive.
Chapter 4 is devoted to the measurement of the deformation in a Terfenol-D plate under similar conditions as it is used in magnetoelectric converters by means of atomic force microscopy. The magnetic field distribution is studied by finite element analysis and the correlation between measured deformation and corresponding magnetic field parameters are discussed for different scenarios.
In **Chapter 5**, a finite element model to predict the induced voltage in the ME transducer as response to the magnets displacement is developed, corrected based on atomic force investigations, and used for the design of the harvester. The proposed design is analysed analytically and based on finite element analysis. The effects of the structure parameters such as the non-linear magnetic forces, the magnetic field distribution, and the resonance frequency are discussed, and the electric output performances of the transducer are evaluated.
Chapter 6 deals with the experimental investigations of the harvester with an artificial vibration source under harmonic excitations and real measured vibration profiles.

Chapter 7 summarizes the main results of this work. In addition, conclusions and future trends are provided.

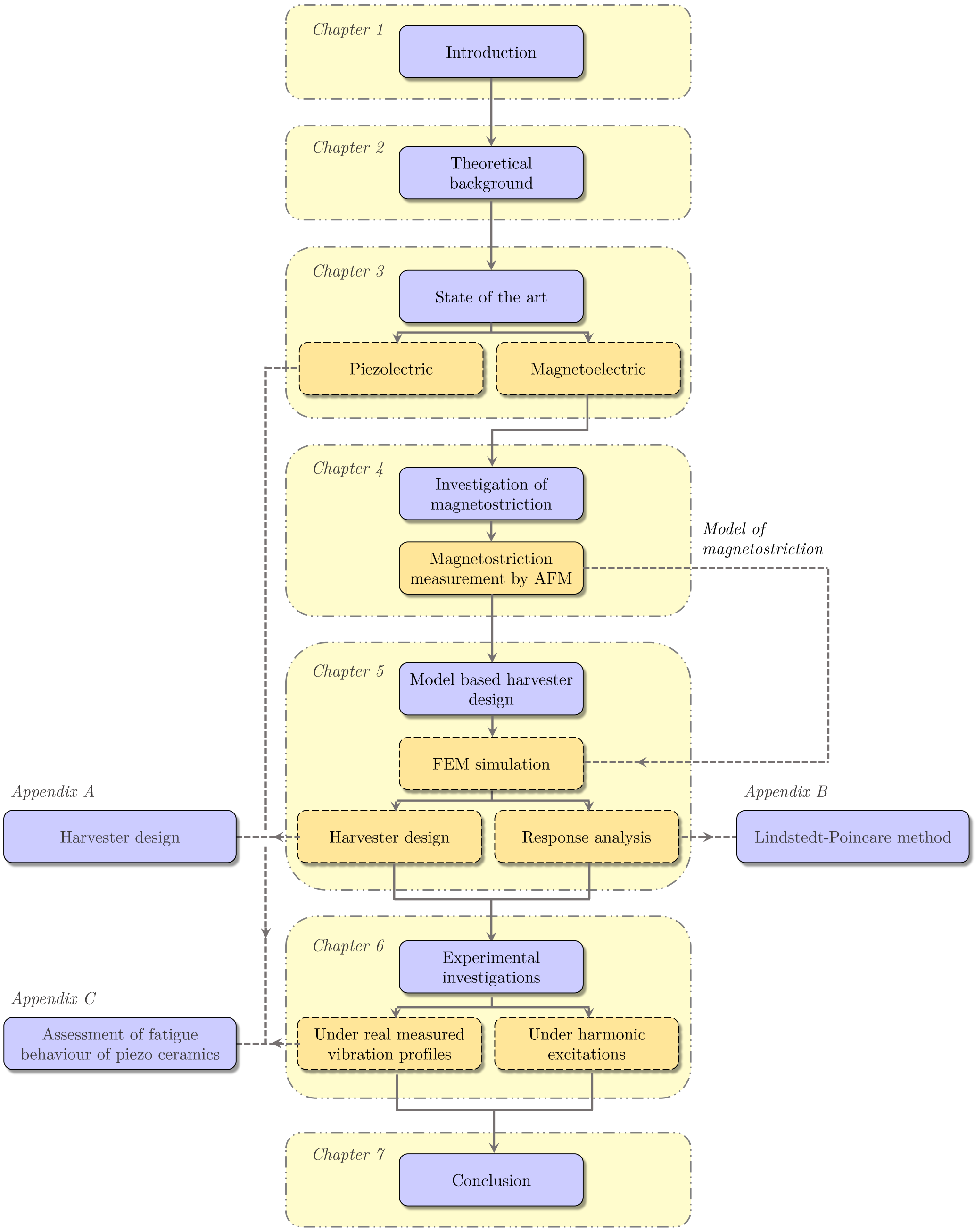

Figure 1.2: Structure of the thesis and interactions of the chapters

CHAPTER 2

Theoretical background

Magnetoelectric effect, which refers to the coupling between magnetic and electric fields in matter [16], has drawn increasing interest in vibration energy harvesting. Magnetoelectric transducers combine piezoelectric and magnetostrictive materials to form one composite able to convert magnetic field into electrical energy which may improve the efficiency of the vibration energy harvesting system [17].
This chapter presents an overview of the basic physical principles behind magnetoelectric energy harvesting with emphasis on magnetostrictive and piezoelectric laminate composites.

2.1 Magnetoelectric effect

The magnetoelectric effect can be presented as a polarization $\vec{P_o}$ response to an applied magnetic field $\vec{H}$ or conversely a magnetization $\vec{M}$ response to an applied electric field $\vec{E}$ [18]. This effect was predicted in 1894 and observed for the first time in 1960 [19]. A linear magnetoelectric behaviour can be observed when a weak AC magnetic field oscillating in the presence of a strong DC bias field [19]. Furthermore, the intensity of the ME effect is mainly depending on the ME coefficient C_{ME} coupling the magnetic and electric fields. The coupling mechanism can be written as given by Equation 2.1.

$$C_{ME} = \frac{electrical\ energy}{magnetic\ energy} \tag{2.1}$$

2.1.1 Magnetoelectric voltage coefficient

The ME effect is characterised by the magnetoelectric voltage coefficient, α_{ME} which relates the induced polarisation P_o to the applied magnetic field H according to the Equation 2.2 [20].

$$P_o = \frac{\alpha_{ME}}{\epsilon_0 \epsilon_r} H \tag{2.2}$$

where ϵ_0 and ϵ_r are respectively the vacuum permittivity and the relative permittivity. Furthermore, the magnetoelectric voltage coefficient can be defined as the change of the electric field with the change of the applied magnetic field as shown in Equation 2.3.

$$\alpha_{ME} = \frac{dE}{dH} \tag{2.3}$$

2.1.2 Magnetoelectric materials

In general, materials, which exhibit the ME effect are classified into two categories: single phase materials and composites.

2.1.2.1 Single phase ME materials

Magnetoelectricity has been observed as an intrinsic effect in some multiferroics materials which possess simultaneously ferroelectric and ferromagnetic properties [21]. These single phase ME materials have been under intensive study in the past decades [22]. In this context, materials such as Cr_2O_3 [23] [24], ME boracites [25] and phosphates [26] have been studied. However, the ME coupling in most of these materials is relatively too low to be used in practical applications [19]. Furthermore, most of single phase ME materials exhibit ME behaviour only at low temperature and they are not useful at room temperature [27].

2.1.2.2 Two phase ME materials

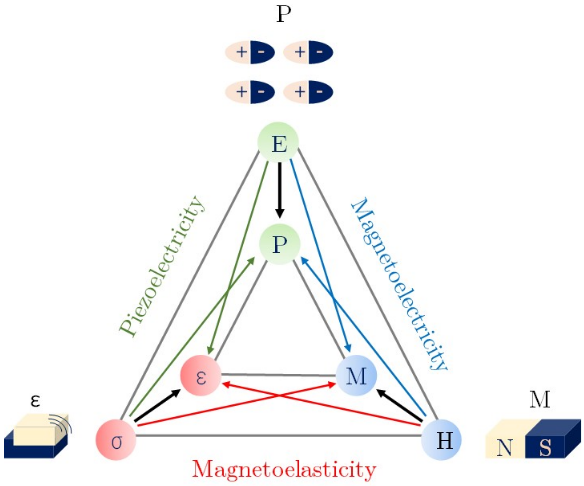

Figure 2.1: Basic coupling mechanisms of the magnetoelectric effect (adapted from [28]).

To overcome the limitations of single phase magnetoelectric materials, the ME behaviour has also been developed as a composite effect in multiphase systems by combining piezoelectric and magnetostrictive components [29] [30]. Various PE and Ms materials commonly used in ME composites are listed in Table 2.1.

The composite as a whole can be considered macroscopically as a new, homogeneous material with a significant improved ME coupling.

In such composite structures, during operation, a change of magnetic field affects the magnetostrictive elements leading to deformations, which are transmitted directly to the piezoelectric elements. The different interacting couplings in the ME effect are presented in Figure 2.1.

In composite ME materials, the ME voltage coefficient can be expressed as given by Equation 2.4.

$$\alpha_{ME} = \frac{dE}{dx} \times \frac{dx}{dH} \tag{2.4}$$

where dE/dx is the change in electric field per unit of dimension and dx/dH is the change in dimension per unit of magnetic field. In the following sections, the magnetostrictive effect and the piezoelectric effect are described.

2.2 Magnetostriction

The magnetostrictive effect can be defined as the deformation of a material during the magnetization process and conversely change of magnetization in response to applied stress. The phenomenon of magnetostriction depends on the crystal symmetry and in atomic scale on spin-orbit interaction [19] [32]. Additionally, it depends on texture and material composition [33].

The energy transformation from magnetic to mechanical and vice-versa is characterised by a short response time in the range of milliseconds which makes these materials technologically applicable for energy harvesting devices [31]. Dimensional changes in magnetostrictive materials are generated from the alignment of the magnetic domains inside the material (Figure 2.2). In case of $H = 0$, domains in the material are randomly oriented. Once a magnetic field is applied, the series of domains rotate to partially align themselves in the same direction as the magnetic field is applied resulting in dimensional changes. Increasing the applied field to a certain value (depends on the ME material), leads to reach saturation where a total alignment of all domains is observed.

The phenomenon of magnetostriction includes several effects which are principally related to the coupling between the magnetic and the elastic regimes in a Ms material. Table 2.2 summarizes the different effects exhibited by magnetostrictive materials. In the following sections, these effects are discussed and explained.

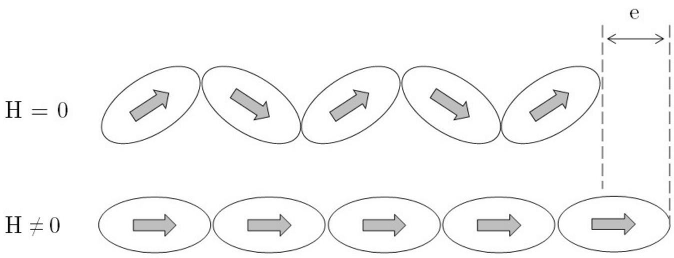

Figure 2.2: Rotation and re-orientation of the magnetic domains in magnetostrictive materials [31]

Table 2.1: List of well-known piezoelectric and magnetostrictive materials used as constituents of ME composites [34]

Piezoelectric materials	Magnetostrictive materials
Lead-based	Metals:
$Pb(Zr,Ti)O_3$ (PZT)	Fe, Co, Ni
$Pb(Mg_{1/3}Nb_{2/3})O_3$ -$PbTiO_3$ (PMNT)	Alloys:
$Pb(Zn_{1/3}Nb_{2/3})O_3$ -$PbTiO_3$ (PZN-PT)	FeNi-based
(PMN–PZT)*	FeCo-based
(PIN-PMN-PT)**	CoNi-based
Lead-free:	Ni_2MnGa
$BaTiO_3$ (BTO)-based	Permendur (FeCoV)
$(K_{1/2}Na_{1/2})NbO_3$ (KNN)-based	Galfenol (FeGa), FeGaB
$Na_{1/2}Bi_{1/2}TiO_3$ (NBT)-based	Samfenol ($SmFe_2$)
Others:	Terfenol-D ($Tb_{1-x}Dy_xFe_2$)
AlN	Fe-based metallic glasses (FeBSi,
ZnO	FeCoB, FeCoSi, FeCuNbSiB)
(Sr, Ba)Nb_2O_5	Ceramics:
$Ba_{1-x}Sr_xTiO_3$ (BSTO)	Fe_3O_4
$Bi_{1-x}Sr_xTiO_3$ (BST)	$Zn_{0.1}Fe_{2.9}O_4$ (ZFO)
$La_3Ga_{5.5}SiO_{14}$ (LGS)	$La_xSr_yMnO_3$ (LSMO)
$La_3Ga_{5.5}Ta_{0.5}O_{14}$ (LGT)	$La_xCa_yMnO_3$ (LCMO)
Polyurethane (PU)	Ferrites or doped Ferrites (e.g., $NiFe_2O_4$
Polyvinylidene difluoride (PVDF)	(NFO), (Li, Cu, Mn) ferrite)

* $Pb(Mg_{1/3}Nb_{2/3})_y\ (Zr_xTi_{1-x}\ )_{1-y}O_3$.
** $Pb(In_{1/2}Nb_{1/2})O_3$ -$Pb(Mg_{1/3}Nb_{2/3})O_3$ -$PbTiO_3$.

2.2.1 Joule effect and Villari effect

When a magnetostrictive material is subjected to a magnetic field, a mechanical strain occurs in addition to strains from applied stresses [35]. This effect is known as the Joule effect. It can be described by the mathematical function given by Equation 2.5.

$$\epsilon = \epsilon(\sigma, H) \tag{2.5}$$

where ϵ and σ represent respectively the strain and the stress. The Joule effect is usually associated with the actuation capability. Nevertheless, the excitation of the Ms element is also employed in a variety of sensing applications [36]. The Joule effect has an important reciprocal effect known as the Villari effect; The magnetization of a magnetostrictive material changes by mechanical stress in addition to changes by magnetic field [35]. This characteristic property of magnetostrictive materiel can be defined as given by Equation 2.6.

$$B = B(\sigma, H) \tag{2.6}$$

where B represents the magnetic flux density.

Table 2.2: Magnetostrictive effects

Direct effect	Inverse effect	Description
Joule effect	Villari effect	Relation between strain and magnetic field
Barret effect	Nagaoka-Honda effect	Relation between volume change and magnetic state
Wiedemann effect	Mateucci effect	Relation between torsional displacement and magnetic field
ΔE effect		Change of the Young's modulus as a result of a magnetic field
Hysteresis		History dependence

2.2.2 ΔE$_m$ effect

The ΔE$_m$ effect refers to the change of the young's modulus of the material due to the rotation of magnetic domains as a result of applied magnetic field. This effect can be quantified as shown in Equation 2.7.

$$\Delta E_m = \frac{E_{ms} - E_{m0}}{E_{m0}} \tag{2.7}$$

where E_{ms} and E_{m0} are respectively the Young's modulus with and without magnetic field.

The ΔE$_m$ effect is small in most materials such as nickel (ΔE$_m = 0.06$). However, it can reach relatively a large value in some giant magnetostrictive materials such as Terfenol-D (ΔE$_m = 5$) [37].

The stiffness of magnetostrictive materials depends on the applied excitation and initial conditions (zeo strain, zero external load or a condition in between) [38]. Furthermore, at magnetic saturation, magnetostrictive materials have an intrinsic or uncoupled stiffness.

2.2.3 Hysteresis

All existing magnetostrictive materials have a hysteresis response [39]. The hysteresis of magnetostrictive materials is more complex than that of regular magnetic materials.

The hysteresis relation for magnetostrictive materials is coupled with the mechanical variables of stress and strain [38]. This makes magnetostrictive devices difficult to control. For instance, the hysteresis in Terfenol-D is in the range of 2 % [40].

2.2.4 Other effects

In addition to purely compressive or tensile strain originated from applied magnetic field, there is also a shear stain, which results in a torsional displacement. This is known as the Wiedemann effect [40]. The inverse of the Wiedemann effect is called Matteuci effect [41]. Furthermore, applying a magnetic field can result on a change of the volume of magnetostrictive materials [37]. This is known as the Barret effect. However, this effect can only occur in extreme operational conditions. The inverse of the Barret effect is the Nagaoka-Honda effect. It can be defined as the change in the magnetic state caused by a volume change [42].

2.2.5 Magnetostrictive materials

Magnetostrictive materials (MsM) can be classified into two main categories: MsM based on highly magnetostrictive rare earth elements and MsM based on α-Fe with substitutions of non-magnetic Ga and Al for Fe [43].
Most of these materials are able to produce high magnetostriction only at cryogenic temperatures [44]. However, some other materials are capable of exhibiting ME effect at room temperature such as Terfenol-D, which is a Ms alloy of the rare earth elements terbium and dysprosium [45]. Table 2.3 presents the material properties of two well-known magnetostrictive alloys; Terfenol-D and Galfenol compared to Iron.

2.3 Piezoelectric effect

The piezoelectric effect can be defined as the electro-mechanical interaction between the mechanical and the electrical state in crystals without a centre of symmetry [46]. This effect is a reversible process (Figure 2.3). The direct piezoelectric effect is the ability of certain crystals to convert mechanical energy into electrical energy. Conversely, the inverse PE effect is the generation of mechanical stress resulting from an applied electrical field. The PE effect is nowadays used in many applications such as sensors, actuators and motors (Figure 2.4).

Table 2.3: Material properties comparison between Terfenol-D, Galfenol and Iron

		Terfenol-D [47]	Galfenol [48]	Iron [49]
Standard composition		$Tb_{0.3}Dy_{0.7}Fe_{1.92}$	$Fe_{81.6}Ga_{18.4}$	Fe
Crystallographic structure		Hexagonal	bcc	bcc
Mechanical properties	Unit			
Density	kg/m^3	9200 - 9300	7800	7874
Young's modulus	GPa	18 - 55*	40 - 60*	200
Tensile strength	MPa	28 - 40	350	180-210
Magnetostrictive properties				
Strain (ppm)	ppm	800 - 1200	200 - 250	-24
Energy density	kJ/m^3	4.9 - 25	0.6 - 0.7	
Piezomagnetic constant, d_{33}	nm/A	6 - 10	20 - 30	
Magnetic properties				
Relative permeability		2 - 10	75 - 100**	150 - 5000
Saturation flux density	T	1	1.5 - 1.6	2.2
Magnetomechanical properties				
Coupling factor		0.7 - 0.8	0.6 - 0.7	

* at constant I.

** estimated values based on low carbon steel.

2.3.1 Direct piezoelectric effect

When a piezoelectric material is subjected to a mechanical stress electrical charges are generated on its surface in addition to charges resulting from applying an external electrical field [50]. This effect is known as the direct piezoelectric effect. It can be described by the mathematical function given in Equation 2.8.

$$D = D(\sigma, E) \tag{2.8}$$

where D and E represent respectively the electric field displacement and the electrical field. An example of the use of the direct effect is found principally in voltage generators and sensors such as acceleration and pressure sensors.

2.3.2 Inverse piezoelectric effect

The inverse piezoelectric effect is that, in PE materials, a mechanical strain occurs when an electric field is applied in addition to stain resulting from mechanical stress. It can be described by the mathematical function given in Equation 2.9.

$$\epsilon = \epsilon(\sigma, E) \tag{2.9}$$

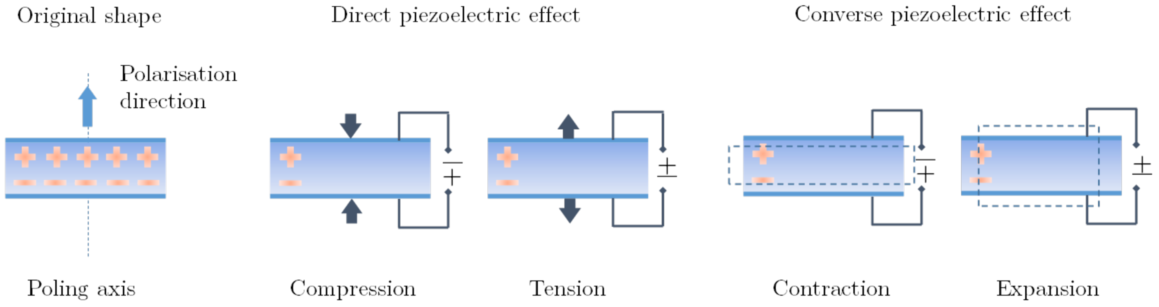

Figure 2.3: Direct and inverse piezoelectric effects

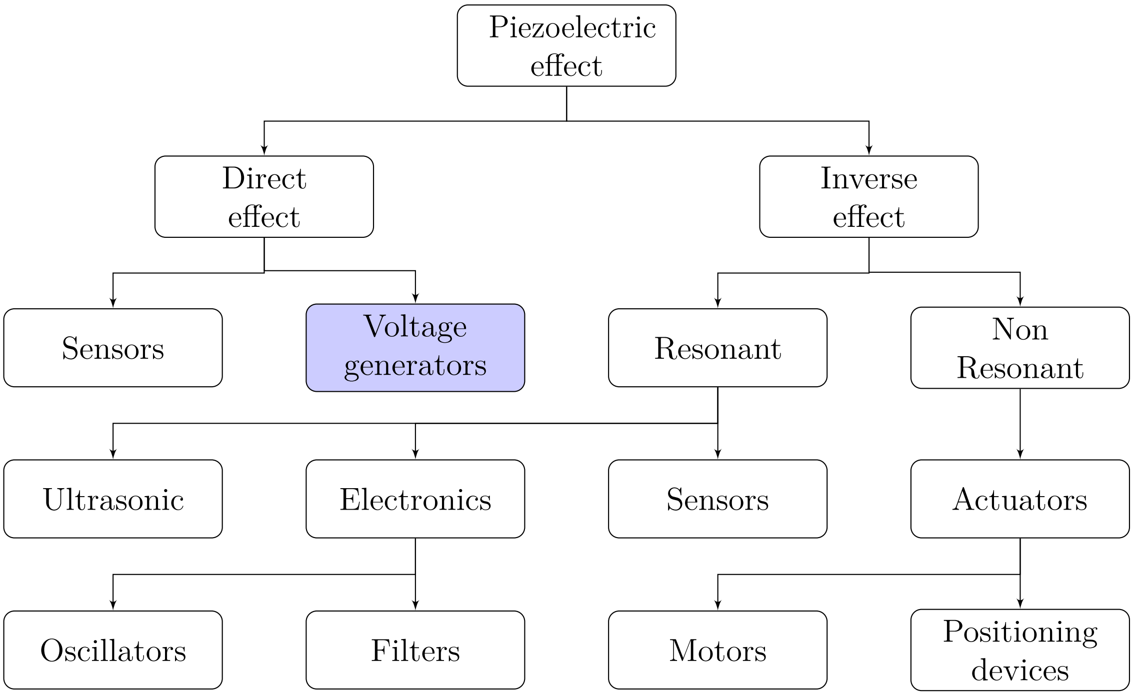

Figure 2.4: Applications of the piezoelectric effect [46]

An example of the use of the inverse effect is found in some types of sensors and principally in actuators and micro-positioning systems.

2.3.3 Poling process

Electric dipoles in piezoelectric materials are found by default to be randomly oriented. In this case, applying a mechanical force to the PE material results to a weak piezoelectric response.
In order to force these materials to be more piezoelectric sensitive, a process can be applied to PE materials to change the orientation of their electric dipoles in a prescribed direction. This process is known as poling process and can only be performed at temperatures below the curie point.

The poling process is implemented by applying a strong, direct current electric field along a specific direction for a sufficient time on the material [51]. Removal of the electric field leaves the dipoles in a configuration of near alignment. The poling process permanently changes the volume of the PE element [52]. The dimension between the poling electrodes increases and the dimensions parallel to the electrodes decrease. This process is shown in details in the Figure 2.5.

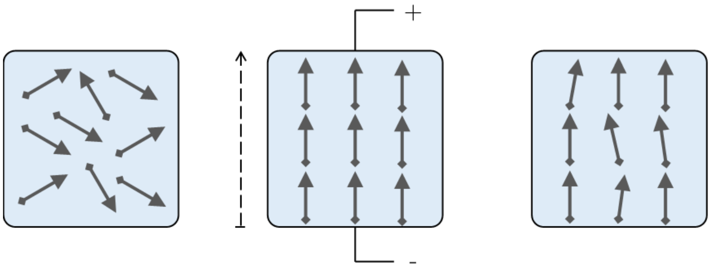

(a) (b) (c)

Figure 2.5: Alignment of electric dipoles in a material: (a) Unpoled, (b) During poling, and (c) After poling

2.3.4 Piezoelectric materials

Materials exhibiting the piezoelectric effect include a variety of naturally occurring crystals, natural materials, manufactured crystals, manufactured ceramics among others. The ideal material may be selected based on the application, since certain materials are more efficient than others. However, Lead Zirconate Titanate (PZT) and Lead Magnesium Niobate Titanate (PMNT) are more attractive than other piezoelectric materials due to their excellent piezoelectric properties. Table 2.4 describes the properties of some commonly used piezoelectric materials.

Table 2.4: Material properties comparison between PZT, Barium titanate and PMNT

		PZT [53]	Barium titanate [54]	PMNT [55]
Standard composition		*	$BaTiO_3$	**
Form		Polycrystal	Single crystal	Single crystal
Mechanical properties	Unit			
Density	kg/m^3	7600	5600	8100
Piezoelectric properties				
PE Charge Constant	10^{-12} m/V	$d_{33}=290$	$d_{33}=160$	$d_{33}=2000$
PE Voltage Constant	10^{-3} Vm/N	$g_{33}=26.5$	$g_{33}=11$	–

* $PbZr_{0.6}Ti_{0.40}O_3$ [56].
** $Pb(Mg_{1/3}Nb_{2/3})O_3$-$PbTiO_3$.

2.4 Magnetoelectric composites

Various interfacial bonding of the PE and Ms constituents for designing two-phase magnetoelectric composites have been proposed [34]. Commonly used composite structures can be classified as follows:

- 0-3 mode where magnetostrictive particles are embedded in the piezoelectric matrix [57] [58].
- 1-3 mode where magnetotrictive fibers/rods/tubes/wires are embedded in the piezoelectric matrix [59] [60].
- 2-2 mode where the composite is formed by alternating magnetostrictive and piezoelectric layers [61] [62].

Commonly reported ME composite structures are shown in Figure 2.6. There have been other coupling modes for synthesizing ME composites such us quasi-one dimensional ME composites which are formed by a magnetostrictive wire into a piezoelectric tube [63].

2.4.1 Modes of magnetoelectric composites

The selection of the suitable coupling mode is a critical factor due to the strong influence of the interfacial bonding on the ME response.
0-3 mode composites (see Figure 2.6 (a)) are simple to be fabricated. However, keeping the composite insulating is becoming problematic since the conductive Terfenol-D grain percolation path makes the polarization of the composite difficult and cause the charges developed in the piezoelectric phase to leak through this conductive path [64]. To avoid this, the low resistive magnetostrictive particles should be well dispersed in the piezoelectric matrix in such a way that the magnetostrictive particles have to be not in contact with each other while the piezoelectric matrix is self-connected. Hence, forming a 0-3 connectivity of phases, and the column fraction of the magnetostrictive grains in the piezoelectric matrix is limited by the percolation [65]. Besides 0-3 mode, the 1-3 mode is another type of ME structures where a fiber (or a rod, tubes, wires) is embedded in the piezoelectric matrix (see Figure 2.6 (b)). Such 1-3 ME composite can be fabricated via a dice-and-fill process [66]. Although the 0-3 mode and 1-3 mode with magnetostrictive structures embedded are simple, the 2-2 mode composites are more realizable (see Figure 2.6 (c)). This is mainly due the high concentration of conductive Terfenol-D which be easily separated by the piezoelectric layers in this composite structure. Furthermore, it was reported that 2-2 mode composites can exhibit higher ME voltage coefficients than others [34]. The fabrication of composites based on the 2-2 mode can be done with different dimensions, number of layers, and geometries including discs [67], rectangles [68] and rings [69]. However, a well know implementation of these structures is to bond rectangular PE and Ms plates using an epoxy resin. Most of reported composites based on the 2-2 mode are formed of 3 layers as shown in Figure 2.7. The influence of the composition of such structures

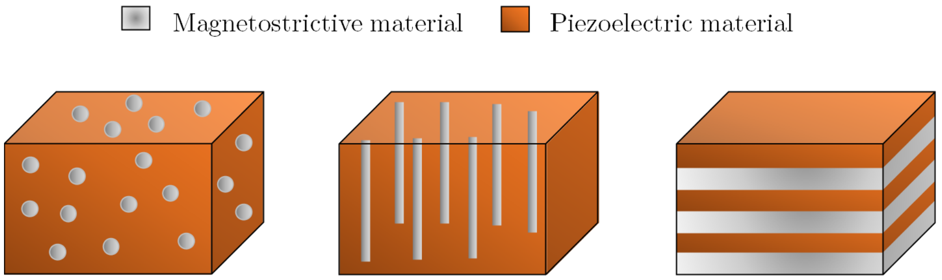

(a) (b) (c)

Figure 2.6: Commonly reported ME composites structures: (a) 0-3 mode, (b) 1-3 mode, and (c) 2-2 mode

in terms of the material of the inner layer and the relative thickness ratio of the layers is proposed in [70, 71]. In this study, the first ME composite is formed of a sandwich of PZT/Terfenol-D/PZT discs while the second ME composite is a sandwich of a sandwich of Tefenol-D/PZT/Terfenol-D discs. The ME voltage coefficient was measured for the two composites when varying the relative thickness ratio, f_v, of the Terfenol-D layer. Figure 2.8 shows numerical results for the two 2-2 sandwich composites with perfectly interfacial bonding between PZT and Terfenol-D disks. It is found that, for the Terfenol-D/PZT/Terfenol-D composite, the ME effect is nearly linearly proportional to the thickness ratio while for PZT/Terfenol-D/PZT composite, the ME effect increases by increasing the thickness ratio until reaching a maximum at $f_v = 0.85$ and then it decreases to nearly 0 at $f_v = 1$. It has to be indicated that in this study the used Terfenol-D layers was thicker than the PZT layers.

Figure 2.9 shows the ME voltage coefficients in different composite structures formed by different combinations of PE and Ms materials. It can be seen that laminate ME composites show higher magnetoelectric properties than other structures. In particular, giant ME effect is reported in a number of laminate composite of Terfenol-D or Metglas and various piezoelectric materials, which exhibit excellent piezoelectric properties, such us, PMNT or PZT. The maximum reported voltage coefficient was for the case of a Terfenol-D/PMNT laminate composite and it is up to 10 V/cm.Oe (1 kA/m = 12.54 Oe).

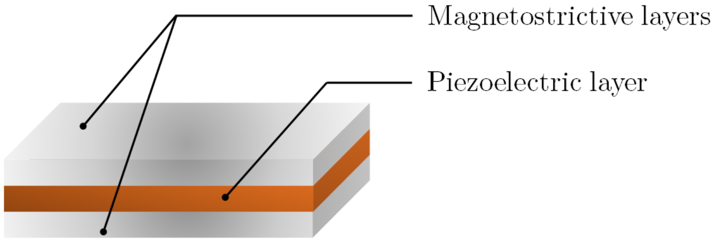

Figure 2.7: Schematic of a magnetoelectric laminate composite

2.4.2 Magnetoelectric laminate composites

Magnetoelectric laminates can be operated in numerous working modes. This depends mainly on the direction of polarization (P_o) and magnetization (M) of the piezoelectric and the magnetostrictive layers, respectively. For instance, when both M and P_o are oriented parallel to the length of the layers, the ME effect is designated as a longitudinal magnetization - longitudinal polarisation or (L-L) one. Similarly, when M and P_o are oriented parallel to the thickness of the layers, the ME effect is designated as a transverse magnetization – transverse polarisation or (T–T) one. Other vibrational modes such us L-T or T-L modes are also possible. The laminate composites are generally fabricated by bonding one PE layer to two Ms layers using an epoxy resin, followed in most cases by annealing at a temperature from 60 °C to 100 °C for good mechanical and electrical properties.

2.4.2.1 Bonding interface

In most of numerical and theoretical investigations of the ME effect in laminate composites, a perfectly bonding interface between the layers is assumed. In other words, they assume that the transmitted deformation to the inner piezoelectric layer is similar to the induced deformation in the magnetostrictive layer without losses. Any imperfect bonding interface influences the deformation transfer capability, which affects the ME response of the composite. Existing researches related to this field indicate that the thickness of the interfacial binder film between the layers is an important factor. Thinner interfacial binder film thickness guarantees better ME response of the laminate composite [64]. Furthermore, it is reported that with decreasing the shear modulus of the binder film, the interfacial bonding becomes weak due to the formation of a sliding interface leading to a large decrease in the ME response of the composite [64].

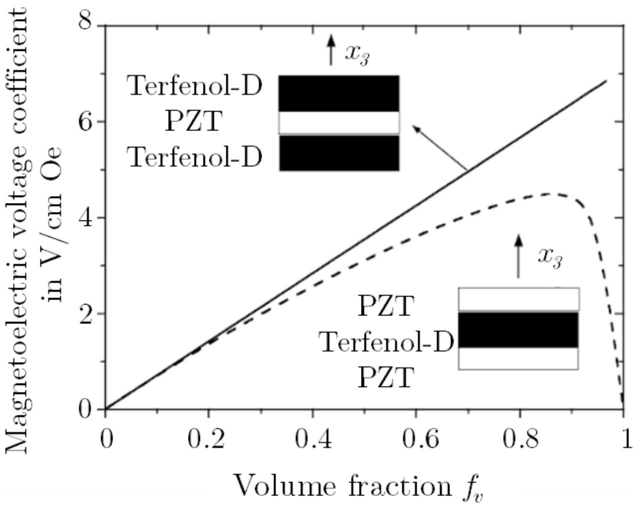

Figure 2.8: ME voltage coefficient as function of the volume fraction [65]

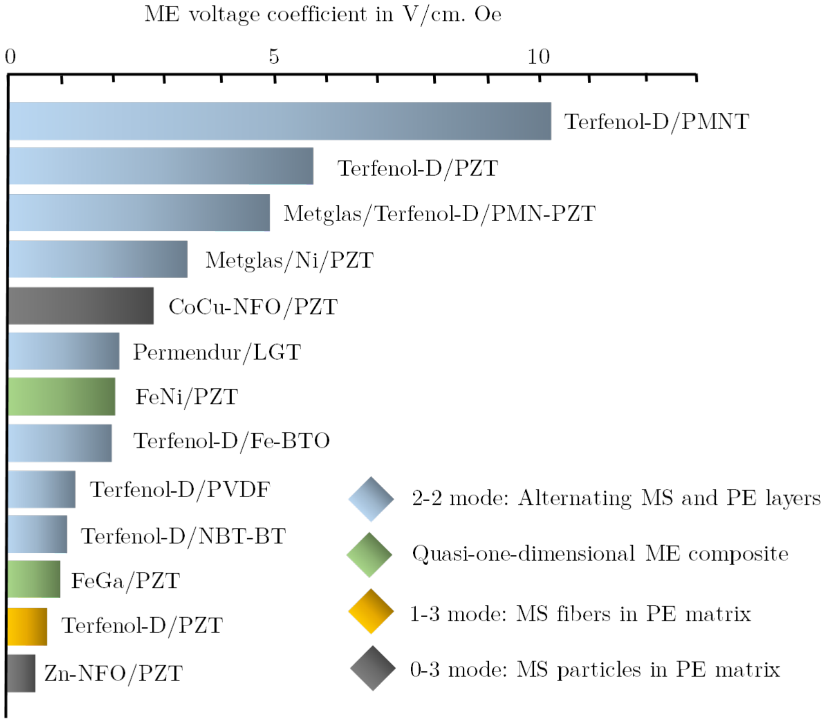

Figure 2.9: ME voltage coefficients in different composite structures and compositions (adapted from [34])

2.4.2.2 Magnetoelectric equivalent circuit

A well known approach to model 2-2 mode composites is the equivalent circuit approach [72, 73]. It is useful for modelling the ME behaviour of laminates in particular in the dynamic cases. This approach is based on piezoelectric and magnetostrictive constitutive equations, where the magnetostrictive and piezoelectric layers are mutually coupled through elastic interaction, via an equation of motion (strain-stress coupling between layers) [74].

Depending on the magnetiztaion and the polarization directions of the Ms and PE layers, respectively, the ME equivalent circuits for the corresponding mode can be derived under free boundary conditions where an applied magnetic field H acts as a magnetic induced "mechanical voltage" and then induces a "mechanical current" via a coupling factor φ_m. In turn, $\varphi_m H$ results in an electrical voltage V [65]. Using this approach, different parameters including mainly the ME voltage coefficient can be derived at low frequencies as function of the piezomagnetic constant, the voltage constants and the thickness ratio of the Ms layer among other parameters. At resonance, the limitation of the vibration amplitude have to be included by considering a finite mechanical quality factor.

In the next chapter, a detailed literature review is expounded and analysed about piezoelectric and magnetoelectric vibration energy harvesting devices.

CHAPTER 3

State of the art of piezoelectric and magnetoelectric vibration converters

To date, piezoelectric materials has been studied extensively to convert mechanical energy into electrical energy. So far, varieties of piezoelectric vibration converters have been proposed based on different coupling architectures. Two main groups of piezoelectric material based vibration energy harvesting can be identified; classical piezoelectric transducers and magnetoelectric transducers which are principally based on a combination of magnetostrictive and piezoelectric laminate composites.
This chapter is intended as a survey of recent progress in vibration energy converters based on piezoelectric and magnetoelectric effects.

3.1 Piezoelectric converters

The cantilever has been the most proposed geometrical design for piezoelectric vibration converters. This section reviews macroscale cantilever based vibration energy harvesting devices through piezoelectric transducers. The most common configuration of a piezoeoelectric harvester is a rectangular beam, a piezoelectric element and a tip mass as shown in Figure 3.1. In this configuration, the piezoelectric layer can be in the form of unimorph with one layer on top of the beam or in the form of bimorph with multiple piezoelectric layers on the beam.

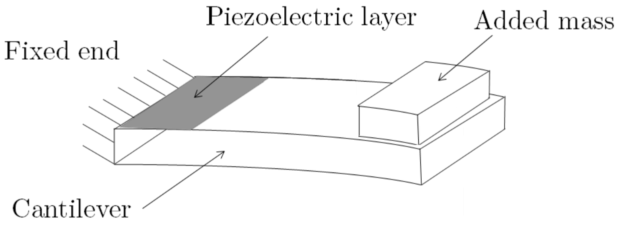

Figure 3.1: Schematic of a classical rectangular beam based piezoelectric vibration energy converter

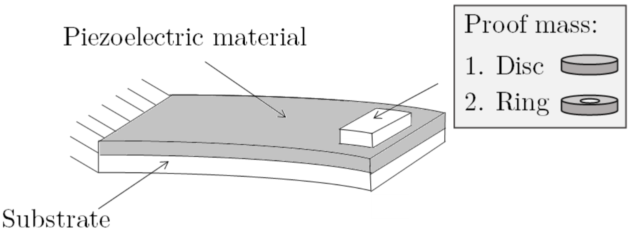

Figure 3.2: Schematic of the unimorph piezoelectric energy harvester with different proof mass shapes

3.1.1 Unimorph cantilever based piezoelectric converters

In [75], experimental analysis was carried out to determine the performance of an unimorph piezoelectric energy harvester without and with different proof mass shapes. To that end, two geometries of proof masses were employed; ring (3.6 g) and disc (0.55 g) proof masses. The developed converter consists of a piezoelectric (PZT 5H) layer on the top of the stainless steel substrate as shown in Figure 3.2. The converter was tested under real vibration profiles. In fact, one end of the cantilever was clamped to the different vibrating surface including mixer, DC motor, generator, alternator, and induction motor. For instance, it was reported that maximum output voltages of 0.456 V and 0.526 V were measured under a mixer vibration (3.2 m/s^2 and 3.4 m/s^2 applied accelerations respectively) when a disc and a ring mass were used as proof masses respectively. Additionally, the influence of the substrate thickness was studied. These results correspond to 0.8 mm and 0.1 mm substrate thicknesses respectively. In all experimental investigations, the reported output power was in the range of several hundreds of nW. It was demonstrated that the output performance of the harvester can be improved by choosing an appropriate proof mass geometry in addition to the selection of a suitable substrate thickness. However, the harvested power, for different applied real vibration, is relatively low and is not sufficient to continuously power a wireless sensor node.

A modification of the previous coupling architecture has been made by Gao et al. in [76]. In this study, a piezoelectric unimorph cantilever (PUC) with unequal piezoelectric and nonpiezoelectric lengths was investigated theoretically and experimentally. Figure 3.3 shows a schematic of the proposed piezoelectric unimorph cantilevers. It is found that PUCs with unequal piezoelectric and nonpiezoelectric lengths with a concentrated force applied at the tip and found that the PUC with a longer non-piezoelectric layer gave a larger induced voltage at a fixed vibration frequency. For instance, the maximum measured powers per applied acceleration were 2 μW/(m/s^2) and 4 μW/(m/s^2) for 1 and 1.8 length ratios respectively. It has to be noted that the optimal length ratio of the piezoelectric and non-piezoelectric layers is not investigated in this study. Furthermore, the effect of increasing the length of the non-piezoelectric layer on the resonance frequency of the harvester, which has a great influence on the performance of the vibration converter, is not evaluated.

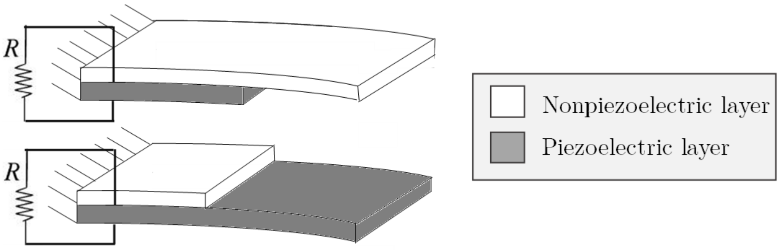

Figure 3.3: Schematic of the unimorph cantilevers with unequal piezoelectric and nonpiezoelectric layers lengths

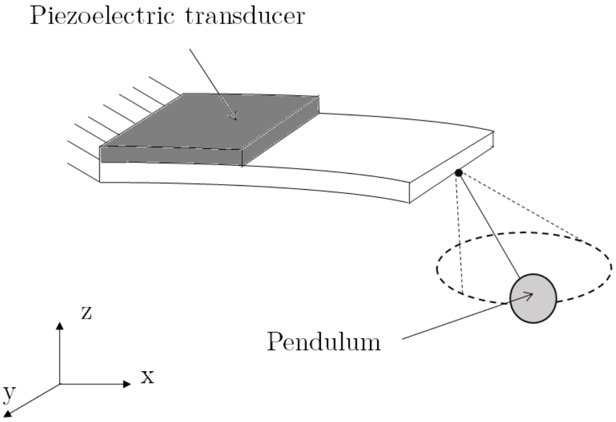

Figure 3.4: Schematic of the unimorph cantilever-pendulum piezoelectric harvester proposed by Xu *et al.*

In [77], Xu et al. reported a PUC design with a pendulum for multi-directional energy harvesting. As shown in Figure 3.4, the design consists of a pendulum attached to the free end of the piezoelectric cantilever. The aim was to benefit from the non-linear coupling between the pendulum motion in 3-dimensional space and the beam bending vibration at resonances. Very low excitation amplitudes were applied to the PUC (0.008 g). In the proposed design, the resonance frequency of the beam and the pendulum are 9.13 Hz and 4.56 Hz, respectively.

The experimental results indicate that the proposed harvester can generate power output under excitations in x, y and z axis, which presents an improvement to the traditional cantilever design which performs optimally under vibration parallel to z direction. The reported maximum voltage output was 3.01 V under x- or y-direction excitations compared to 3.29 V obtained under z-direction excitation. Nevertheless, the power outcome of the harvester is not evaluated.

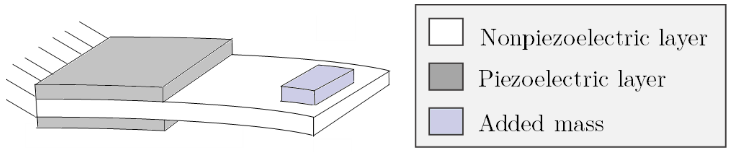

Figure 3.5: Schematic of the bimorph piezoelectric beam generator by Roundy *et al*.

3.1.2 Bimorph cantilever based piezoelectric converters

The second typical piezoelectric energy harvester is a bimorph cantilever located on a vibrating host structure, to generate electrical energy from base excitations.

In 2005, Roundy et al. developed a bimorph piezoelectric beam generator [79]. In this design, a tow layer bender is mounted as a cantilever beam with an added mass at the end and the top and bottom layers are composed of piezoelectric material as shown in Figure 3.5. The results prove that designs with 5 g and 10 g added masses are able to generate 200 μW and 400 μW output power, respectively, at about 120 Hz and an acceleration of 0.25 g.

A similar design in proposed by Aboulfotoh et al. [78]. It consists of two symmetrical piezoelectric layers in parallel connection and a middle non-piezoelectric layer and holds a tip mass (Figure 3.6). In this work, the influence different parameters on the power output are studied, including the ratio between the thickness of the middle layer and that of the piezoelectric layer, the free length and the mass ratio. It is reported that the output powers of 10 μW to 20 μW were achieved at 250 Hz and 260 Hz into 9.7 kΩ and 73 kΩ, respectively. Based on this study, the most significant parameter affecting the power output of a bimorph piezoelectric cantilever is the thickness, which has to be maximized as much as possible.

Another configuration of piezoelectric cantilever generator is reported in [80]. The main difference to the previous architecture is the elimination of the proof mass. The aim of this study was to develop a model of PZT power harvesting devices. The model was evaluated using a commercially available piezoelectric bimorph actuator (Quick Pack QP40N plate manufactured by Mide Technology) as shown in Figure 3.7.

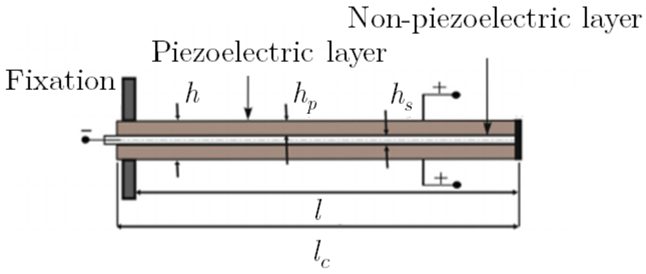

Figure 3.6: A sketch of a bimorph piezoelectric cantilever proposed by Aboulfotoh *et al*. [78]

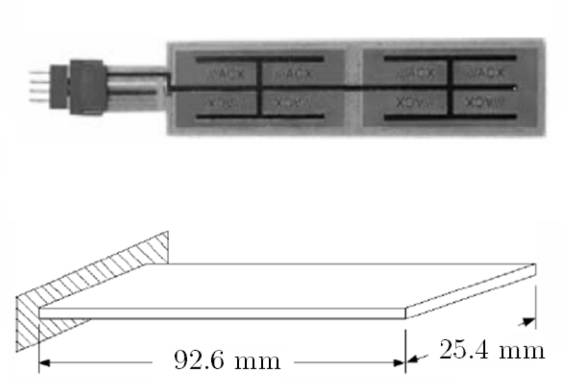

Figure 3.7: Quick Pack QP40N plate manufactured by Mide Technology [80]

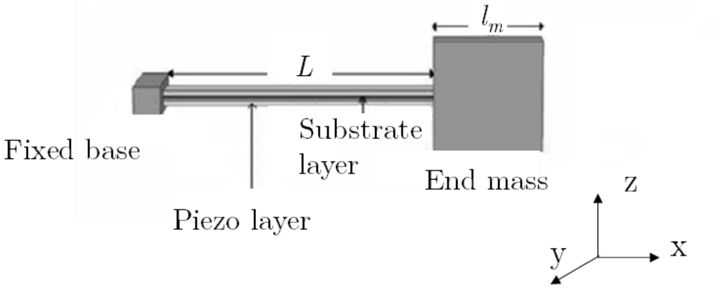

Figure 3.8: Schematic and cross section view of the bimorph generator proposed by Kundu *et al.* [81]

It was reported that a maximum of 500 μW into a 15 kΩ resistance at 113 Hz and 1 g acceleration can be generated. Besides, another PZT bender with a bimorph structure was proposed in [81]. The energy harvester consists of three layers of uniform thickness with an end mass attached symmetrically to the free end as shown in Figure 3.8. The central layer is brass substrate sandwiched between two piezoelectric layers of PZT-5H. The top and bottom surfaces of the bimorph are metallized to form the electrodes that can be wired as parallel or series connections. The optimal load resistance for parallel configuration is found to be 10.3 kΩ, and at the resonance frequency 100 Hz, the generated power is 0.323 mW.

As it can be seen from the previous mentioned researches, a common characteristic is the high resonance frequency of the developed prototypes, which is more than 100 Hz. This can be a limitation for the wide use of these converters in real applications.

A design employing multiple piezoelectric layers is proposed in [82] by Zhu et al.. Three generators were fabricated using single-, double- and triple- PZT layer as shown in Figure 3.9.

The generators have the same dimensions and same total piezoelectric layer thickness of 150 μm. The output performances of the three configurations were investigated in

order to evaluate the use of multi-layer generators compared to a single-layer one. The three prototypes were fabricated by screen printing and tested experimentally. It was found that a double-layer generator produces 41.5 % and 19.4 % more power than a single layer and a triple layer generator, respectively, with the same total thickness of PZT and the same resonant frequency.
For instance, the maximum measured output powers in the single-, double- and triple-PZT layer designs were 69.18 μW, 97.9 μW and 82.61 μW at 158 kΩ, 37 kΩ and 17 kΩ load resistances respectively. These results demonstrate that the use of multiple transducers in the design of the converter does not guarantee higher output powers. Table 3.1 summarizes all presented piezoelectric converters. It can be concluded that a deep investigation of the geometrical parameters, the used piezoelectric material and the structure of the converter, among others, are required for the design of a high-performance piezoelectric vibration converter.

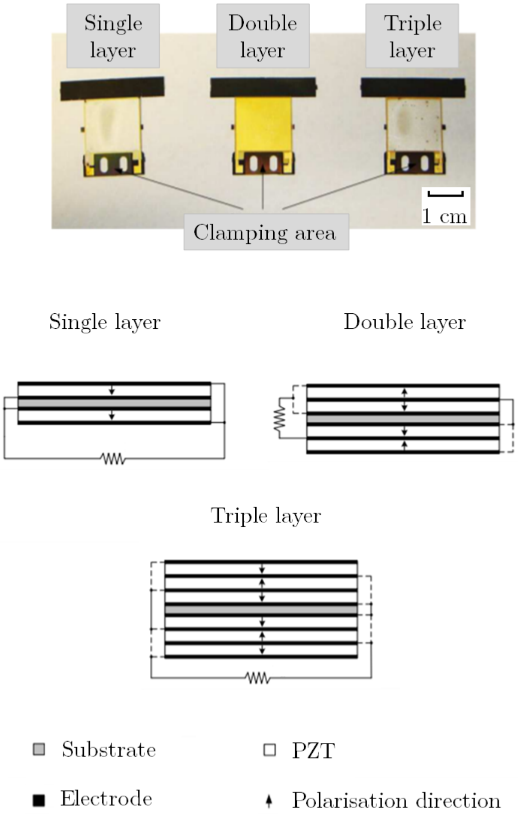

Figure 3.9: Picture and schematic of the bimorph multilayer piezoelectric vibration energy harvester proposed by Zhu *et al*. [82]

Table 3.1: Summary of reviewed piezoelectric harvesters

Architecture	Ref.	Frequency (Hz)	Power (mW)	Acceleration (g)	Note
Unimorph	[75]	< 20	0.001	0.01 to 0.56	Ring (3.6 g) and disc (0.55g) proof masses
	[76]	–	0.004	0.1	Different nonpiezoelectric-to-piezoelectric length ratio
	[77]	9.13	– (3 V)	0.008	With a pendulum
Bimorph	[79]	120	0.2	0.25	5 g added mass
	[79]	120	0.4	0.25	10 g added mass
	[78]	260	0.02	–	–
	[80]	113	0.5	1	A commercial piezo element is used
	[81]	100	0.323	–	Uniform thickness for all layers
	[82]	64.5	0.069	–	Single PZT layer
	[82]	64.5	0.097	–	Double PZT layers
	[82]	64.2	0.082	–	Triple PZT layers

3.2 Magnetoelectric converters

Different magnetoelectric converters have been developed by numerous researchers. Most developed magnetoelectric converters are mainly using laminate composites of Terfenol-D and piezoelectric layers. In the following, a selection of ME harvesters are detailed and classified with respect to their architecture: vibration-based cantilever, vibration-based spherical magnet, vibration-based magnetic levitation, vibration-based wire current, vibration-based rotary pendulum (Figure 3.10).

3.2.1 Cantilever based magnetoelectric converters

A popular coupling architecture of magnetoelectric converters employs a three-layer magnetostrictive laminate composite formed of thin piezoelectric layer bonded to two magnetostrictive layers and placed in the air gap of a magnetic circuit fixed at the end of a cantilever beam. An implementation of such architecture with a magnetic circuit composed of Neodymium (NdFeB) magnets and magnetic yokes was reported in 2009 by Dai *et al*. as shown in Figure 3.11 (a). The ME transducer is a sandwich of one lead zirconate titanate (PZT) plate ($12\times10\times1$ mm^3) bonded between two Terfenol-D plates ($12\times10\times1$mm^3). The prototype delivers a maximum power output of 1.055 mW across

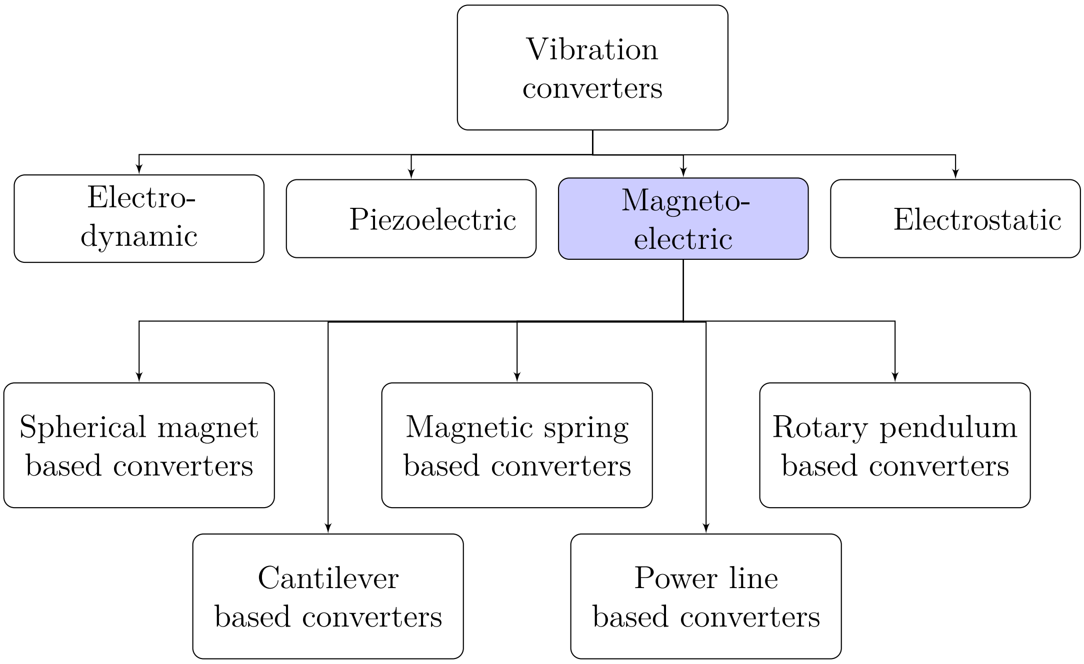

Figure 3.10: Possible architectures for magnetoelectric vibration energy converters in literature

564.7 kΩ load at 51 Hz frequency for an acceleration of 1 g. The output power density of the harvester is 0.472 mW/cm^3 when only considering the volume of the cantilever beam, the magnetic circuit, and the transducer [83]. This value should not be taken into account since it is not presenting the whole system. Zhang *et al.* reported another macro scale harvester based on similar architecture in 2012 as shown in Figure 3.11 (b). A PMN-PT layer (12×6×1 mm^3) is bonded between two Terfenol-D layers (12×6×1 mm^3) to form the ME transducer. The magnetic circuit is made up of two magnetic yokes and of eight NdFeB magnets with different magnetic polarization to produce a concentrated flux gradient acting on the transducer.

The harvester generates at resonant frequency of 30.6 Hz a maximum output power of 1.9015 mW across 3.585 MΩ resistor at 1 g acceleration and a power of 0.7804 mW at 0.3 g acceleration [84].

Another implementation of this architecture was published by Dai *et al.* in 2011. The proposed harvester employs multiple Terfenol-D/PMNT/Terfenol-D laminate magnetoelectric transducers (12×6×1 mm^3). Four prototypes were fabricated to investigate the optimal power output of the harvester using various numbers of transducers in different positions respecting the magnetic flux density distribution. The first prototype is formed with a single transducer placed at position 1 as shown in Figure 3.11 (c), the second and third prototypes are each formed with two transducers placed at positions 1, 4 and 2, 3 respectively. The fourth prototype is formed of four transducers placed at position 1, 2, 3 and 4. Results show that 1.44 mW at 1 g acceleration, 4.07 mW at 1.5 g, 3.95 mW at 2 g and 7.13 mW at 2.5 g can be generated at 26.2 Hz, 37 Hz, 29.4 Hz and 34.8 Hz for the four prototypes, respectively [85].

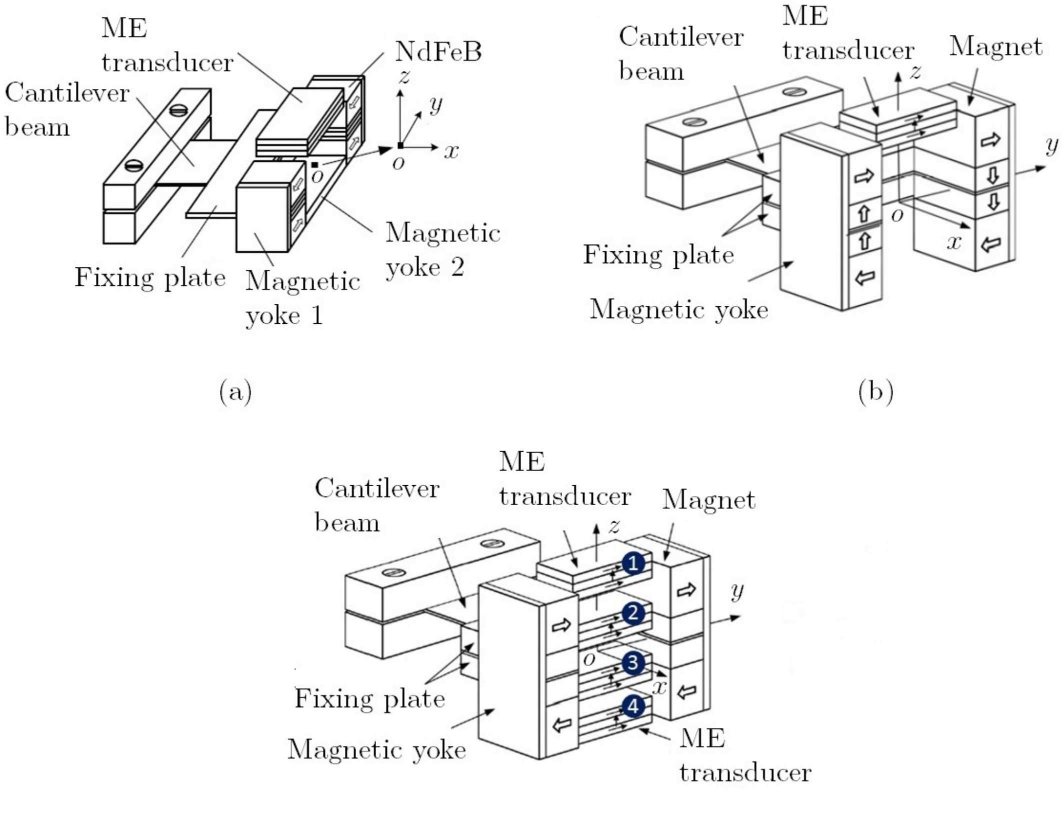

(a) (b)

(c)

Figure 3.11: Magnetoelectric energy harvesters with magnetic circuit attached to the end of a cantilever beam. (a) Single transducer reported by Dai *et al.*, (b) Single transducer reported by Zhang *et al.*, and (c) Multiple transducers reported by Dai *et al.* [83] [84] [85]

When considering only the volume of the magnetic circuit, the transducers, and the cantilever beam, the maximum output power densities of the prototypes 1, 2, 3 and 4 are 0.24, 0.63, 0.61 and 1.1 mW/cm^3 respectively.

A modification of the previous coupling architecture has been made by Bai *et al*. In this development, a spiral cantilever beam is used instead of conventional cantilever beam in order to improve the operation frequency range [86]. The design consists of a spiral-shaped cantilever with tip mass in the form of magnets coupling with a ME transducer as shown in Figure 3.12. Furthermore, peak frequencies can be tuned and the frequency spacing between the adjacent modes can be reduced due to the magnetic coupling between the transducer and the magnets. The experimental results indicate that the proposed harvester can obtain five obvious peak values in the range of 15 to 70 Hz, which are concentrated around 20.7, 26.1, 32.3, 42.2 and 63.7 Hz. For these peak frequencies, the maximum output powers are 118.3, 25.1, 80.5, 40.5 and 6.21 μW, for resistances of 1.35, 1.27, 1.22, 1.13 and 1.07 MΩ, respectively.

In 2011, Li *et al*. employed the magnetic coupling to tune the resonance frequency of the harvester [87]. In fact, the developed prototype is based on a ME transducer formed by Terfenol-D/PMNT/Terfenol-D plates ($12\times10\times3$ mm^3) placed in a cylindrical magnet, a cantilever beam and a circular magnet as shown in Figure 3.13 (a). The repulsive magnetic force between the magnets makes the resonant frequency of the harvester tunable. It is reported that the maximum power generated is 68.8 μW under an acceleration of 0.2 g at a resonant frequency of 25.4 Hz and the frequency tunable range can reach 4.4 Hz. Later on, they fabricated a generator based on this design [88]. The new prototype has two cylindrical magnets arranged on the free end of a cantilever beam, and two hollow magnets with ME transducers inside their cavities as presented in Figure 3.13 (b). The harvester has been mounted on a wheel driven by an AC servo-actuator. It is reported that a maximum power of 517 μW can be generated at a rotation frequency of 9.8 Hz, corresponding to a half-power bandwidth of 13.5 Hz.

Figure 3.14 shows a cantilever based magnetoelectric harvester design without the use of magnetostrictive layers, investigated by Qiu *et al*. in 2014 [89]. In this design, the transducer is a multi-layered structure composed of a PZT layer ($12\times6\times1$ mm^3), two NdFeB permanent magnet layers ($12\times6\times2$mm^3) and two triangular-tooth aluminium clamps ($12\times6\times1.5$ mm^3).

Instead of magnetostrictive material, the triangular-tooth aluminium clamps, placed between the piezoelectric layer and permanent magnets, transmit the mechanical stress to the piezoelectric layers, which respond by generating electrical energy. Experimental results show that the presented vibration energy harvester can obtain an average power of 0.39 mW for an acceleration of 0.6 g at a frequency of 38 Hz. Furthermore, Yang *et al*. proposed a broadband ME vibration energy harvester applicable in two-dimensional motion. The structure of the converter is presented in Figure 3.15 [90]. It consists of a circular cross-section elastic rod, a ME transducer and a magnetic circuit. Contrarily to conventional cantilever beam, the elastic rod is able to extract the 2 D vibration

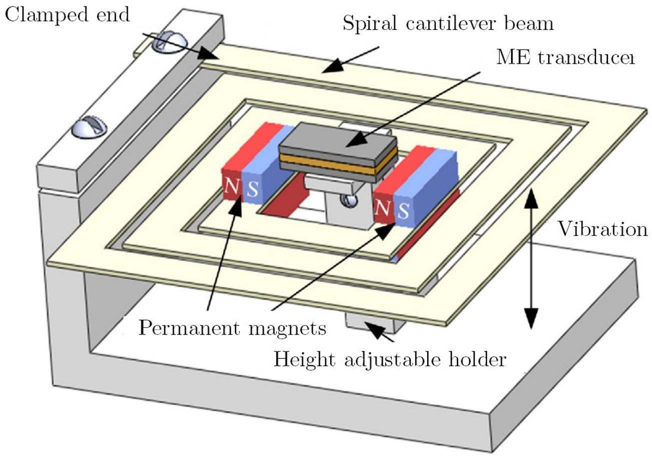

Figure 3.12: Spiral-shaped cantilever generator proposed by Bai *et al*. [86]

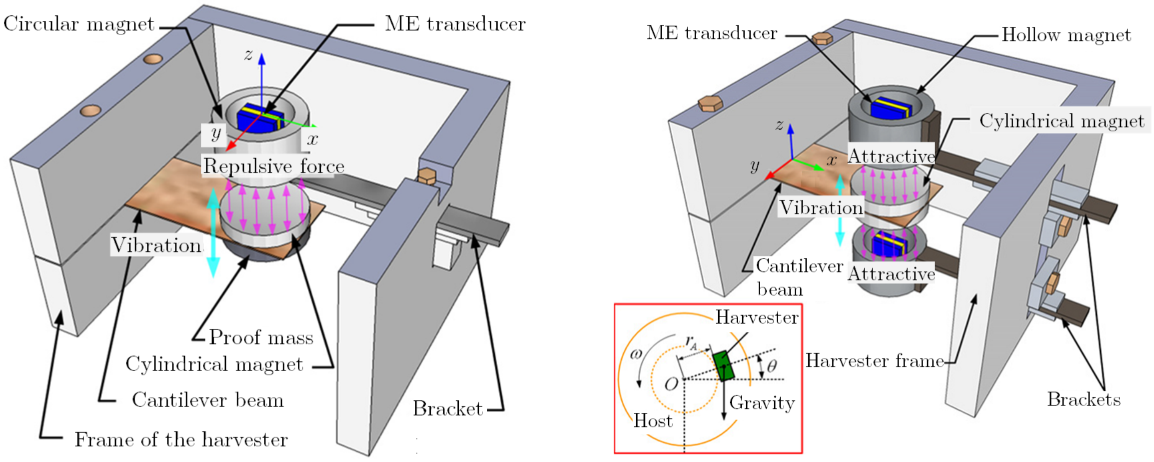

(a) (b)

Figure 3.13: Magnetoelectric energy harvesters with resonance frequency tunability proposed by Li *et al.*. (a) Single transducer generator, and (b) Twin transducer generator [87], [88]

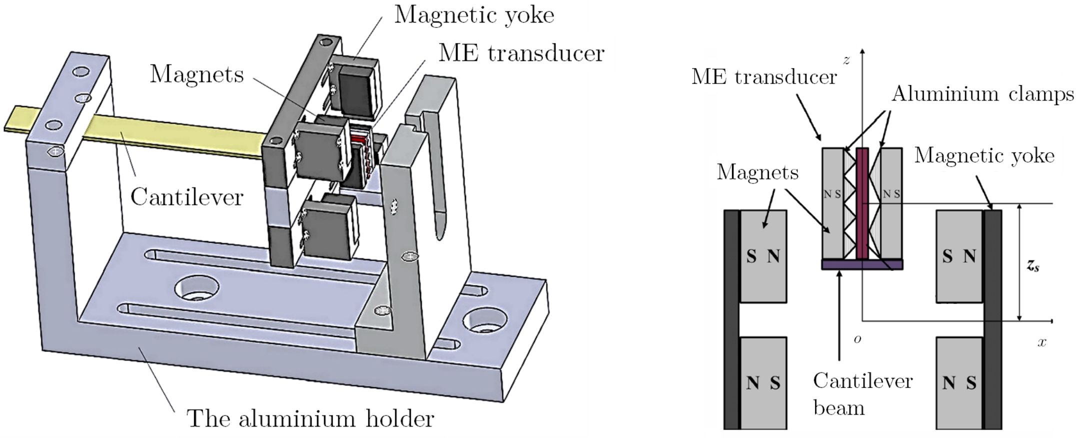

(a) (b)

Figure 3.14: Magnetoelectric energy harvester proposed by Qiu *et al.* (a) A schematic diagram of the converter, and (b) Magnet/piezoelectric composite transducer [89]

energy in y-z plane (Figure 12). In fact, one end of the elastic rod is free, in which a disc and a ring magnet are coaxially mounted, and the other end is fixed to the harvester housing. The ME transducer is placed in the air gap between these magnets and two other coaxially magnets are fixed to the housing. In the experiment, two ME transducers with different dimensions have been used; a ($12\times6\times2.8$ mm^3) transducer and a ($12\times3\times2.8$ mm^3) one. Results of the experiment performed on the narrower ME transducer show that, for an acceleration of 0.6 g, output powers of 0.6, 0,49, 0.33, 0.5 and 0.56 mW are obtained for excitation angles of -90°, -45°, 0°, 45°, and 90°, respectively, for a load of 2.9 MΩ. On the other hand, for the 6 mm width transducer

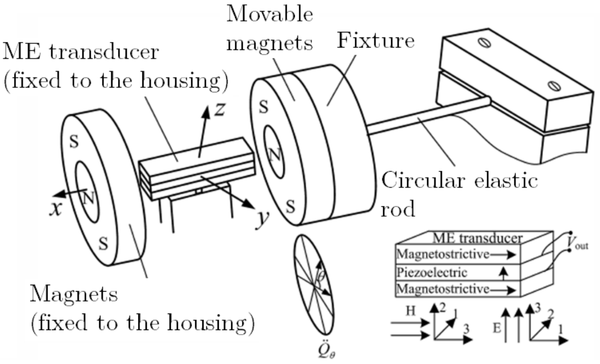

Figure 3.15: Two dimensional broadband vibration converter proposed by Yang *et al.* [90]

and for similar excitations, the output power doesn't exceed 0.2 mW for a load of 5.91 MΩ. However, the frequency bandwidth increased due to the larger non-linear factor in comparison to the 3 mm width transducer.

3.2.2 Spherical magnet based magnetoelectric converters

The use of a spherical permanent magnet as a proof mass can be considered as one of the commonly applied coupling architectures. Based on this architecture, Moss *et al.* developed a bi-axial magnetoelectric energy harvester in 2012 [91]. The aim was to develop a potential solution of powering structural health monitoring systems embedded within aircrafts. A bi-axial oscillator is created using a permanent-magnet/ball-bearing arrangement (Figure 3.16). The magnet produces a bi-axial restoring force on the bearing and it steers magnetic field through the transducer. For excitation with 61 mg root mean square (RMS) of acceleration and 9.8 Hz frequency, a peak RMS power of 121 μW is reached.
The same coupling architecture has been used by Ju *et al.* in 2013 [92]. The transducer is based on a freely movable spherical permanent magnet to transform external vibration into a time varying magnetic field applied to the magnetoelectric transducer made of Ni-Mn-Ga (magnetic shape memory alloy) and PZT as shown in Figure 3.17. The prototype is able to generate a maximum output voltage of 10.24 V and output power of 4.1 μW for 950 Ω load when it is mounted on a smart phone or shaken by hand.

3.2.3 Magnetic spring based magnetoelectric converters

Harvest energy from non-linear vibration created by magnetic spring has been also investigated. Zhu *et al.* developed in 2012 a magnetoelectric converter with the use of magnetic spring principle as presented in Figure 3.18 [93]. In this development a ring magnet oscillates between two repulsive magnets, which are fixed to the pipe's outer surface. The transducer is formed by three-layers Terfenol-D/PZT/Terfenol-D composite, and is fixed to the pipe inner surface at the centre.

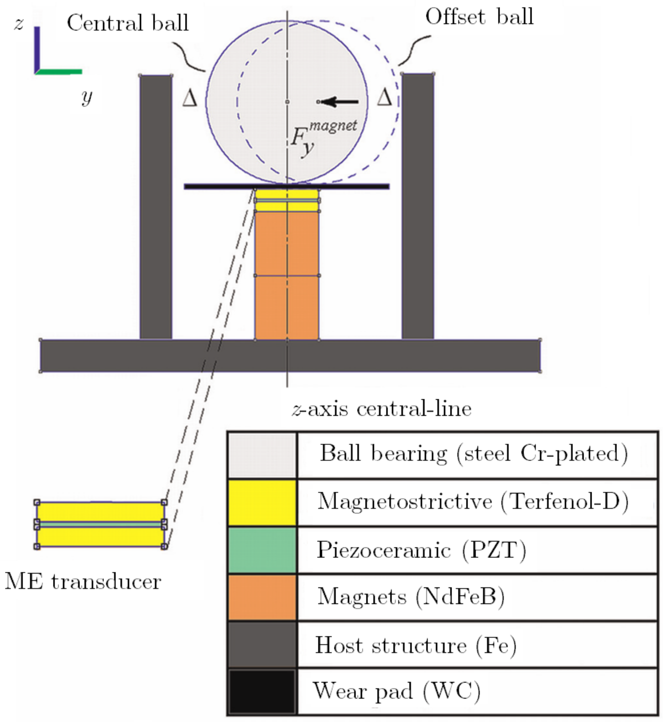

Figure 3.16: Magnetoelectric energy harvester with spherical permanent magnet proposed by Moss *et al.* [91]

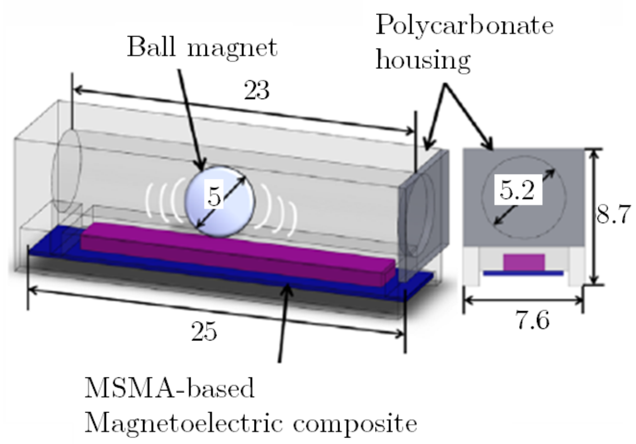

Figure 3.17: Low frequency magnetoelectric energy harvester proposed by Ju *et al.* [92]

It has been reported that for an excitation frequency of 10 Hz and at 1 g of acceleration, the maximum power output is 1.1 mW across 10 MΩ load resistance, which corresponds to a high power density of 3.46 $\times 10^3$ W/m^3 when only the volume of the transducer is considered.

In 2014, Naifar *et al*. developed a magnetoelectric converter based on magnetic levitation [94]. The coupling architecture is composed by two magnetic springs and two ME transducers placed on the air gap between two rectangular magnets. The poles of the thin magnets are placed in such a way that the upper ones are levitated as presented in Figure 3.19. The laminate is made of two PZT layers (12×6×0.25 mm^3) bonded between two Terfenol-D layers (12×6×1 mm^3). The predicted power generation is 30 μW at a resonance frequency of 29 Hz for an excitation amplitude of 1 mm.

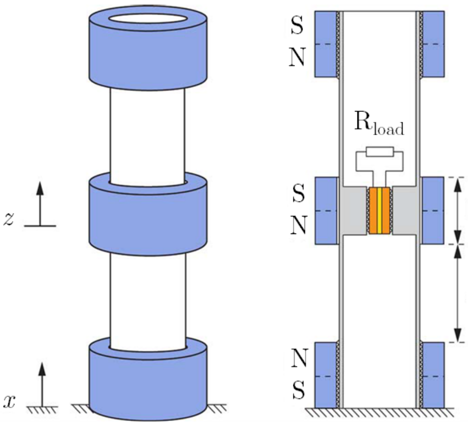

Figure 3.18: Two dimensional and three dimensional view of the harvester proposed by Zhu *et al*. [93]

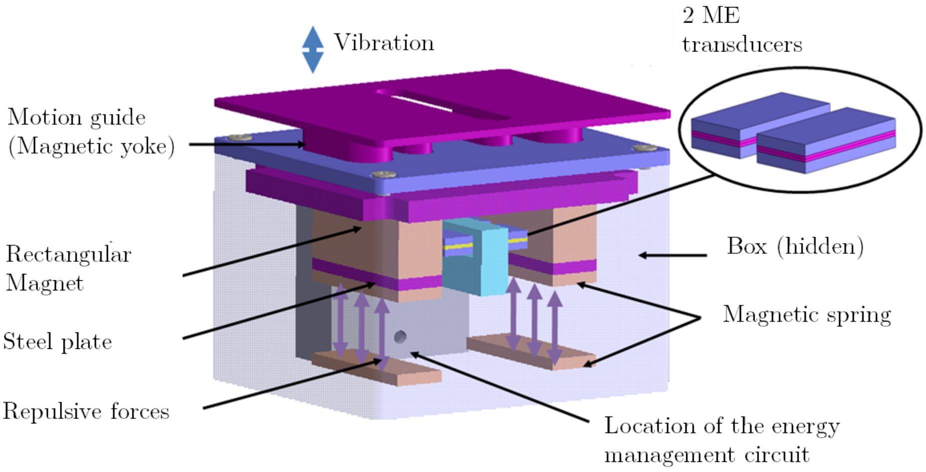

Figure 3.19: Magnetoelectric energy harvester with twin lateral transducers by Naifar *et al*. [94]

3.2.4 Power line based magnetoelectric converters

Another reported method for the design of ME energy harvesting is based on the AC magnetic field around electric power lines based on the Ampere's law. This method provides a promising solution to the power supply of wireless sensor nodes since power lines can be readily found in human daily life. It consists of the use of a magnetic circuit placed around the power line to produce a concentrated magnetic flux density on the wires and a force acting on the magnetic circuit. Several attempts have been made to develop piezoelectric cantilever beam generators for energy harvesting from power lines [95, 96]. However, it was reported that the sharp vibrations of a piezoelectric cantilever beam can cause fracture in the PE layers [97]. A novel converter based on magnetoelectric transducer has been explored by He *et al.* who investigated the harvesting of electrical power from AC magnetic field around electric power lines by mounting a Halbach array and a magnetic circuit on the free end of a cantilever beam as shown in Figure 3.20 [97]. The idea is to create first relative motion between the magnetic circuit and the transducer based on the magnetic field generated by the power line. The Halbach array, which is constructed from three specially arranged NdFeB magnets, produces augmented magnetic field on the side where the power line

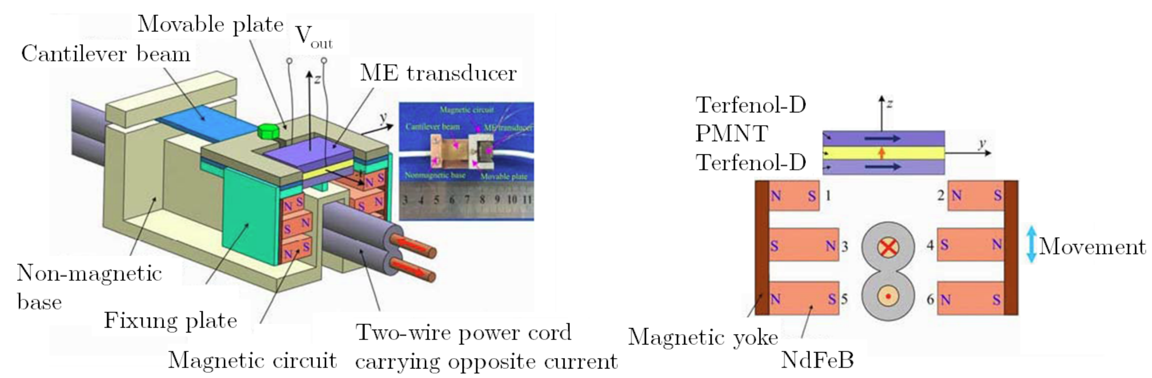

(a) (b)

Figure 3.20: Energy harvester from two-wire power cords proposed by He *et al.* [98]

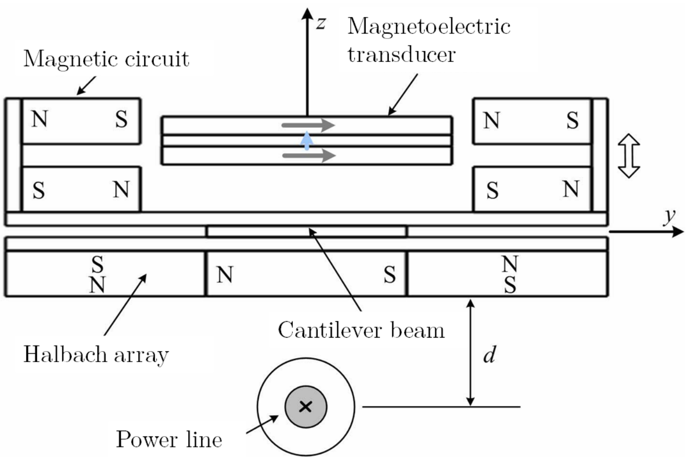

Figure 3.21: Non-contact magnetoelectric generator proposed by He *et al.* [97]

is placed, the magnetoelectric transducer placed in the air gab of the magnetic circuit undergoes the variation of the magnetic field when the power line is energized. The magnetoelectric transducer is a sandwich of a PZT layer (12×6×0.8 mm^3), bonded between two Terfenol-D (12×6×1 mm^3) layers. This non-contact energy harvester, which is placed at a distance of 4 mm from the wire, can produce, at the current of 5 A, a power of 523 μW across an 896 kΩ resistor under the resonant frequency of 50 Hz. Furthermore, the same research group fabricated a similar ME energy harvester from two-wire power cords as shown in Figure 3.20. The harvester employs a magnetic circuit consisting of six NdFeB magnets mounted on the free end of a cantilever beam and a transducer formed of three layered Terfenol-D/PMNT/Terfenol-D layers (12×6×1 mm^3). The vertical Ampere forces acting on the two conductors of the power cord are superimposed. An enhanced movement is then induced on the magnetic circuit. Experimental results demonstrated that 671.2 μW maximum power can be generated with a matching load resistance of 991 kΩ at the current of 6 A [98].

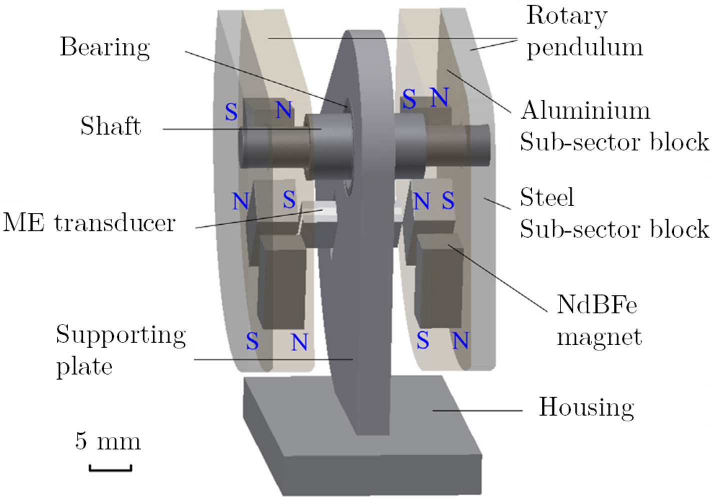

Figure 3.22: Schematic diagram of the vibration-based rotary pendulum harvester proposed by Dai [99]

3.2.5 Rotary pendulum based magnetoelectric converters

A variety of vibration energy harvesters based on pendulums has been reported. Most pendulum-based vibration energy harvesters use electromagnetic [100–104] or piezoelectric [105] transduction mechanisms. Using of pendulum-based converters can improve the working bandwidth of vibration energy harvesting [106–108]. However, magnetoelectric vibration energy harvester with the use of rotary pendulum have rarely been studied. One attempt to develop a pendulum-based broadband vibration energy harvester using ME transducer was reported in [99]. The harvester consists of a ME transducer, a rotary pendulum and a supporting plate as shown in Figure 3.22. In this design, the rotary pendulum is fixed on the supporting plate of the housing through a bearing, and the Terfenol-D/PMN-PT/Terfenol-D transducer (12×6×1 mm^3) is placed between six magnets attached to the rotary pendulum. It is indicated that the harvester has 3 dB bandwidth of 3.2 Hz and frequency-doubling characteristics and can produce high output power of 970.2 μW at 0.5 g RMS acceleration at the resonant frequency of 14.8 Hz.

Table 3.2: Summary of reviewed magnetoelectric harvesters

Architecture	Ref.	Frequency (Hz)	Power (mW)	Acceleration (g)	Note
Cantilever	[83]	51	1.055	1	Terfenol-D/ PZT
	[84]	30.6	1.9015	1	Terfenol-D/PMN-PT
	[85]	26.2	1.44	1	Terfenol-D/PMN-PT Single transducer
	[85]	37	4.07	1.5	Twin transducers
	[85]	29.4	3.95	2	Twin transducers
	[85]	34.8	7.13	2.5	Four transducers
	[86]	20.7	0.1183		Spiral cantilever
	[87]	25.4	0.0688	0.2	Terfenol-D/PMN-PT
	[88]	9.8	0.517		Improvement of [87] Twin transducers
	[89]	38	0.39	0.6	Elimination of magnetostrictive material
	[90]		0.6	0.6	6 mm width transducer
	[90]		0.2	0.6	3 mm width transducer
Spherical magnet	[91]	9.8	0.121	0.061 (RMS)	Terfenol-D/ PZT
	[92]		0.0041		Ni-Mn-Ga/ PZT Shaken by hand/Phone
Magnetic spring	[93]	10	1.1	1	Terfenol-D/ PZT
	[94]	29	0.03		Terfenol-D/ PZT Excitation: 1 mm
Power line	[97]	50	0.523		Terfenol-D/ PZT Use of cantilever One wire power cord
	[98]	50 - 60	0.6712		Terfenol-D/ PZT Use of cantilever Two wire power cords
Rotary pendulum	[99]	14.8	0.970	0.5 (RMS)	Terfenol-D/ PMN-PT 3.2 Hz bandwidth Frequency-doubling

3.3 Summary

Table 3.2 summarizes all presented magnetoelectric converters. The reviewed prototypes are able to generate energy outcomes from 0.0041 mW to 7.13 mW. They are principally based on the use of single ME transducer formed of different types of Ms and PE materials. Furthermore, it is remarked most of these converters, which are still laboratory devices and have relatively big sizes, have been tested under various excitations. Consequently, in most of these cases, it is rather difficult or even impossible to compare their output performances based on the above indicated results. However, it can be observed that for some of these converters, which use similar ME transducer and have similar coupling architecture, the energy outcome is totally different even at comparable excitations.

Figure 3.23 shows the output power relative to the working frequency for a selection of main developed piezoelectric and magnetoelectric transducers. As shown in Figure 3.23, most ME converters have low natural frequency comparing to standard piezoelectric-based harvesters, which makes them more suitable to harvest energy from real applications. There is a continuing debate on the effective architecture and design for converting vibration into electricity based on magnetoelectric effect. However, the design should take in consideration different important parameters including the low frequency, which characterizes most of environmental vibration and mainly the best use of the magnetic field, which requires a detailed investigation of the coupling between the magnets and the Ms layers.

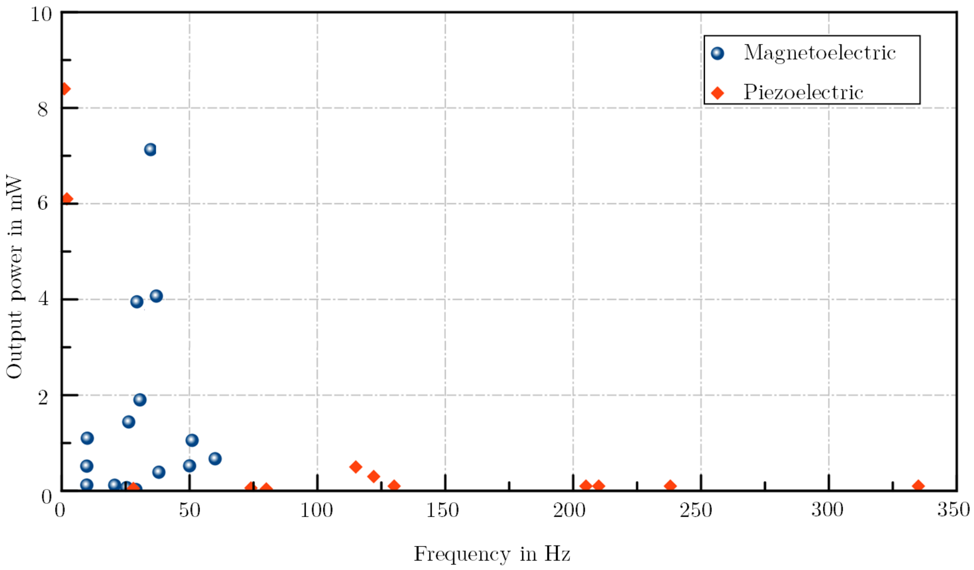

Figure 3.23: Output power relative to the working frequency for main developed magnetoelectric [83–94, 97, 98] and piezoelectric [79, 80, 109–118] vibration transducers prototypes

3.4 Novel approach of designing magnetoelectric transducers

In this thesis, a novel approach is proposed for designing magnetoelectric converters. The aim is to improve to the performance of ME energy converters in response to low amplitude and low frequency vibration, which is the case of most real vibration profiles. In fact, as shown in the previously mentioned researches, it can be concluded that to date developed ME converters operate still well below their maximum possible output performance. This is mainly because of the numerous factors that influence the ME effect in the transducers and the whole converter. Therefore, deep investigations of different influencing parameters in ME converters are required.

We propose a new approach for the design of ME vibration converters, which allows more understanding of the conduction mechanisms from magnetic to electrical energy. FEM is a suitable tool to simultaneously model the different interacting effects. However, material parameters of the anisotropic magnetostrictive material, Terfenol-D, are in general given as a range and most of them depend on the applied magnetic field. In order to ensure coherence between FEM and real values despite of the difficulty of developing an accurate of magnetostriction, a direct measurement of the deformation in a Terfenol-D plate is carried out. For this a novel characterization method is proposed based on AFM measurements. Additionally, the proposed approach is includes the development of an accurate FEM of magnetoelectricity in ME laminate composites, investigation of the adhesive layer and tuning the resonant frequency of the converter.

3.4.1 Investigation of the magnetostrictive effect

In magnetoelectric converters, the contribution of the magnetostrictive layer is decisive since it is able to produce higher mechanical stress than piezoelectric cantilever beam generators. Additionally, a high output voltage from the piezoelectric layer requires high stains generated from the two Ms layers. This would not be possible without ensuring a good coupling between the magnets and the giant magnetostrictive material. However, during operation the two plates undergo a non-uniform time dependent magnetic field, which makes the prediction of magnetostriction not evident. Investigation is important in order to examine the interaction between the magnets and the Terfenol-D layers to enhance the induced deformation in the magnetostrictive layer in response to low magnetic field variation, which contributes to improve the efficiency of magnetoelectric vibration converters under low excitation amplitudes.

A measurement method based on Atomic Force Microscopy (AFM) observations is developed to simultaneously investigate the magnetic domains orientation and to track the deformation in a Ms plate under similar static positions as it is used in ME converters. Both longitudinal and transversal magnetostriction can be obtained for different relative positions between the Ms layer and the magnets. Here, the aim is to determine static magnetostriction to evaluate the FEM model of the magnetostrictive effect, which is used for dynamic simulations when coupled with the model of the piezoelectric effect.

3.4.2 Development of a finite element model of ME effect

In order to study the magnetoelectric response in the laminate composite, a three-dimensional model, which can accurately predict the induced voltage in the piezo element as function of the excitation displacement of the magnetic circuit is developed. The model contains different interactions in the ME converter including magnetostriction and piezoelectricity.

It takes into consideration the non-linear behaviour of magnetostrictive and piezoelectric materials. Most of FEM software have a specific module for piezoelectric material. However, modelling of magnetostriction remains a challenge and have to be developed based on the constitutive equation of the magnetostrictive effect and the material properties. To evaluate the developed model of magnetostriction, AFM measurements are employed as a tool to ensure coherence between FEM results and real values.

Once an accurate model of the magnetoelectric effect in laminate composite is developed, different geometrical parameters, materials and scenarios can be evaluated. Specifically, the performance of the ME transducer can be determined for different magnetic circuit designs in terms of the shape, dimensions, and the direction of magnetization of the magnets. Furthermore, the incorporation of moving mesh feature in the model allows to investigate the dynamic response of the transducer under harmonic excitations through a time dependent analysis by creating a variable magnetic field acting on the ME composite. The model is also be employed to study different important parameters including the magnetic field distribution, the induced deformation in the magnetostrictive layers, the transmitted deformation to the inner piezoelectric plate, and the induced voltage. This allows to select optimal design parameters, which leads to enhance the converter performance.

3.4.3 Investigation of the adhesive

For the fabrication of the ME laminate composite, the bonding adhesive should guarantee simultaneously strong mechanical and electrical properties of the composite. Three different adhesive layers are proposed in this work. The first is similar to a one solution presented in [91], which is based on the use of a conductive epoxy resin, which needs to be cured at 65 °C for 2 h under mechanical load.

Another solution is proposed in this work based on the use of carbon nanotubes (CNTs) with different concentrations mixed to an epoxy resin. The aim is to ensure good mechanical and electrical properties of the composite without applying relatively high temperatures, which may cause depolarization of the piezoelectric layer. CNTs/epoxy dispersions can be cured at room temperature and has good electrical properties. Therefore, bonding the magnetostrictive and the piezoelectric layers is performed using CNTs/epoxy. The performance of the ME converter bonded with different epoxy with different CNTs concentrations is evaluated to select the suitable adhesive layer, which can ensure better load transfer.

3.4.4 Simple tuning of the resonant frequency of the converter

In order to harvest energy from real vibration profiles, the converter should be able to work for wide frequency band instead of resonant one. Non-liner forces presented in the ME converter can contribute to increase the working bandwidth of the converter. Most of developed ME harvesters use this property to increase the working bandwidth for a fixed configuration.

In magnetoelectric converters, varying the relative position between the magnetic circuit and the transducer results on changes of the interaction forces between these two parts due to the non-liner distribution of the magnetic field. The idea here is to benefit from these changes not only to improve the output energy but also to vary to resonance frequency of the converter.

In this work, the resonance frequency of the converter can be tuned by adjusting the separation distance by a simple screw/nut system. This opens new perspectives to use the same design to harvest energy from different environmental vibration sources with different characteristic frequencies.

CHAPTER 4

Experimental investigation of the magnetostrictive effect

In this chapter, a method for magnetostriction measurement in a Terfenol-D plate is proposed and investigated. Induced deformation in the sample plate, when placed in similar conditions as in ME converters, are studied by Atomic Force Microscopy (AFM). The evolution of magnetic domains as well as longitudinal and transversal magnetostriction in the sample are investigated with and without applied magnetic fields. In addition, the magnetic field distribution in the Terfenol-D layer is studied using finite element method and the correlation between the AFM experimental measurements and the FEM simulation of the magnetic field is investigated.

4.1 Methods for magnetostricton measurement

To date, several attempts have been made to investigate magnetic domains and to measure magnetostriction by different methods and different performances. Several techniques have been adopted to directly measure the deformation in magnetostrictive materials in response to an applied magnetic field including local probe technique, strain gauges, and laser displacement sensors. The use of local probe techniques e.g., AFM have shown an increasing interest due to their relatively high resolution, which may reach sub-nanometer. Local probe techniques and especially AFMs have been employed in the characterization of the surface topography of different kind of magnetostrictive materials as shown in the works by Lord et al. [119], Wittborn et al. [120], Tomiczek et al. [121] and Meier et al. [122]. However, direct measurement of magnetostrcition in general still present a big challenge since the expected deformations are in the range of tens of ppm (Atulasimha et al. [123]).

The first direct measurements of the deformations in Terfenol-D surface caused by magnetostrictive lattice strains magnetostriction using a scanning probe microscope was reported by Holden et al. [124] performed on Terfenol-D rods. Papageorgopoulos et al. proposed a new approach to measure magnetostriction of samples with linear dimensions below 100 µm by atomic force microscopy adapted for the application of magnetic field [125]. Furthermore, a method for direct measuring the magnetostriction of ferromagnetic films, which were deposited on non-magnetic substrates by atomic force microscopy was suggested by Harin et al. [126]. Another AFM-based method for measuring the change of dimension in a 10 µm individual Fe-Ga/Cu nanowire was proposed by Park et al. [127]. However, in the previous mentioned literatures, magnetostriction have been only measured in samples with dimensions in the range of some micrometers since most AFMs feature have only a limited scan range, which not exceed 100 µm because of the limitations of piezo actuated scan stages commonly used in AFMs.

In this chapter, a novel method to measure magnetostriction by atomic force microscopy for macro scale samples based on the evaluation of the evolution of easily identifiable features when applying an external magnetic field. The longitudinal magnetized Terfenol-D plate is placed between two rectangular NdFeB magnets. The evolution of magnetic domains as well as longitudinal and transversal magnetostriction of a longitudinal magnetized Terfenol-D plate are investigated using AFM with and without an applied magnetic field for two different positions. In addition, the magnetic field distribution and the displacement in the material are investigated using finite element method.

4.2 Terfenol-D surface morphology

The studied sample consists of a Terfenol-D plate ($Tb_{0.3}Dy_{0.7}Fe_2$, Etrema Products, Inc., USA) of 12 mm length, 6 mm width and 1 mm thickness magnetized along its length direction. One of the two 12 × 6 mm^2 surfaces of the sample was investigated first using an ultra-high-resolution field-emission scanning electron microscope (SEM, Nova NanoSEM 200) to depict its topography.

SEM micrographs are shown in Figure 4.1 with different magnifications. At lower magnification, the anisotropy of the material is clearly observable since different structures with different sizes are presented (Figure 4.1 (a)). At higher magnification, observations show the presence of easily identifiable features on the surface under investigation (Figure 4.1 (b)).

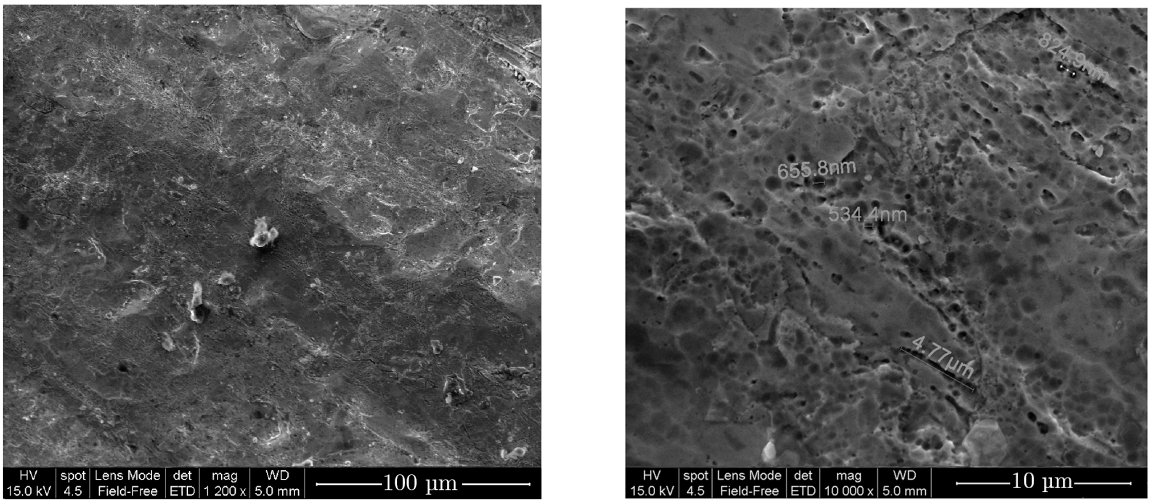

(a) **(b)**

Figure 4.1: SEM morphology of the Terfenol-D plate (a) lower magnification, and (b) higher magnification

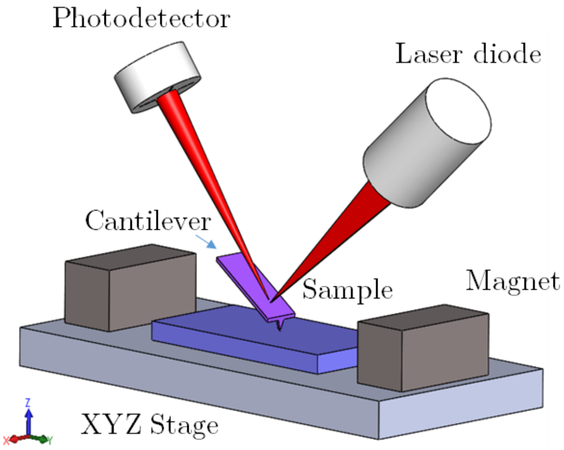

Figure 4.2: Schematic of the AFM investigations [128]

4.3 Experimental procedure

A schematic of AFM investigations to measure the magnetostrictive shifts is shown in Figure 4.2. The experimental setup, the adopted methodology to measure magnetostriction and the selection of the minimum dimensions of the investigated positions are detailed in the following sections.

4.3.1 Experimental setup

The used experimental setup is as shown in Figure 4.3. The setup consists of an Agilent 5600 LS atomic force microscope equipped with controller, a stage controller, a head electronic box and a computer. The sample is fixed on the xyz stage. Two magnets are placed 2.5 mm from both sides of the plate along its length and the surface topography was investigated using the intermittent contact (tapping) mode, typically referred to AC mode of the AFM due to the alternating contact of the tip to the surface.

A stiff cantilever of 40 N/m with a resonance frequency of 300 kHz is chosen. The cantilever is driven to oscillate by an integrated piezo actuator. Instead of deflection (contact force), the amplitude of the forced oscillating lever is detected, analyzed, and utilized in the feedback loop.

The AFM images presented in this chapter have all been produced with an Agilent 5600 LS atomic force microscope at room temperature.

4.3.2 Methodology

In order to measure magnetostriction in the Terfenol-D plate, the evolution of these easily identifiable features is examined with an atomic force microscope when applying an external magnetic field.

Figure 4.4 presents a cross section of the magnets and the Terfenol-D plate. The sample was attached from its center to the XYZ stage of the AFM. The two neodymium magnets (6.3 mm × 3.2 mm × 3.2 mm) are of grade N42 characterized with a remnant

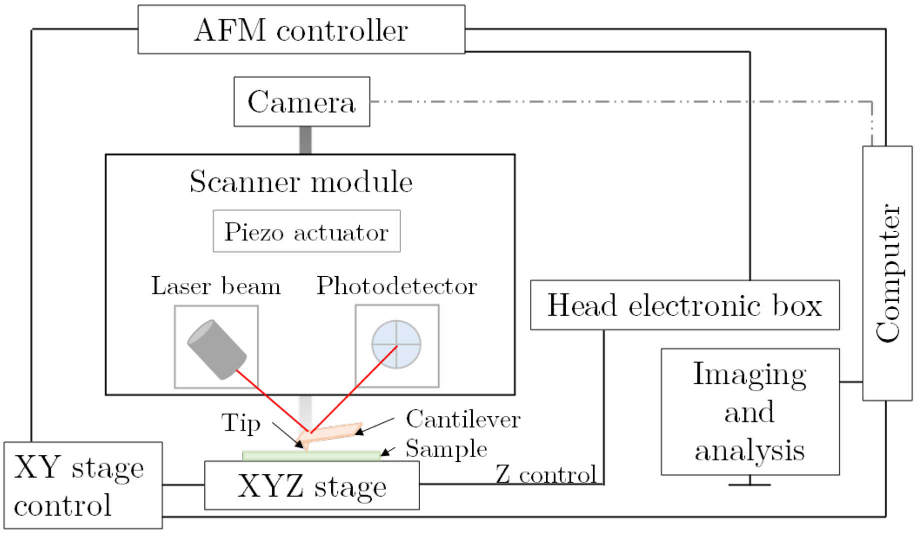

Figure 4.3: Schematic of the experimental setup

flux density of 1.32 T. Their magnetic poles are aligned along y axis and have the same direction to produce a magnetic field distrubition as used in magnetoelectric converters (see Figure 4.5).

The magnetostrictive response was studied for four different positions; $h = 1$ mm, $h = 3$ mm, $h = 4$ mm and $h = 6$ mm.

The surface of the Terfenol-D pate was first investigated with external magnetic field. Once the scanning process was done, the magnets are removed, and the surface was imaged without removing the contact between the sample and the tip.

Because the xyz stage of the AFM is metallic and contains a small magnetized area, the magnetic field density strength B was measured using a digital teslameter (FM 210). Results demonstrate that B on the examined area varies from 0.08 mT to 35.4 mT. The proposed investigations are performed on a position where B is minimal so that only the effect of the magnets is studied.

For each h value, one position on the upper $x - y$ surface of the sample is investigated

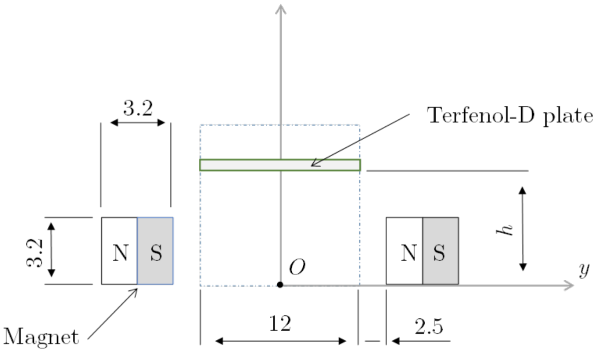

Figure 4.4: Cross section of the magnets and the Terfenol-D plate

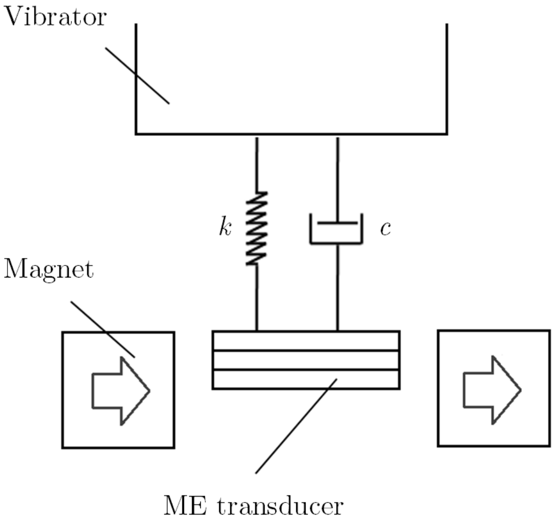

Figure 4.5: Schematic of the operating principle of a magnetoelectric vibration converter [128]

with and without magnets. The positions are chosen randomly, and their coordinates are determined based on the AFM video camera view and the coordinates of the sample in the xyz stage. The origin of coordinate is chosen in the center of the upper $x - y$ surface of the Terfenol-D plate where the sample was attached to the xyz stage. The different heights in the topographic images are used as references to measure the shape deformations along x and y axes, which refer to the longitudinal and transversal magnetostriction of the Terfenol-D plate. Quantitative measurements of the surface shifts are done based on several comparisons between cross sections taken from the topographic images. Figure 4.6 presents a detailed description of the developed approach to measure magnetostriction by atomic force microscopy.

4.3.3 Size of the investigated position

The examined areas size is fixed to be 9 $\mu m \times 9$ μm as a result of SEM and finite element investigations. As observed in SEM morphology images of Terfenol-D, small scan areas of several μm^2 are enough to visualize different features. However, the maximum expected magnetostriction in the 12 mm length plate between the two magnets does not exceed 500 ppm because of the strength of the magnetic field created by the magnets, which has been obtained by finite element simulation for the four configurations. Then, deformations in the plate are estimated to be below 6 μm. For these reasons, 9 $\mu m \times 9$ μm images will be enough for the tracking of the easily identifiable features in the sample surface.

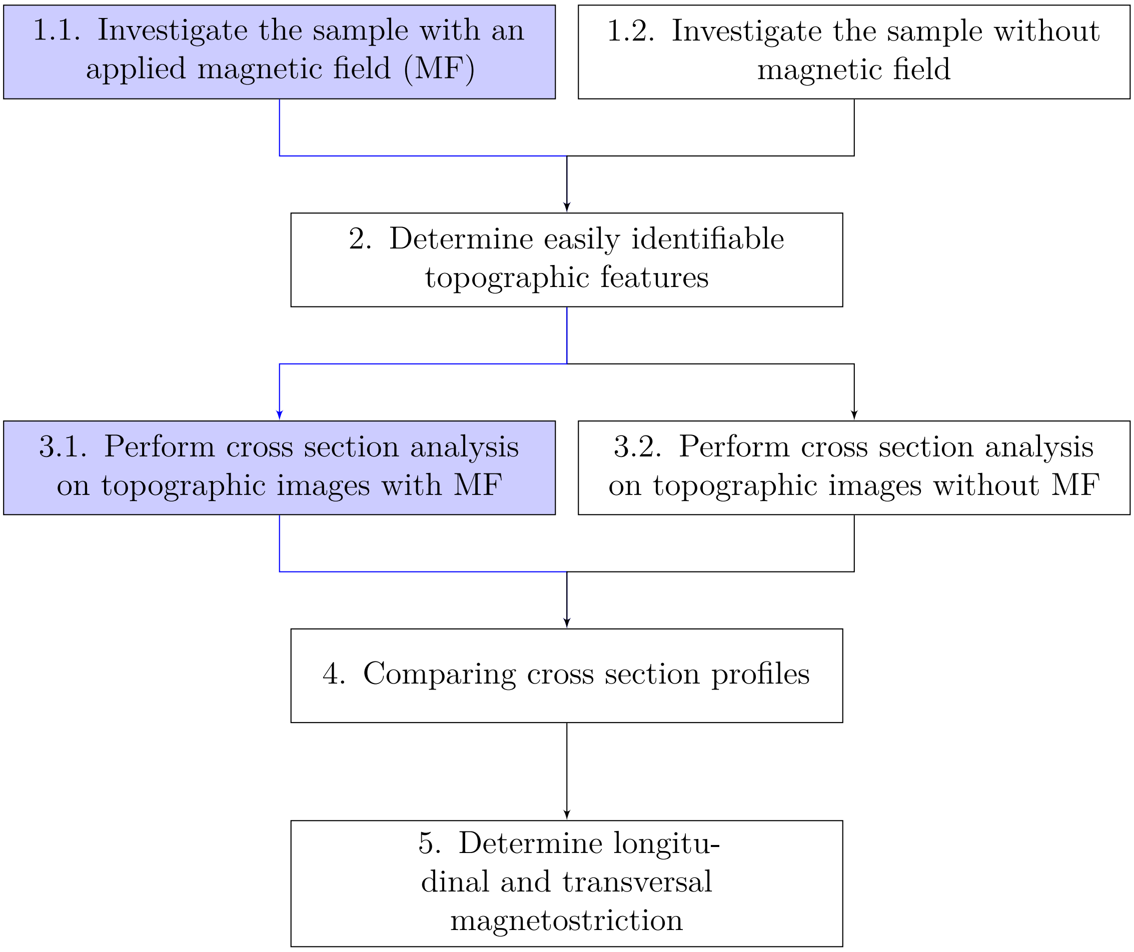

Figure 4.6: Used approach to measure magnetostriction by AFM

4.4 AFM Investigation results

In order to characterize the evolution of magnetic domains, amplitude images are presented for a random position in Figure 4.7. Amplitude images are similar to topography images showing the map of the slope of the sample, but they represent better height images, which may show more clearly the evolution of the magnetic domains. It is shown that domains are randomly oriented in the case without magnets and the application of the magnetic field yields to domains rotation and better homogeneity in the surface of the sample depending on the applied magnetic field.

The topographic images with and without magnets for all proposed h values are presented in Figure 4.8. Figure 4.9 presents the profiles of the cross sections presented in the topographic images by arrows. They are orthogonal to the investigated surfaces. The directions of arrows depend on the position of the examined area and it is from the fixed part to the free part of the sample. The comparison of cross section profiles parallel to x axis, in both cases without and with magnets, is employed for the prediction of the longitudinal deformation while profiles parallel to y axis are used to determine the transversal one for each h position.

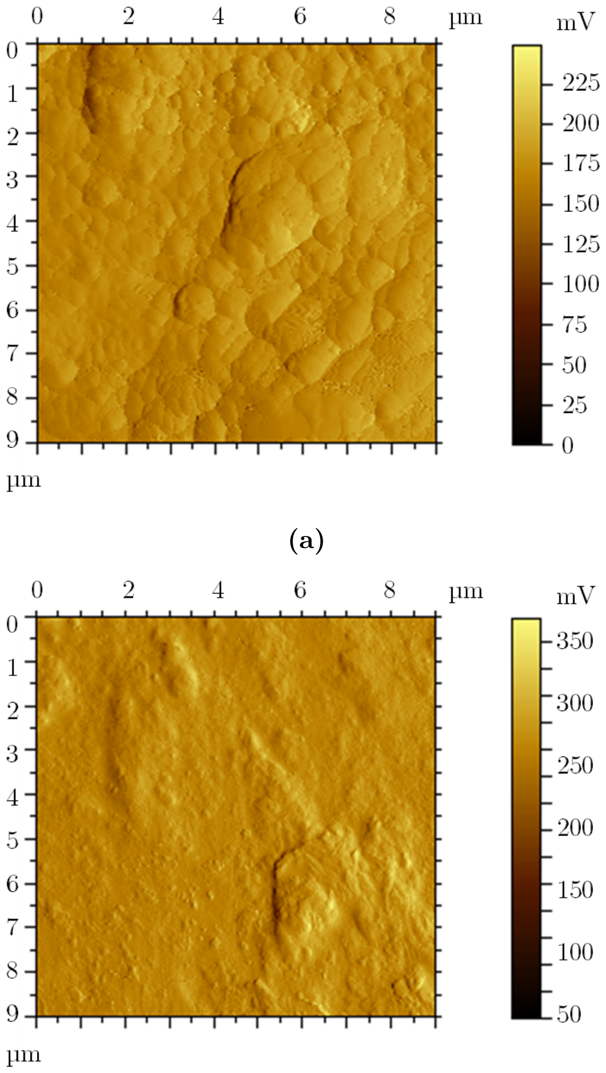

(a)

(b)

Figure 4.7: Example of AFM amplitude images (a) without magnets, and (b) with magnets

Results demonstrate that the magnetic field generated by the two rectangular magnets would result in longitudinal deformations of 2.50, 1.51, 3.20 and -0.19 μm and in transversal deformations of 1.40, 1.98, 0.21 and -0.05 μm for h = 1, 3, 4 and, 6 mm respectively. These results correspond respectively to longitudinal magnetostriction of 208, 125, 266 and -16 ppm and transversal magnetostriction of 233, 330, 35 and -8 ppm.

On the other hand, these results are compared to another set of measurements performed in a different position of the sample in order to determine the influence of the investigated position on the results. Measurements were done for h=3 mm. The results of the comparison are listed in Table 5.3.

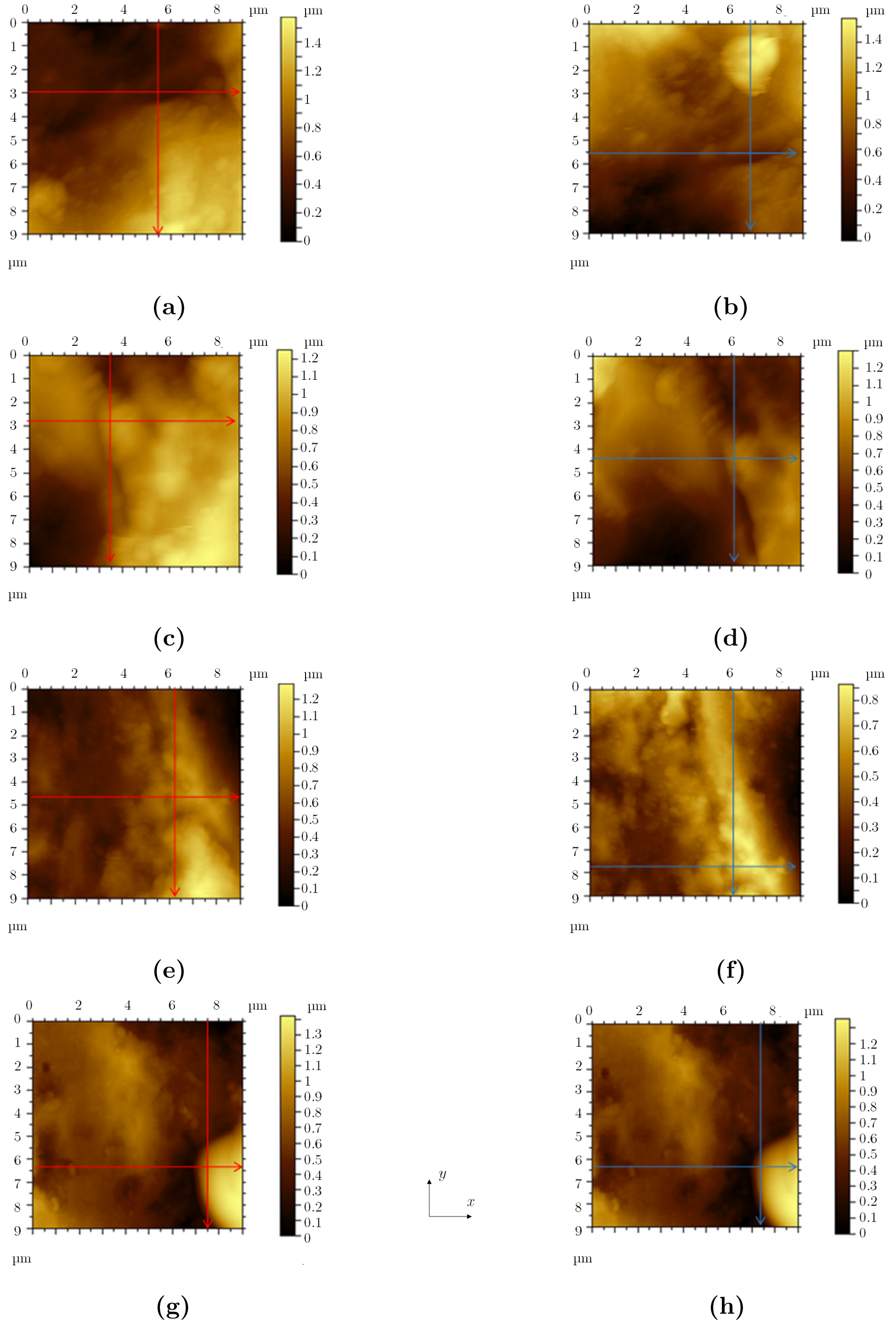

(a) (b) (c) (d) (e) (f) (g) (h)

Figure 4.8: Topographic AFM images in the case without magnets (a) $h = 1$ mm, (c) $h = 3$ mm, (e) $h = 4$ mm, and (g) $h = 6$ mm. Topographic AFM images in the case with two magnets (b) $h = 1$ mm, (d) $h = 3$ mm, (f) $h = 4$ mm, and (h) $h = 6$ mm. Arrows on the topographic images present where the cross sections where taken [128]

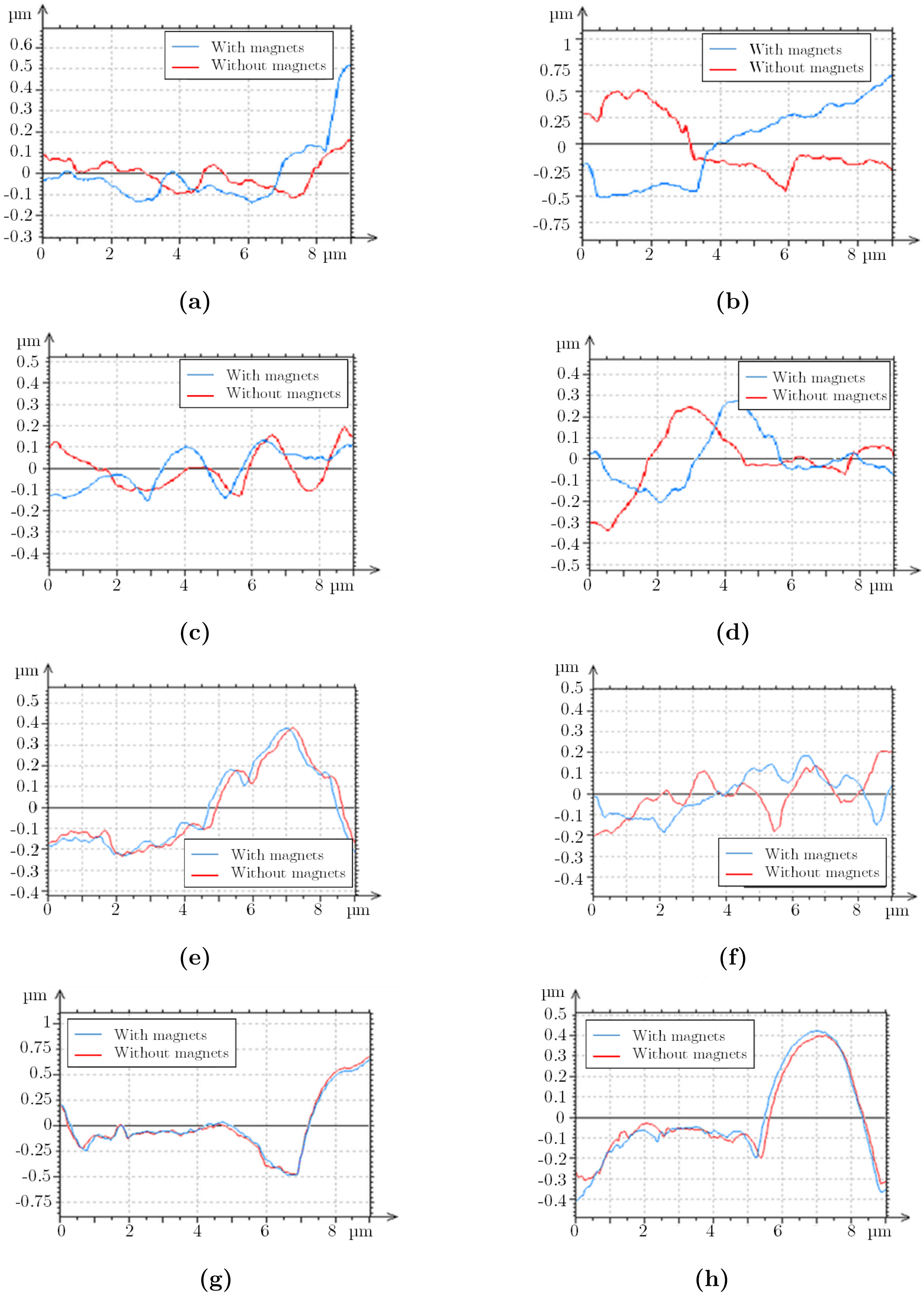

Figure 4.9: Cross sections presented in the topographic images orthogonal to the surface and parallel to y-axis (a) $h = 1$ mm, (c) $h = 3$ mm, (e) $h = 4$ mm, and (g) $h = 6$ mm. Cross sections presented in the topographic images orthogonal to the surface and parallel to x-axis (b) $h = 1$ mm, (d) $h = 3$ mm, (f) $h = 4$ mm, and (h) $h = 6$ mm [128]

It is found that, for $h = 3$, longitudinal and transversal deformations of 2.02 μm and 1.47 μm were obtained, which correspond to deviations of 2 % and 2.6 %, respectively. Comparing those results to the previously obtained values confirm the validity of the proposed approach.

Another factor that is investigated is the history dependence in Terfenol-D. Magnetostriction shifts have been studied first without an applied magnetic field and then after the removal of the field, which has been applied for a short period.

Results are presented in Figure 4.10. The size of AFM topographic images is 7 μm × 7 μm since the two measurements were done without an applied magnetic field. It can be seen that the deformations in the plate are not fully recovered, i.e., magnetic domains before and after magnetization are different. In fact, 0.22 and 0.14 μm are obtained as longitudinal and transversal shifts, respectively.

Table 4.1: Measured deformations in two different positions for $h = 3$ mm

Deformation parallel to x-axis		Error	Deformation parallel to y-axis		Error
Position 1	Position 2		Position 1	Position 2	
1.98	2.02	2%	1.51	1.47	2.6%

4.5 Discussion

AFM investigation results cannot be directly compared to data given by the material supplier or results in previous published works since these latter are always given in the case of static uniform magnetic field. However, there is good agreement between both results. For instance, magnetostriction in the range of 200 ppm was measured by this proposed method when the sample was placed in the air gap between the magnets where the field strength measured by the Teslameter was around 0.05 T. These values are comparable to results given in [129] where 200 ppm magnetostriction was measured in 10 mm square Terfenol-D plates with 1 mm, 3 mm and 5 mm thicknesses under respectively 0.034 T, 0.051 T and 0.088 T. However, detailed analysis of the deformation in the sample with respect to the magnetic field strength and geometry is required to study the magnetostrictive effect.

To that end, we propose to investigate the magnetic field distribution for each of the h values and study the relation between the measured deformation and other magnetic field parameters. In the following section, finite element method is proposed for the analysis of the magnetic field rather than direct measurement since no accurate information about the field distribution can be obtained experimentally.

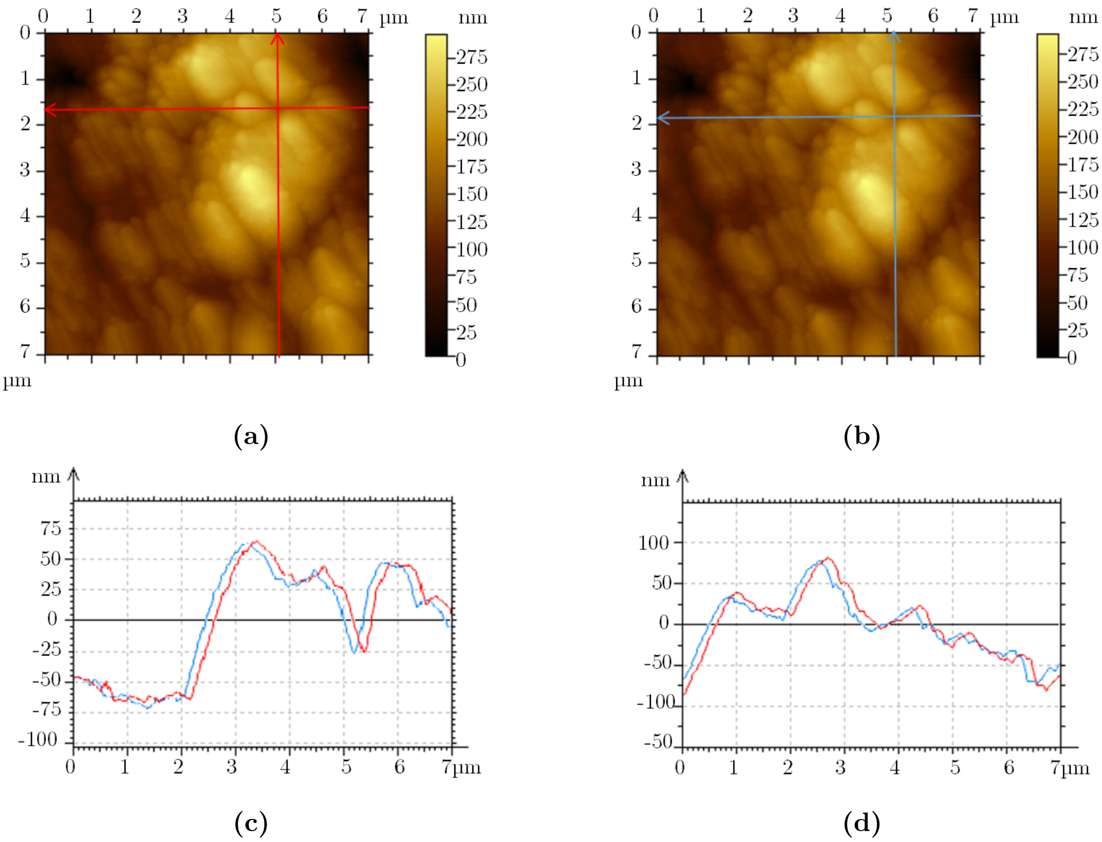

(a) (b)

(c) (d)

Figure 4.10: Topographic AFM images (a) without magnets, (b) after the removal of the magnets. Cross sections orthogonal to the surface of the two configurations (c) parallel to y-axis, (d) parallel to x-axis. Lines on the topographic images present where the cross sections were taken

4.5.1 Finite element analysis of the magnetic field

In this section, a model was implemented in Comsol Multiphysics to simulate the magnetic field and compare findings quantitatively to AFM experimental results. The simulation model contains the Terfenol-D plate, the NdFeB magnets and the metallic stage, which increases the magnetic field.

In the model under consideration, the boundary condition on the outside of the modelling domain is neglected since an air domain enclosed in a region of infinite elements is added to the model. Each magnet is defined by a remnant flux density parallel to y axis of 1.32 T and a relative permeability of 1.09. The used mesh consists of 75932 tetrahedral elements uniformly distributed.

4.5.2 Correlation to magnetic field distribution

Figure 4.11 shows the measured deformations parallel to x and y axis and the x and y magnetic field components variation for each h position. Weak correlation between the evolution of transversal deformations and the magnetic field x component is shown

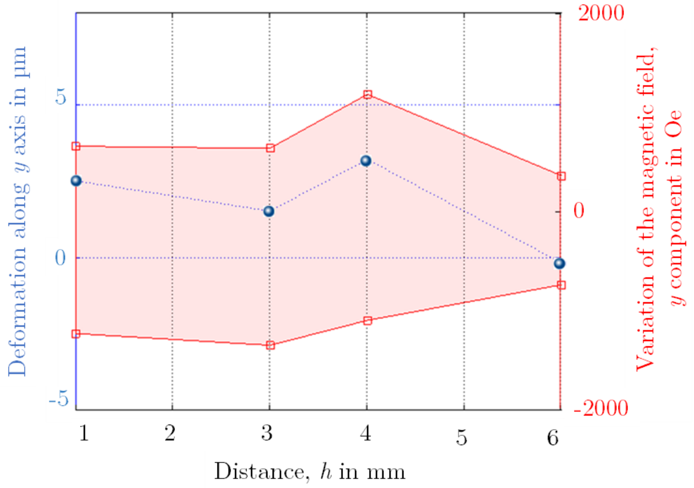

(a)

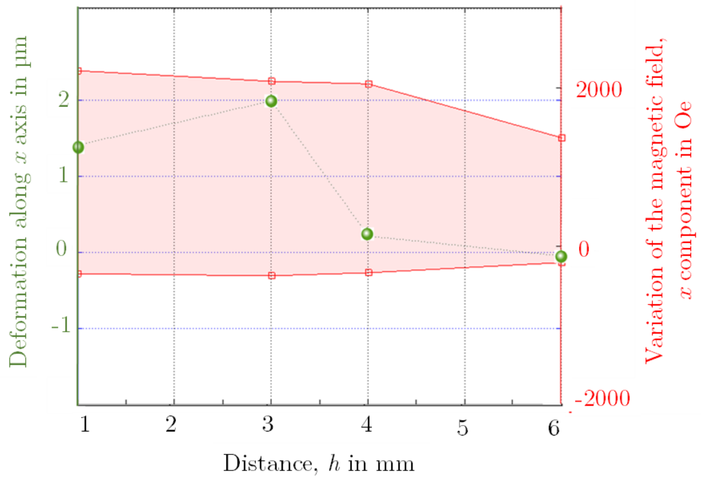

(b)

Figure 4.11: (a) Deformations in the Terfenol-D plate parallel to y axis and variation of the magnetic field y component in the middle longitudinal cross section. (b) Deformations in the Terfenol-D plate parallel to x axis and variation of the magnetic field x component in the middle longitudinal cross section [128]

in Figure 4.11(b). That may be caused by the influence of deformations along the two other axes and the geometric distribution of magnetic field components, which are not considered in this work. However, Figure 4.11(a) shows that the evolution of measured longitudinal deformations in the plate is relatively related to the variation of the magnetic field y component. This result is due to the fact that the magnetic poles of the magnets are aligned along this axis and the plate is placed longitudinally between the magnets.

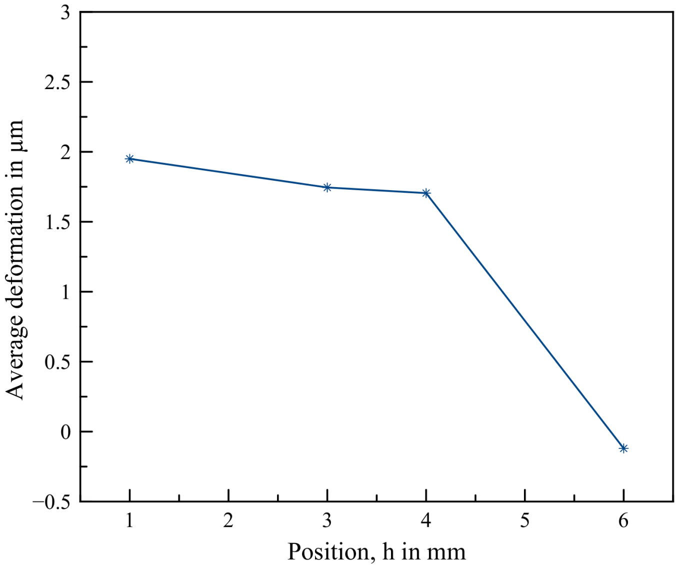

Figure 4.12: Measured average deformation in the Terfenol-D plate

4.5.3 Measured average deformation

The measured average deformation in the Terfeno-D plate for the different investigated relative positions is shown in Figure 4.12. A linear interpolation of the measured values is presented for h between 1 mm and 6 mm. These results will be used in the next chapter in order to compare and evaluate the finite element model of magnetostriction.

4.6 Conslusion

Magnetostriction in a Terfenol-D plate was measured under a non-uniform magnetic field based on AFM topographic and amplitude images. The different heights in the topographic images are used as references to measure the shape deformations parallel to the length and to the width of the plate. The longitudinal magnetostriction and the transversal magnetostriction are measured for different relative height positions of sample in the air gap between two NdFeB magnets. Furthermore, the variation of magnetic field components in the middle longitudinal cross section of the plate is presented based on finite element analysis and the correlation between obtained magnetostriction results and the field components is discussed. In addition, good agreement to previous published results is observed. The average value of the measured deformation will be used in the next chapter as a tool to evaluate the FEM model of magnetostriction.

CHAPTER 5

Model based harvester design

Optimization of magnetoelectric converters performance requires an accurate modelling of the static and dynamic behaviour of different interaction effects in the ME transducer. In this chapter, a finite element model of magnetostriction is developed and corrected based on AFM measurement results. This model is coupled to the simulation of the piezoelectric effect in the piezoelectric layer. Overall, a complete model to predict the induced voltage in the ME transducer as response to the magnet's displacement is defined and used for the design of the harvester.
The developed converter is analysed analytically, and the corresponding governing equation is solved with the Lindstedt-Poincaré method. The effects of the structure parameters, such as the non-linear magnetic forces, the magnetic field distribution and the resonance frequency are discussed, and the electric output performances of the transducer are predicted.

5.1 Finite element model of the magnetoelectric effect

Finite element analyses presented in this section were carried out using COMSOL Multiphysics software. The aim is to simultaneously simulate the coupled physical fields in the magnetoelectric converter.
For the MS effect, COMSOL does not have an interface for modelling magnetostrition. However, it is possible to simulate the response of the Terfenol-D plates by combining COMSOL's structural mechanics and magnetic interfaces. On the other hand, piezoelectricity is modelled based on piezoelectric devices module. Figure 5.1 presents a schematic description of the COMSOL Multiphysics modules used in the simulation.

5.1.1 Modelling of magnetostriction

COMSOL uses a generalized Hooke's law to describe the constitutive relationship between the stress and strain tensors in a solid mechanics problem. To simulate the elastic behaviour of a magnetostrictive material, a combination of solid mechanics and magnetic fields modules is needed. To that end, a relation between magnetostrictive strains and magnetization has to be developed.
Magnetostriction is an anisotropic effect and depends on the stress direction because it is strongly related to crystal symmetry [33]. For the case of Terfenol-D, it solidifies into

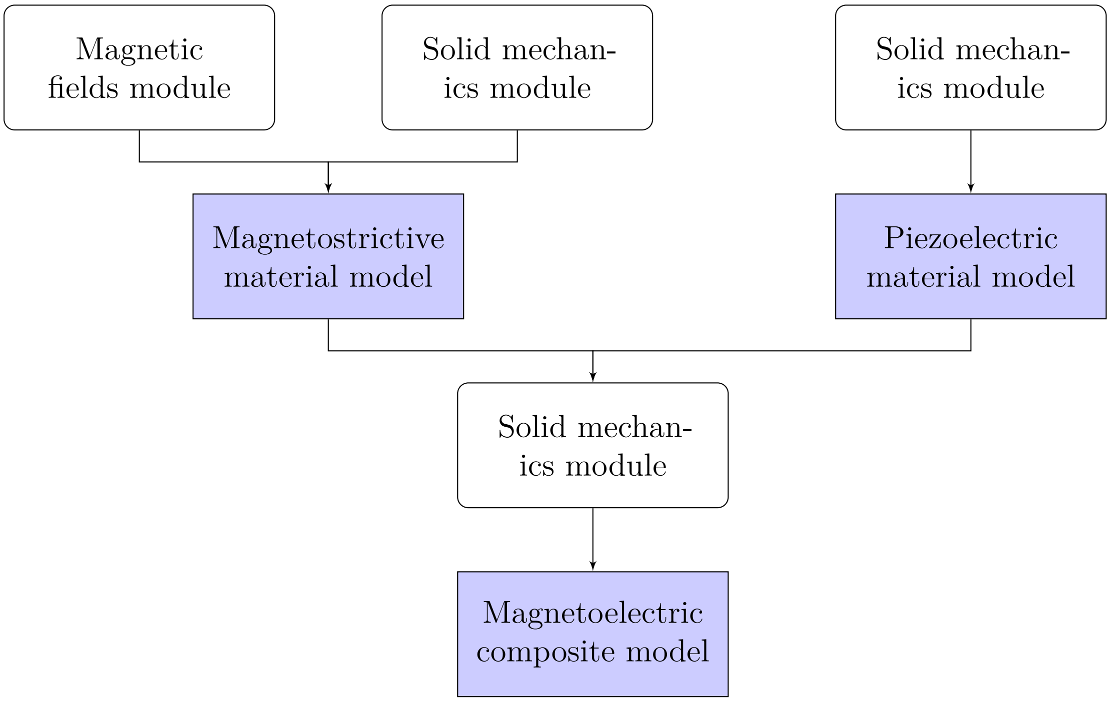

Figure 5.1: Chart of the simulation model in COMSOL

the cubic C15 Laves phase structure [130]. In this case, the magnetostriction along the direction of magnetization can be written as given by Equation 5.1.

$$\lambda = \lambda_{100} + 3(\lambda_{111} - \lambda_{100})(\alpha_1^2\alpha_2^2 + \alpha_2^2\alpha_3^2 + \alpha_3^2\alpha_1^2) \tag{5.1}$$

where λ_{100}, λ_{111} are the saturation magnetization along the directions $< 100 >$ and $< 111 >$ and α_i is the magnetization direction cosine.
By considering Terfenol-D as an isotropic material, Equation 5.1 can be written as given by Equation 5.2.

$$\lambda = \frac{3}{2}\lambda_s(cos^2(\theta) - \frac{1}{3}) \tag{5.2}$$

where λ_s is the saturation magnetization and θ is the angle of magnetization.
Furthermore, the deformation due to magnetostriction along any direction can be considered as a non-linear function of the the direction of magnetization as given by Equation 5.3 [32].

$$\lambda = \frac{3}{2}\lambda_s((\frac{M_i}{M_s})^2 - \frac{1}{3}) \tag{5.3}$$

where M_i and M_s are the magnetization along direction i and the saturation magnetization of the material, respectively. The negative term (-1/3) takes into account the magnetization required to align the individual domains within the magnetostricitve material and for this model it is ignored. Thus, the magnetic effect in MsM can be incorporated by adding anisotropic initial strain but the initial strain terms are

proportional to the magnetization of the material along the corresponding direction. The non-linear magnetic behaviour of Terfenol-D is modelled by using a HB curve to specify the magnetic constitutive relation in the magnetostrictive layers. The used curve in the simulation model is shown in Figure 5.2 [131]. It can provide a value of the magnetic field H for a given magnetic flux density B in the material.
Other physical parameters of Terfenol-D used in the simulation are presented in Table 5.1. In the model under consideration, eddy currents are not taken into account.

Table 5.1: Physical parameters of Terfenol-D used in the simulation

Property	Symbol	Value	Unit
Density [47]	ρ_m	9230	kg/m^3
Poisson's ratio [132]	ν_m	0.5	–
Young's modulus [47]	E_m	30	GPa
Relative permittivity [133]	ϵ_m/ϵ_0	1	–

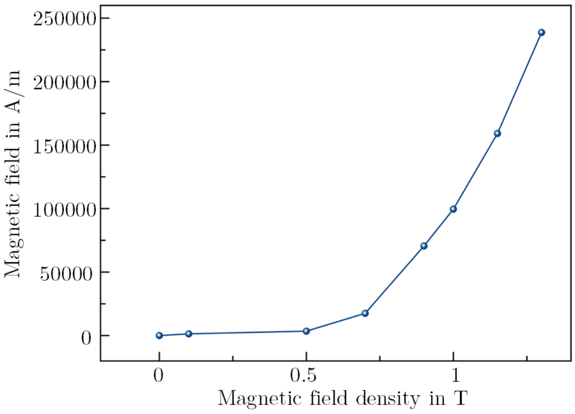

Figure 5.2: HB curve of Terfenol-D [131]

Thus, the electric conductivity of Terfenol-D is assumed to be equal to 0 using similar approach as given in [134].

5.1.2 Modelling of piezoelasticity

In order to model the PE effect in the piezoelectric layer in COMSOL, the Piezoelectric Devices interface is used. It combines Solid Mechanics and Electrostatics features. In this case, the coupling between the mechanical excitation and the output voltage can be defined as stress-charge or strain-charge form. Equations 5.4 and Equations 5.5 present the coupled constitutive equations for piezoelectric materials in case of stress-charge or strain-charge form respectively [135].

$$\left\{ \begin{array}{l} \sigma = c^E \epsilon + e_c^T E \\ D = e_c \sigma + \epsilon_0 \epsilon_p^\epsilon E \end{array} \right\} \tag{5.4}$$

$$\left\{ \begin{array}{l} \epsilon = s^E \sigma + d^T E \\ D = d\sigma + \epsilon_0 \epsilon^\sigma E \end{array} \right\} \tag{5.5}$$

where σ, ϵ, E and D denote the stress, the strain, the electric field and the electric displacement, respectively. c^E is the elasticity matrix, ϵ_p^ϵ is the permittivity matrix and e_c and d_c are the coupling matrices. The superscripts E, σ and ϵ indicate that the parameters were measured at a constant electric field, stress, and strain, respectively. e_c^T and d_c^T refer to the transpose matrices of e_c and d_c, respectively.

In COMSOL, both material properties and material orientation need to be defined to build the model.

In case of strain-charge form, the components of the compliance matrix, s^E, the piezoelectric coupling matrix, d_c and the relative permittivity matrix, ϵ^σ, are required. The simulation model is developed using PMNT as piezoelectric material. Due to the crystallographic structure of PMNT, a total of eleven independent constants are needed as presented in Equation 5.6, Equation 5.7 and Equation 5.8.

$$s^E = \begin{bmatrix} s_{11}^E & s_{12}^E & s_{13}^E & 0 & 0 & 0 \\ s_{12}^E & s_{11}^E & s_{13}^E & 0 & 0 & 0 \\ s_{13}^E & s_{13}^E & s_{33}^E & 0 & 0 & 0 \\ 0 & 0 & 0 & s_{44}^E & 0 & 0 \\ 0 & 0 & 0 & 0 & s_{44}^E & 0 \\ 0 & 0 & 0 & 0 & 0 & s_{66}^E \end{bmatrix} [m^2 N^{-1}] \tag{5.6}$$

$$d_c = \begin{bmatrix} 0 & 0 & 0 & 0 & d_{c15} & 0 \\ 0 & 0 & 0 & d_{c15} & 0 & 0 \\ d_{c31} & d_{c31} & d_{c33} & 0 & 0 & 0 \end{bmatrix} [CN^{-1}] \tag{5.7}$$

$$\epsilon^\sigma = \begin{bmatrix} \epsilon_{11}^\sigma & 0 & 0 \\ 0 & \epsilon_{11}^\sigma & 0 \\ 0 & 0 & \epsilon_{33}^\sigma \end{bmatrix} [Fm^{-1}] \tag{5.8}$$

The material constants of PMNT used in the simulation are given in Table 5.2. Other material properties of PMNT are given in Table 5.3.

The poling direction is a very important parameter for the modelling of piezoelectric layer. For instance, in case of a coordinate system (x_1, x_2, x_3), the matrix components for the PE material properties are related to this coordinate system, where the poling direction is along the x_3-axis. Changing the poling direction requires adding a local coordinate system in the material settings to rotate the piezo-ceramic material.

In this model, the PMNT plate has initially a poling direction along its thickness (z-axis).

Table 5.2: Material constants of PMNT used in the simulation [136]

Matrix	Independent constant	Value	Unit
Elasticity matrix	s^E_{11}	41.4	10^{-12} m^{2}N^{-1}
	s^E_{12}	-22	
	s^E_{13}	-19.4	
	s^E_{33}	47.5	
	s^E_{44}	15.1	
	s^E_{66}	24.9	
Piezoelectric charge matrix	d_{c31}	-549	10^{-12} CN^{-1}
	d_{c33}	1282	
	d_{c15}	169	
Dielectric constants	$\epsilon^{\sigma}_{11}/\epsilon_0$	1821	-
	$\epsilon^{\sigma}_{33}/\epsilon_0$	4841	

Table 5.3: Material properties of PMNT used in the simulation

Property	Symbol	Value	Unit
Density [55]	ρ_p	8100	kg/m^3
Poisson's ratio [137]	ν_p	0.32	
Young's modulus [138]	E_p	20	GPa
Electrical conductivity [139]	ϱ	1.9 10^{-10}	S/m

5.1.3 Implementation of the finite element model

In addition to the model of MS and PE effect in COMSOL, the magnets, their movement and resistive loads are included in the proposed model. The magnets are defined by a remnant flux density of 1.32 T and a relative permeability of 1.09 using the magnetic fields feature. A moving mesh is implemented for the oscillation of the magnets.
A summary of multiphysics coupling in the proposed model is shown in Figure 5.3.
In the model under consideration, an air domain is established around the proposed geometry to realistically model the system as shown in Figure 5.4.

5.1.4 Correction of the finite element model

Based on the proposed FEM model, the magnetostrictive response in one Terfenol-D plate is measured by a parametric sweep study when it is placed in the four different positions, which have been measured by AFM; $h = 1$ mm, $h = 3$ mm, $h = 4$ mm and $h = 6$ mm. For each case, the average deformation in the plate is measured and compared to the average value found by AFM investigations.

Results indicate that the variation of the average deformation is relatively similar for both AFM and FEM analysis. However, the magnitude of the displacement is different.

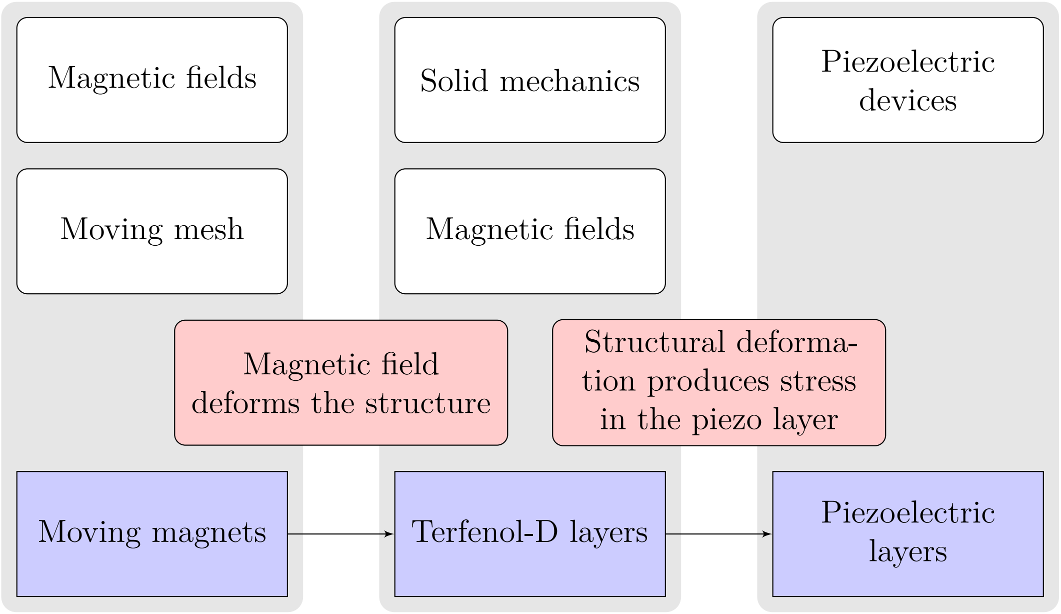

Figure 5.3: Summary of the multiphysics coupling

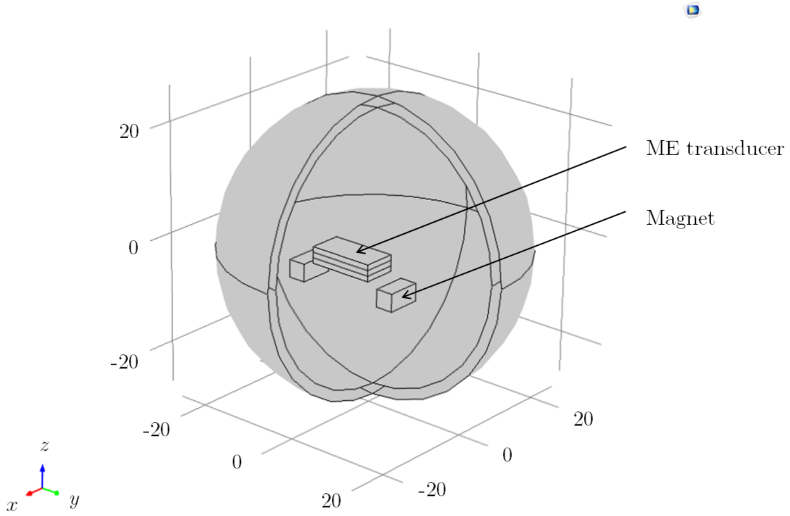

Figure 5.4: Simulation model used for comparison with AFM results

In order to improve the finite element model of magnetostriction, a correction factor, k_f, is introduced to the deformation due to magnetostriction. Therefore, Equation 5.3 can be written as given in Equation 5.9.

$$\lambda = \frac{3}{2} k_f \lambda_s (\frac{M_i}{M_s})^2 \tag{5.9}$$

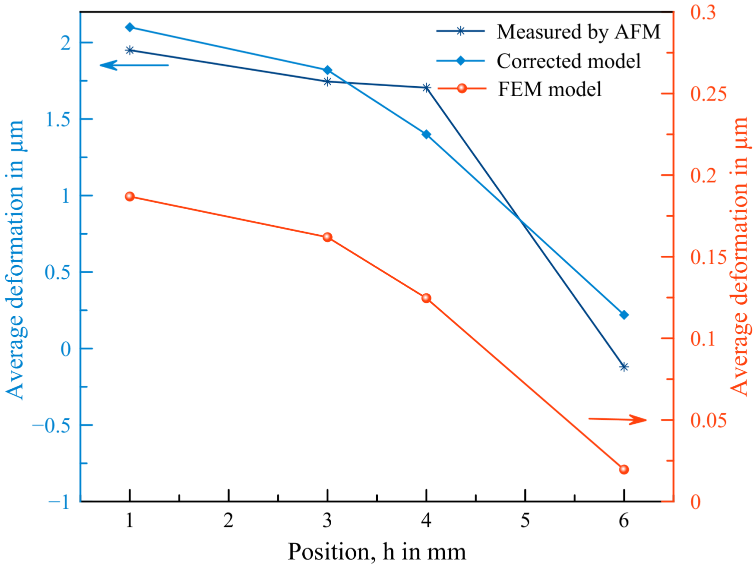

Figure 5.5: Average deformation in the Terfenol-D plate

Deformations in the Terfenol-D plate found by FE analysis, AFM investigations and the corrected FE model are presented in Figure 5.5.
For the following investigations, only the corrected FE model is considered.

5.2 Finite element analysis

The developed model is used to investigate different important parameters for the design of the converter including, the magnetic circuit, the optimal initial position of the transducer, and the direction of polarization and the material properties of the piezoelectric layer.

5.2.1 Magnetic circuit design

In this section, the investigation of the magnetic circuit can be divided in two parts, which are the evaluation of the magnet geometry and the evaluation of the magnets arrangement and their magnetization direction.

5.2.1.1 Influence of the magnet geometry

As discussed in chapter 3, the main used geometries for the magnets used in the magnetic circuit are rectangular or cylindrical-hollow. In this section, the developed model for the magnetostrictive and the piezoelectric materials is used in order to investigate the performance of the ME transducer when placed in the air gap of two magnetic circuit designs based on rectangular and cylindrical-hollow magnets. The simulation models of the two configurations are presented in Figure 5.6.

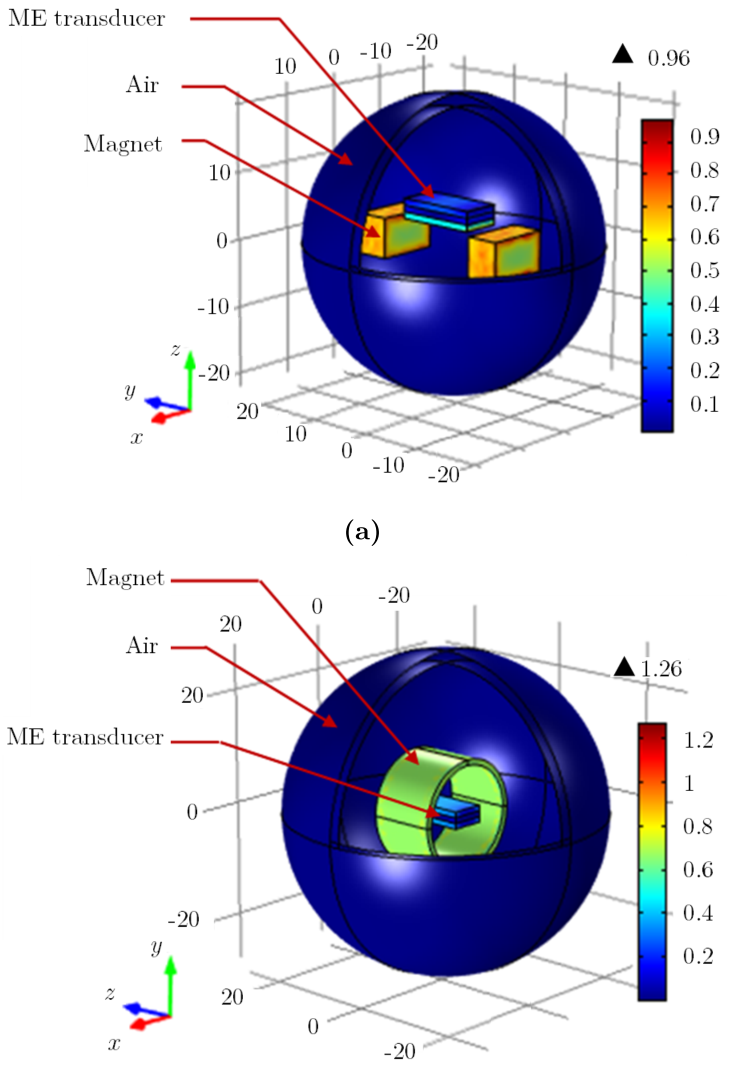

(a)

(b)

Figure 5.6: Simulation model. (a) Magnetic circuit formed of two rectangular magnets. (b) Magnetic circuit formed of a hollow magnet

The ME transducer consists of one piezoelectric plate between two Terfenol-D plates. All layers are of 12 mm length, 6 mm width and 1 mm thickness. In the case presented in Figure 5.6 (a), the magnetic circuit is formed by two rectangular magnets (10 mm × 6 mm × 5 mm). In the second case, the ME transducer is placed inside the cavity of a hollow magnet (10 mm length, 10 mm outer diameter and 9 mm inner diameter) as shown in Figure 5.6 (b). All used magnets were defined by a relative permeability of 1.09 and 1.32 T remnant flux density parallel to z-axis.

In both cases, an air domain is added to the model in order to eliminate the effect of the boundary condition outside of the modelling domain.

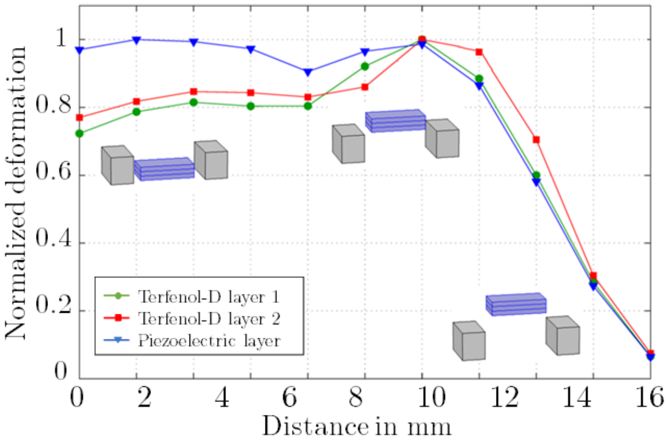

(a)

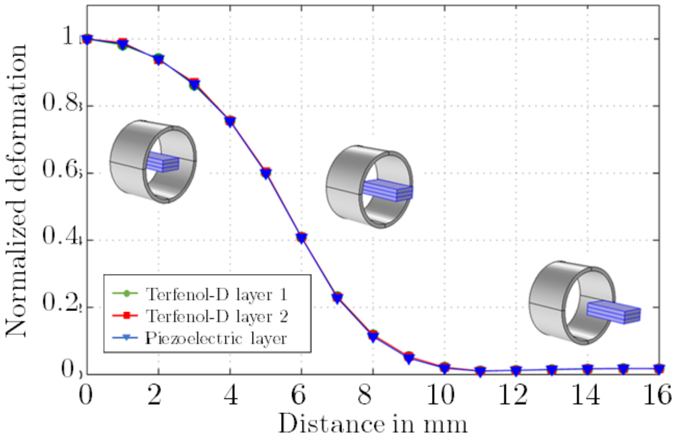

(b)

Figure 5.7: Average deformation in the three layers versus the position of the transducer. (a) Magnetic circuit formed of two rectangular magnets. (b) Magnetic circuit formed of a hollow magnet

Figure 5.7 presents the simulation results. It can be seen in Figure 5.7 (a) that the induced deformation in the two Terfenol-D layers are not identically the same due to the position of the magnets in the air gap of the two rectangular magnets. In this configuration placing the transducer initially directly above the magnets induces more variation of deformation and then voltage comparing to other relative positions between the magnets and the laminate composite.

For the second case (Figure 5.7 (b)), the deformation in the two Terfenol-D plates are similar due to the presence of a symmetry axis in case of a hollow magnet. In this case the transmitted deformation to the piezoelectric layer have also similar variation.

Since the ME transducer is able to generate more energy outcome by increasing the variation of the deformation in the piezoelectric layer, FE results prove that placing a part of the transducer (ideally the half) inside the cavity of the hollow magnet presents the optimal initial position of transducer for this magnetic circuit configuration. Although the use of a hollow magnet have the advantage of generating similar deformation in the three layers of the transducer (i.e., it can be easier to control and optimize), simulation results proves that placing the ME transducer in the air gap between the two rectangular magnets having the same magnetization direction along the axis parallel to the length of the transducer can induce more deformation to the transducer. In the following sections, the focus is to investigate several parameters in different magnetic circuit designs based on rectangular magnets using the developed model of the ME effect in COMSOL Multiphysics. The dimension of all magnets are 6.2 mm × 3.2 mm ×3.2 mm.

5.2.1.2 Influence of the magnets arrangement and their magnetization direction

- Two-magnets magnetic circuit design

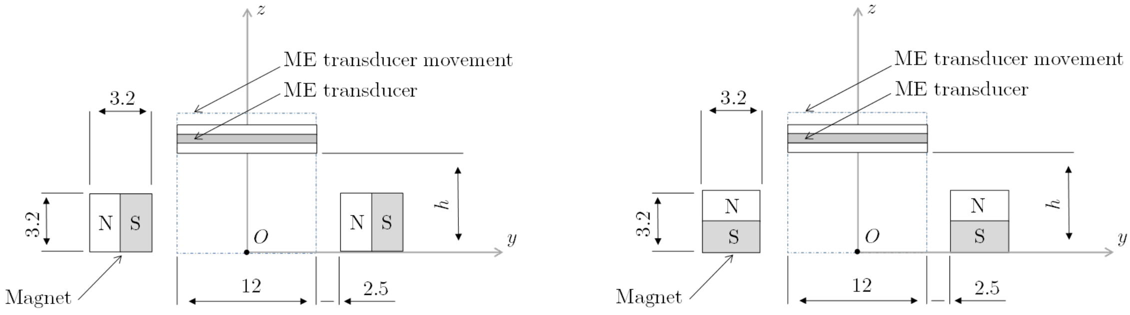

(a) **(b)**

Figure 5.8: Schematic of the proposed finite element investigation with two magnets magnetic circuit design: (a) Configuration A1; (b) Configuration A2

The magnetic circuit should provide the transducer to work in the optimum condition of the magnetic field, i.e., the ME transducer should undergo large enough magnetic field variations at small relative displacements. Therefore, finite element method is used to predict and analyse the magnetic field in the magnetostrictive layers. A schematic of the proposed simulation is presented in Figure 5.8. The aim is to study the effect of changing the direction of magnetization of the magnets on the induced deformation in the ME transducer. Two configuration are studied:

- Configuration A1: The magnetization direction of the two magnets is along the horizontal axis (y-axis) and with the same direction (Figure 5.8 (a)).

- Configuration A2: The magnetization direction of the two magnets is along the vertical axis (z-axis) and with the same direction (Figure 5.8 (b)).

In the model under consideration, the transducer is placed at $h = 3$ mm (selected based on AFM investigation results) and a time dependent analysis is performed for one oscillation period of the magnets with an amplitude of 1 mm. The variations of the average magnetic field density in the upper and the lower Terfenol-D layers for the two configurations are shown respectively in Figure 5.9 (a) and Figure 5.9 (b). The variations of the average deformation in the two Terfenol-D layers and in the

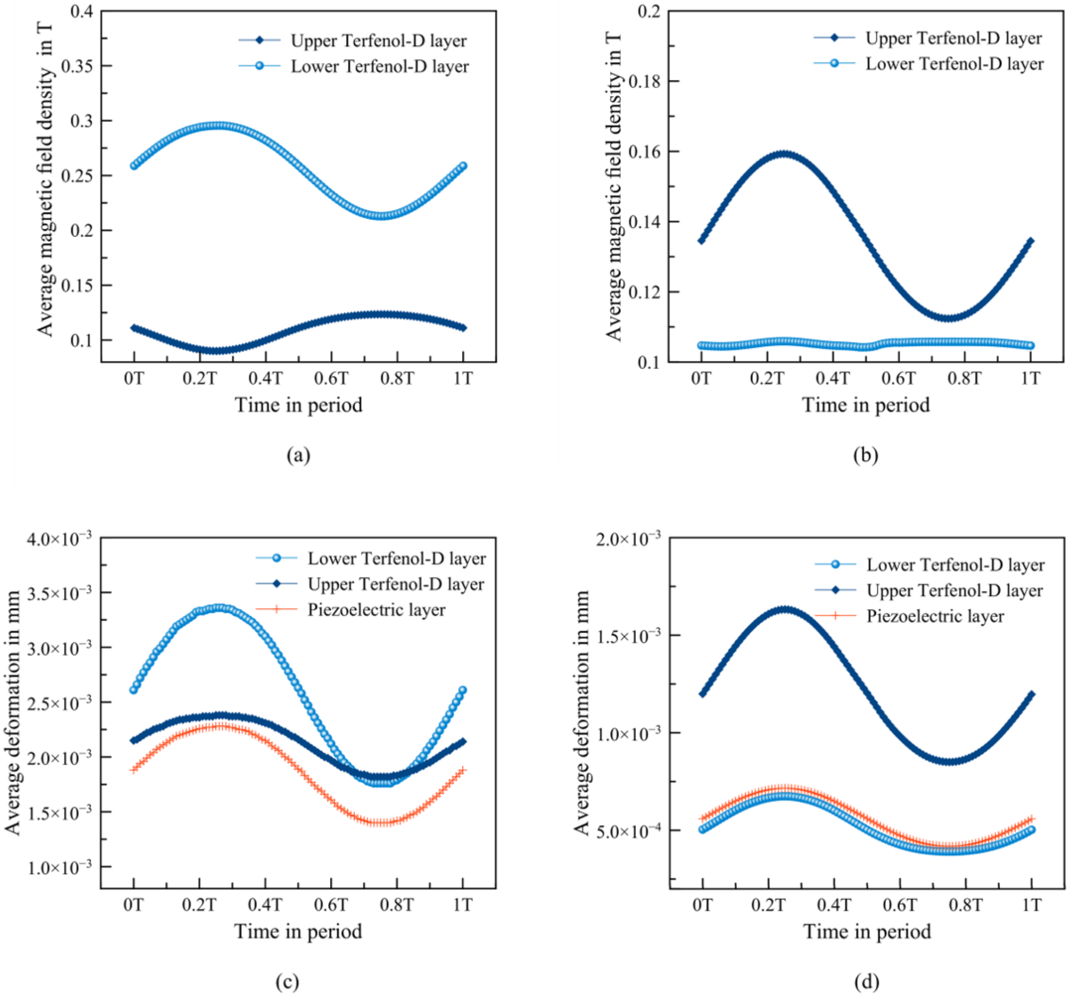

(a) (b) (c) (d)

Figure 5.9: Variation of the average magnetic field density in (a) configuration A1, and (b) Configuration A2. Variation of the average deformation in the three layers (c) Configuration A1, and (d) Configuration A2

piezoelectric layer are presented in Figure 5.9 (c) and Figure 5.9 (d) for the two simulated configuration, respectively. It is remarked that for the two cases, the magnetic field density is different in the upper and the lower magnetostrictive layer due to their initial positions in the air gap and the non-linearity of the magnetic field generated by the magnets. Moreover, the induced deformation in the two Terfenol-D plates has different magnitude and profile, which influence the transmitted deformation to the piezoelectric layer. For instance, the variations of the average deformation of the piezoelectric plate in the first configuration (A1) is almost 2 times higher than in the second configuration (A2). However, it is noticed that the magnetostrictive response in the upper Terfenol-D layer is very low and does not effectively contribute to the strain transmission to the piezoelectric layer in the first configuration (A1). To that end, investigations based on four magnets magnetic circuits are proposed in the following sections.

- Four-magnets magnetic circuit design 1

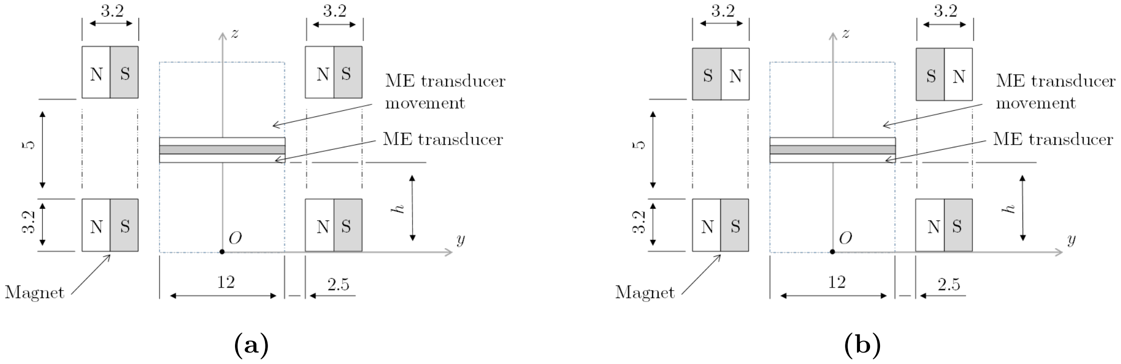

Figure 5.10: Schematic of the proposed finite element investigation with four magnets magnetic circuit design: (a) Configuration B1, and (b) Configuration B2

A second magnetic circuit design based on the use of four magnets is proposed as shown in Figure 5.10. The two upper magnets are placed 5 mm vertically above the two other ones. The ME transducer is placed at h = 4.2 mm so the distance between the upper Ms layer and the two upper magnets is equal to the distance between the lower Ms layer and the two other magnets. A time dependent analysis is performed for one oscillation period of the magnets with an amplitude of 1 mm. Two configurations are studied:
- Configuration B1: The magnetization direction of the four magnets is along the horizontal axis (y-axis) and with the same direction (Figure 5.10 (a)).
- Configuration B2: The magnetization direction of the four magnets is along the horizontal axis (y-axis). The two upper magnets have opposite magnetization direction compared to two lower magnets (Figure 5.10 (b)).

The variations of the average magnetic field density in the upper and the lower Terfenol-D layers for the configuration B1 and 4 are shown respectively in Figure 5.11 (b) and Figure 5.11 (a). The variations of the average deformation in the two Terfenol-D layers and in the piezoelectric layer are presented in Figure 5.11 (d) and Figure 5.11 (c) for the two simulated configuration, respectively. It can be seen that the two Terfenol-D layers undergo similar magnetic field variations, which is caused by the four magnets circuit design. However, the deformations in the three layers in configuration B1, where all magnets have the same direction of magnetization, are very low comparing to configuration B2.

- Four-magnets magnetic circuit design 2

A third magnetic circuit design is proposed as shown in Figure 5.12. The proposed design is similar to the one using two magnets. The main difference is that, the magnets used in the right and the left parts of the magnetic circuit are replaced with two stacked magnets in order to get a concentrated flux gradient. The transducer is placed at h = 3 mm and a time dependent analysis is performed for one oscillation period of the magnets with an amplitude of 1 mm. One configuration is studied:

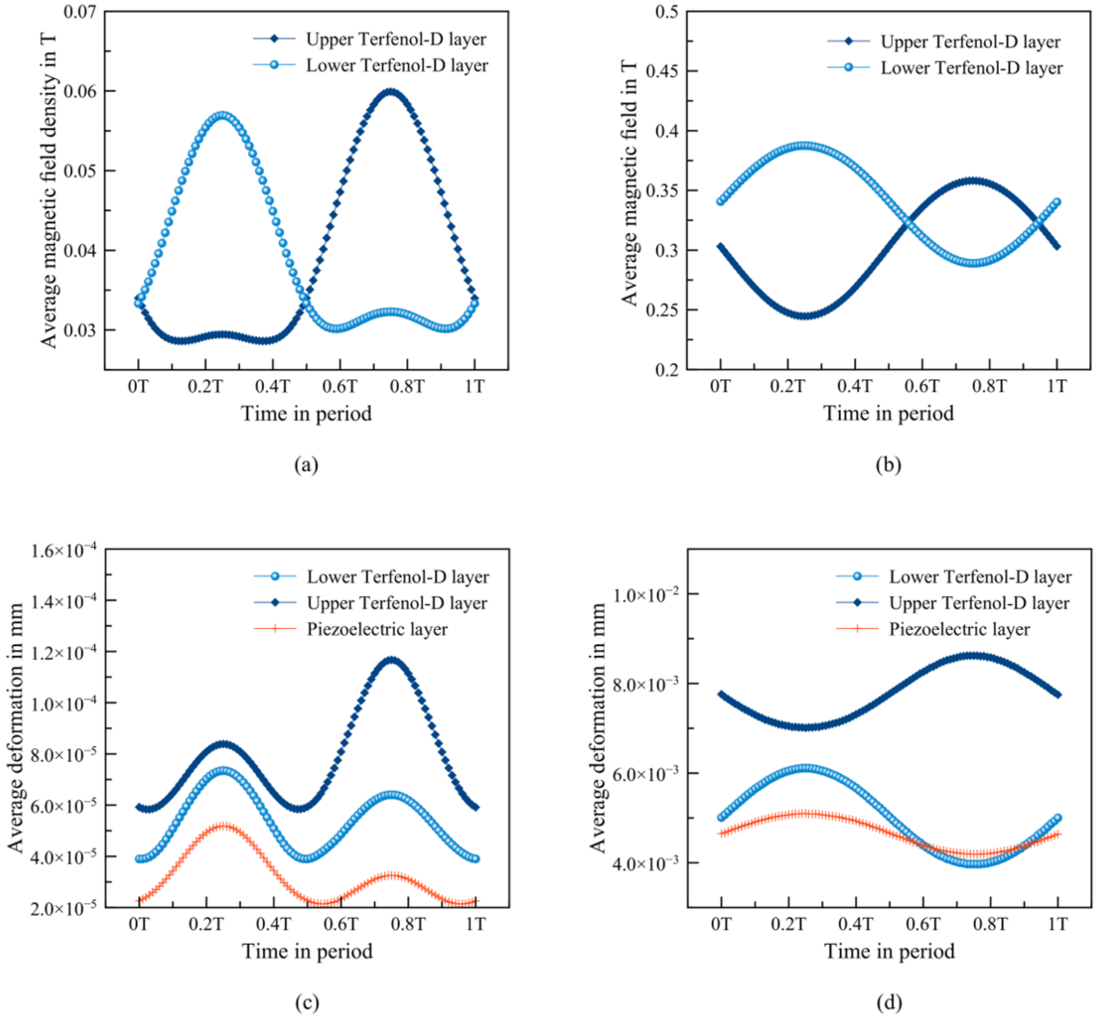

(a) (b)

(c) (d)

Figure 5.11: Variation of the average magnetic field density in (a) Configuration B1, and (b) Configuration B2. Variation of the average deformation in the three layers (c) Configuration B1, and (d) Configuration B2

- Configuration C1: The magnetization direction of the four magnets is along the horizontal axis (y-axis) and with the same direction (Figure 5.12). The variations of the average magnetic field density in the upper and the lower Terfenol-D layers for the configuration C1 are shown in Figure 5.13 (a). The variations of the average deformation in the two Terfenol-D layers and in the piezoelectric layer are presented in Figure 5.13 (b).

In order to select the optimal magnetic circuit design, variations of the deformation in the piezoelectric layers and the induced voltage in the four proposed configurations are presented in Figure 5.14 and Figure 5.15 respectively. It can be seen that the transmitted deformations to the PE layer is higher in configurations A1, B2 and C1 than in configurations A2 and B1 where quasi-null variation of deformation are obtained.

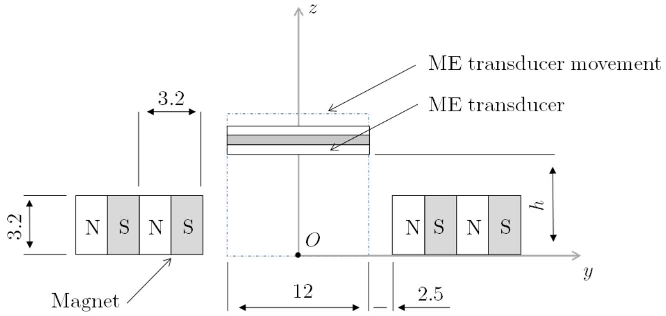

Figure 5.12: Schematic of the proposed finite element investigation with four stacked magnets magnetic circuit design: Configuration C1

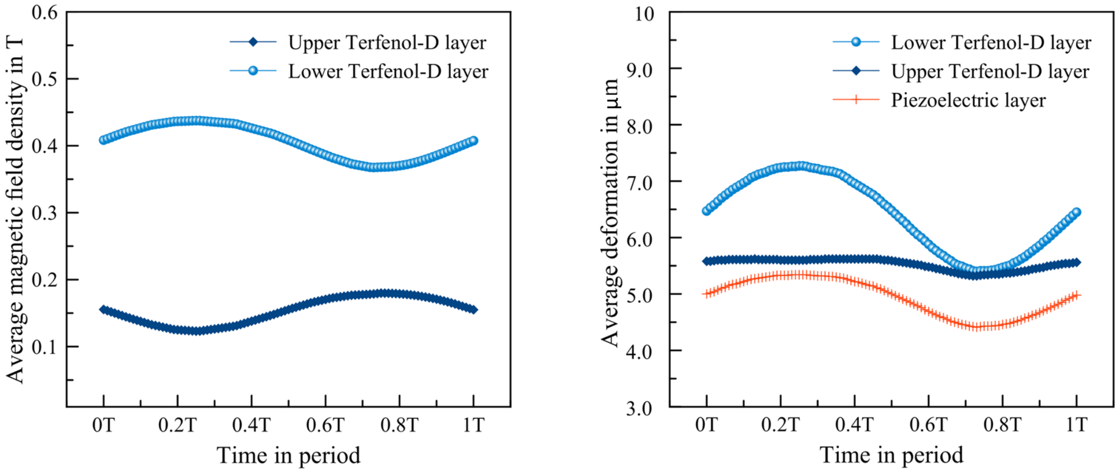

(a) (d)

Figure 5.13: Case of four stacked magnets magnetic circuit design (a) Variation of the average magnetic field density in the three layers, and (b) Variation of the average deformation in the three layers

However, the induced voltage in the piezoelectric layer in configuration C1 is around 25 % and 50 % higher than that in configuration A1 and B2 respectively. In order to analyse these results with relation to the magnetic field acting on the transducer for the 3 proposed magnetic circuit designs, the magnetic flux density distribution for configuration A1, B2 and C1 is investigated (Figure 5.16). As it can be observed in Figure 5.16 (b), the magnetic field created by the four magnets acts similarly on the upper and lower Terfenol-D layers at the initial position of the transducer.
Besides, in the two other configurations (A1 shown in 5.16 (a) and C1 shown in 5.16 (c)), the magnetic field is mainly acting on the lower magnetostrictive layer. However, the strength of the magnetic field created by the magnetic circuit in configuration C1 is significantly higher than in the two other configurations, which may justify the higher voltage output obtained with this configuration as shown in Figure 5.15.

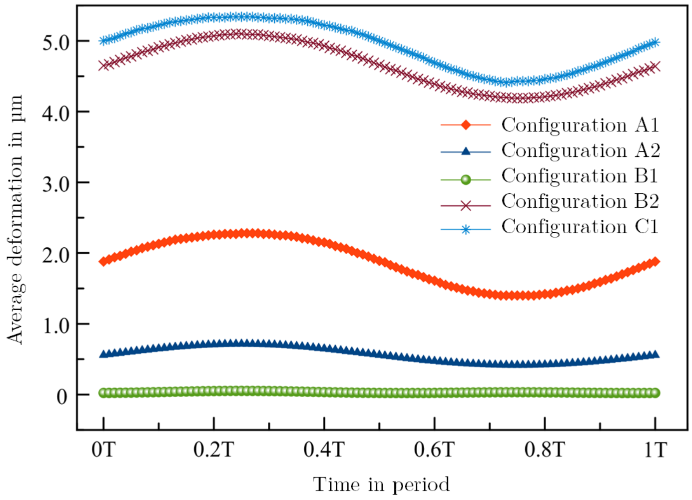

Figure 5.14: Variation of the average deformation in the piezoelectric layer for the five proposed configurations

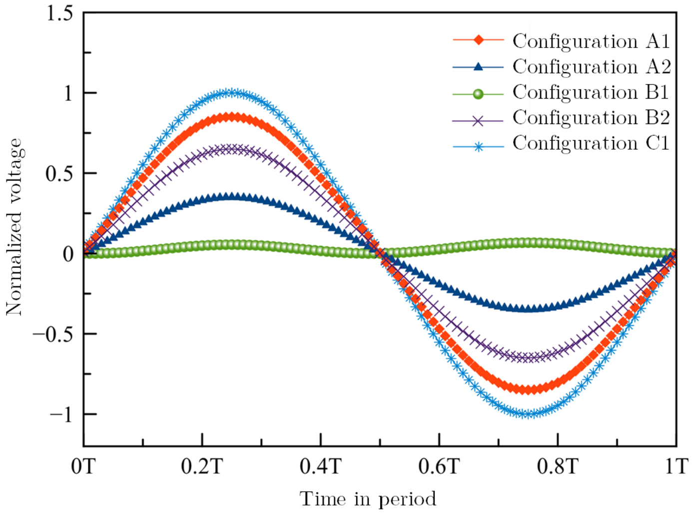

Figure 5.15: Normalized induced voltage from the piezoelectric layer for the five proposed configurations

In the following sections, investigations are performed using the magnetic circuit design proposed in configurations A1, B2, and C1 (See Figure 5.16) in order to study other influencing parameters on the transducer performance.

5.2.2 Optimal initial position of the transducer

The initial position of the transducer along the vertical axis has a great importance for the better use of the magnetic field distribution and has decisive influence on the output power of the ME converter.

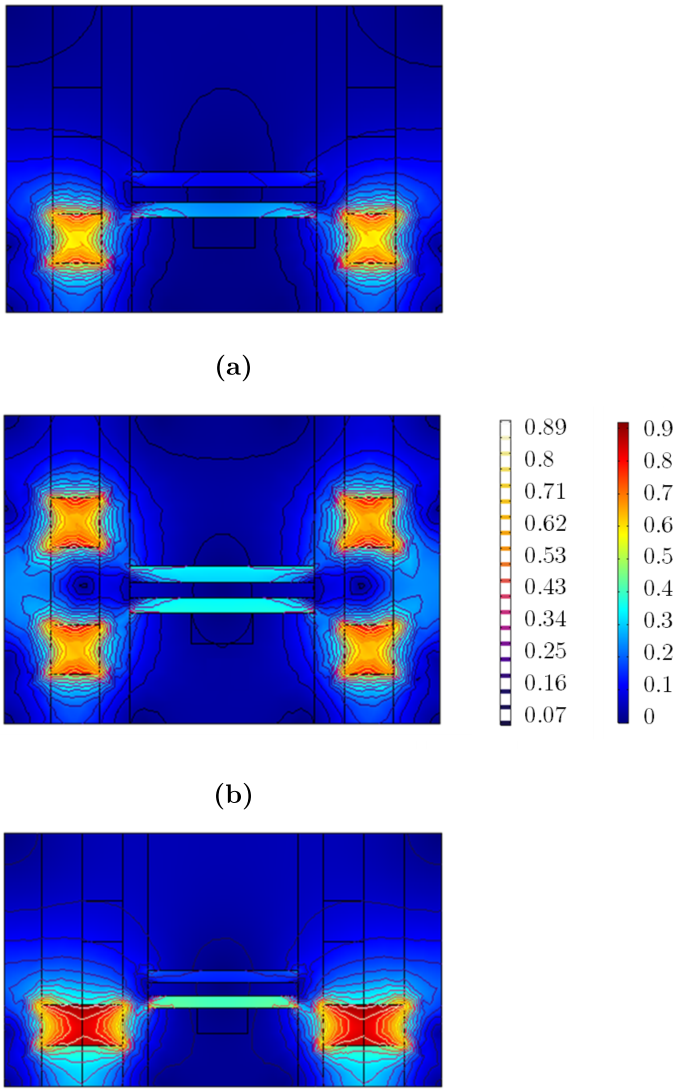

(a)

(b)

(c)

Figure 5.16: Magnetic flux density norm for (a) configuration A1, (b) Configuration B2, and (c) Configuration C1

An optimal position can be selected theoretically by investigating the magnetostrictive response in the Terfenol-D layers or by determining the highest possible transmitted deformation to the inner piezoelectric layer. To that end, a parametric sweep is proposed in function of the initial position of the transducer h. For each h value, a dynamic analysis is performed for one oscillation period of the magnets with an amplitude of 1 mm. Investigations are done for the case of a magnetic circuit as given in configuration C1.

Five vertical positions of the transducer in the air gap of the magnetic circuit are investigated. Figure 5.17 presents the variation of the deformation in the PMNT plate for the different proposed h values for one period of oscillation. It can be found from Figure 5.17 that for $h = 1$ mm $h = 5$ mm, the variation of deformation is almost equal to 0, which results in very low induced voltage. The highest transmitted deformation to the piezoelectric layer is for $h = 3$ mm, i.e, when the transducer is placed exactly in the middle between the upper and the lower magnets along the vertical direction. Therefore, $h = 3$ mm can be used as the optimal initial position to place the transducer. Thus, this position is adopted and is used for FE analyses in the following sections.

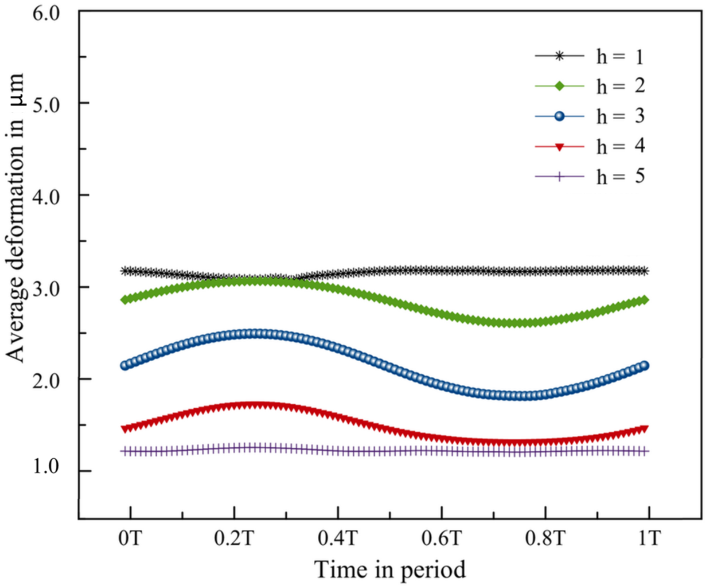

Figure 5.17: Variation of the average deformation in the piezoelectric layer for different positions of the transducer in the air gap of the magnetic circuit

5.2.3 Parameters of the magnetoelectric transducer

Two parameters in the ME laminate composite are investigated, which are principally related to the piezoelectric layer: the direction of polarization and the used material. Investigation are carried out for a magnetic circuit design as given in configuration C1.

5.2.3.1 Direction of polarization of the piezoelectric layer

For the piezoelectric layer, depending on the polarization direction, two modes can be defined: longitudinal mode (L mode) and transversal mode (T mode). In the model under consideration, these modes correspond to y-polarized and z-polarized layer, respectively. A time dependent analysis is performed for each mode to determine the influence of the polarization direction on the transmitted deformations to the PMNT plate and the induced voltages. Figure 5.18 (a) and (b) show the variation of the deformation and the normalized voltage in the piezoelectric layer, respectively, for one period of magnets oscillation with 1 mm amplitude.

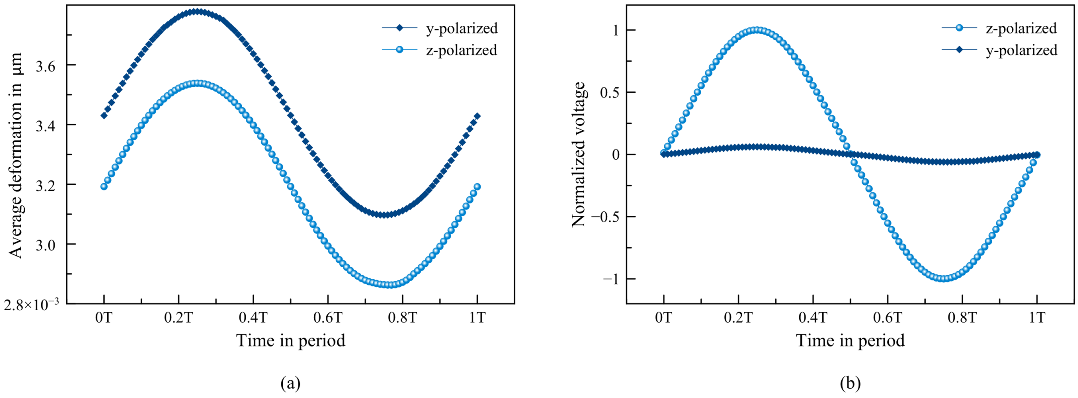

Figure 5.18: (a) Variation of the average deformation in the piezoelectric layer for the two proposed polarization direction. (b) Normalized voltage for the two proposed polarization direction

It can be seen from Figure 5.18 (a) that the deformations in the y-polarized and z-polarized modes have similar variation profiles but with different amplitudes. This can be explained by the fact that the magnetostrictive layers have the same deformation in these two cases and therefore the difference of the measured amplitudes is due to the change of the polarization direction.
However, a big difference in the induced voltage is shown Figure 5.18 (b) for the two polarization directions. In fact, the z-polarized plate generates voltage about 10 times higher than the y-polarized one. Therefore, this direction of polarization is adopted for the design of the ME converter.

5.2.3.2 Piezoelectric materials

The second investigated parameter in the ME transducer is the material of the piezoelectric element. For this purpose, a comparison between Terfenol-D/ PZT/ Terfenol-D and Terfenol-D/ PMNT/ Terfenol-D laminate composites is made. The material properties of PZT used in the simulation are taken from [140] and [141].
Figure 5.19 presents the normalized voltage generated by the PMNT and the PZT plates for one period of oscillation with 1 mm amplitude. It is found that the voltage output when using PMNT is more than twice the voltage output when using PZT. Hence using PMNT as PE material.

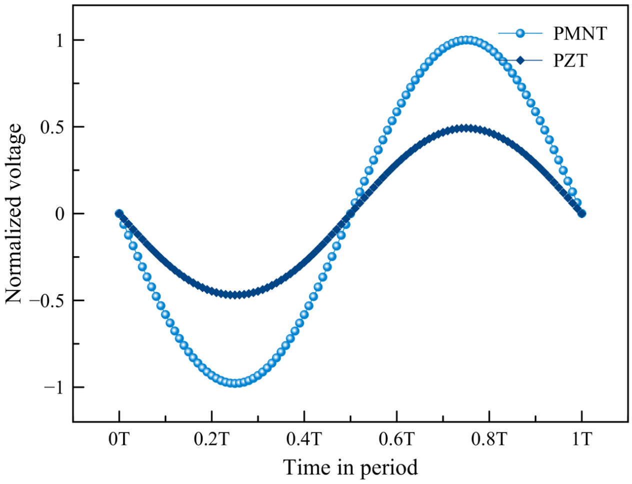

Figure 5.19: Influence of the used piezoelectric material on the output voltage of the transducer

5.3 Harvester design

In this section, the design of the harvester is presented based on different results found by finite element investigations.

5.3.1 Magnetic circuit

In order to evaluate FEM simulation results, three designs of the magnetic circuit are proposed, which are configuration A1, B2 and C1 in the previous sections.
- Configuration A1: Two rectangular magnets having the same magnetization direction along the horizontal axis.
- Configuration B2: Four rectangular magnets having magnetization directions along the horizontal axis. The two upper magnets have opposite magnetization direction compared to two lower magnets.
- Configuration C1: Four rectangular magnets having the same magnetization direction along the horizontal axis. Each two magnets are stacked together along the y axis.

The dimensions of all used rectangular magnets are 6.3 mm × 3.2 mm × 3.2 mm. They are fixed to two supports, which are attached to the housing of converter. Additionally, the position of support relative to the transducer can be adjusted using a simple screw/nut system. All magnets used for the design of the converter are neodymium magnets NdFeB grade N42 KJ Magnetics.

5.3.2 Magnetoelectric transducer

Figure 5.20 presents a schematic of the ME transducer. It consists of one PMNT plate of length 12 mm, width 6 mm and thickness 1 mm bonded to two Terfenol-D plates (Etrema Products, Inc., USA) of length 12 mm, width 6 mm and thickness 1 mm. The

magnetostrictive layers are magnetized in their length direction and the piezoelectric layers are polarized along their thickness direction.
In order to investigate the influence of the epoxy resin used for the fabrication of the ME laminate composite, three scenarios are used for the bonding of the Ms and the PE layers. More details are described in section 6.1.2.3.

5.3.3 Cantilever beam

A brass cantilever beam with 50 mm length and 20 mm width is used. The thickness of the cantilever is determined through finite element analysis (in section 5.4.2.1) in order to select the suitable natural frequency of the converter.

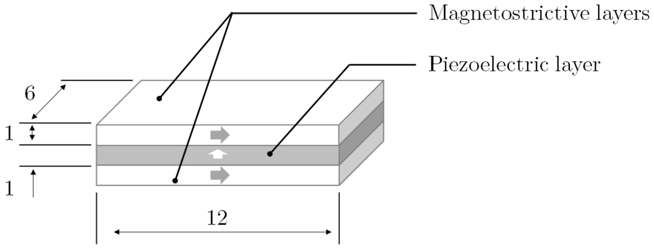

Figure 5.20: Schematic of the magnetostrictive and piezoelectric laminate composite. Magnetostrictive layers are magnetized along their length direction and the piezoelectric layer is polarized along its thickness direction

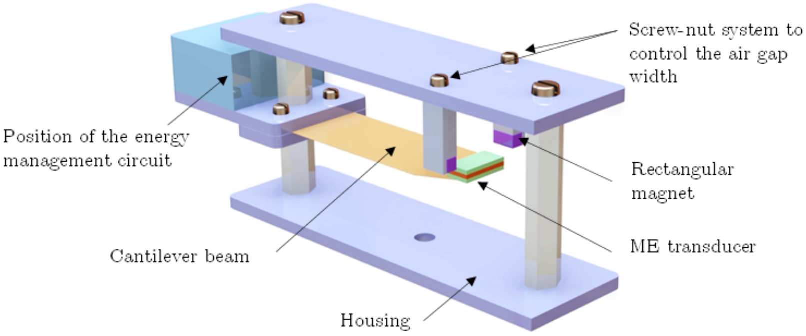

Figure 5.21: Schematic of the proposed magnetoelectric vibration energy harvester

5.3.4 Harvester structure

The harvester consists of an easy mounting structure formed of a cantilever, a single ME transducer, and a magnetic circuit acting on the laminate composite. The structure of the proposed magnetoelectric vibration energy harvester is shown in Figure 5.21. More details are presented in Appendix A.
The process of converting mechanical vibration to electrical energy is based on the magnetoelectric effect as a composite effect of magnetostrictive and piezoelectric layers. The structure can oscillate in the z direction. The principle is that external vibration is transformed first to a change of a magnetic field due to the relative displacement of

the ME transducer attached to the free end of the cantilever and placed in the air gap of the magnetic circuit. The magnetic field change influences the two magnetostrictive layers leading to deformations, which are transmitted directly to the piezoelectric layer leading to generation of electrical power.

5.4 Response analysis of the harvester under harmonic excitation

The aim of this section is to study the electrical response of the proposed design under harmonic excitation. The idea is to analyse the governing equation of the converter using Lindstedt-Poincaré method, and then to predict the power outcome of the transducer based on the ME equivalent circuit.

5.4.1 Governing equation

The proposed converter can be modelled as a one degree of freedom (1 DoF) mechanical spring-mass-damper model as shown in Figure 5.22. m presents the mass of the transducer and the cantilever, and $u(t)$ denotes the vertical displacement of the vibration source. Mechanical loses are modelled by the viscous damping force F_c having a damping force factor c. F_M presents the interaction force between the magnetic circuit and the two ME transducers. The governing equation of the 1 DoF converter can be written according to Newton's second law as given in Equation 5.10:

$$F_c + F_k + F_M + p = ma_c \tag{5.10}$$

where p denotes the excitation force, and a_c is the acceleration vector.
Due the non-linear distribution of the magnetic field created by the magnets, F_M is a non-linear function of the displacement z. It can be expressed by Equation 5.11:

$$F_M(z) = \sum_{i=0}^{n} \alpha_i z^i \tag{5.11}$$

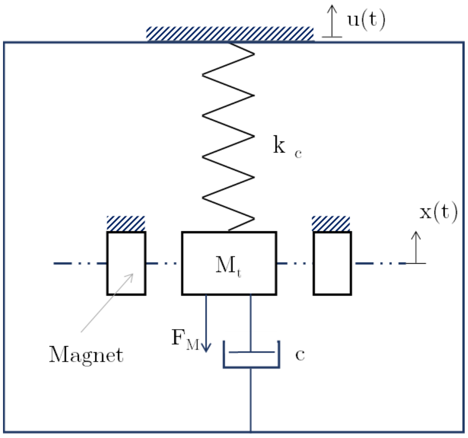

Figure 5.22: Equivalent model of the vibration converter

Therefore, in the case of harmonic excitation, the governing dynamic equation of motion of the converter is given by Equation 5.12.

$$m\ddot{z} + c\dot{z} + k_c z + \sum_{i=0}^{n} \alpha_i z^i = mP_0 sin(\bar{\omega} + \phi) \tag{5.12}$$

where P_0 is the amplitude of the external vibration acceleration, $\bar{\omega}$ is the angular frequency and ϕ represents the phase angle. For small amplitude vibration, n and p are not greater than 3 (Which is be confirmed by finite element analysis in section 5.4.2.3), so Equation 5.12 can be rewritten as given by Equation 5.13.

$$m\ddot{z} + c\dot{z} + \alpha_3 z^3 + \alpha_2 z^2 + (k_c + \alpha_1)z = mP_0 sin(\bar{\omega} + \phi) \tag{5.13}$$

Introducing the two parameters $\omega = \sqrt{(\alpha_1 + k_c)/m}$ and $\xi = c/2\sqrt{(\alpha_1 + k_c)/m}$ in Equation 5.13, Equation 5.14 is obtained.

$$\ddot{z} + 2\xi\omega\dot{z} + \omega^2 z + \frac{1}{m}[\alpha_3 z^3 + \alpha_2 z^2] = P_0 sin(\bar{\omega}t + \phi) \tag{5.14}$$

or in an equivalent form as presented in Equation 5.15:

$$\ddot{z} + 2\tau\psi\omega\dot{z} + \omega^2 z + \frac{\tau\omega^2}{m}[\alpha_3 z^3 + \alpha_2 z^2] = \tau P_0 \omega^2 sin(\bar{\omega}t + \phi) \tag{5.15}$$

where $\tau = 1/\omega^2$ and $\psi = \xi\omega^2$. The differential Equation 5.15 is solved by the Lindstedt-Poincaré method [142] [143] and leads to Equation 5.16 as a first approximate solution (see Appendix B for more details):

$$z(t) = \gamma cos(\bar{\omega}t) + \frac{\alpha_2\gamma^2}{6m\omega} cos(2\bar{\omega}t) + \frac{\alpha_3\gamma^3}{32m\omega} cos(3\bar{\omega}t) \tag{5.16}$$

where γ is found as a solution of Equation 5.17.

$$(2\psi\gamma)^2 + [\frac{\alpha_3 + \gamma^3}{4m}]^2 = P_0 \tag{5.17}$$

5.4.2 Structure parameters

The aim of this section is to determine necessary parameters mentioned in the analytical model in the previous section (Section 5.4.2.1). The analysis of the interaction force between the magnets and the ME transducer is performed for the three proposed configurations of the magnetic circuit.

5.4.2.1 Resonance frequency

The structure of the cantilever beam based converter is shown in Figure 5.23. If we consider a cantilever beam having a rectangular cross section and fixed at one end with a concentrate mass on the other end, the natural angular frequency of the system, ω_c, can be determined using the approximate formula given in Equation 5.18 ([144]).

$$\omega_c = \sqrt{\frac{k_c}{M_t + 0.23 m_c}} \tag{5.18}$$

where k_c is the stiffness of the cantilever beam. M_t and m_c are respectively the mass of the transducer and the cantilever beam (see Figure 5.23).
It has to be noted that the existence of the magnetic force resulting from the interaction between the magnetic circuit and the ME transducer creates an additional non-linear stiffness within the structure. In that case, the resonance frequency of the structure can be determined as a function of the beam stiffness and the stiffness associated with the magnetic force. In the following, the influence of magnetic force is not taken into consideration in the calculation of the resonance frequency in this section. In this case, the theoretical natural frequency of the structure is the same for the three configurations of the magnetic circuit design.
The bending stiffness can be determined using Equation 5.19.

$$k_c = \frac{3E_cI_c}{l_c^3} \tag{5.19}$$

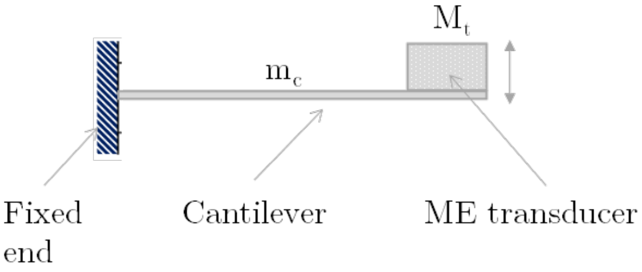

Figure 5.23: Schematic of the converter structure

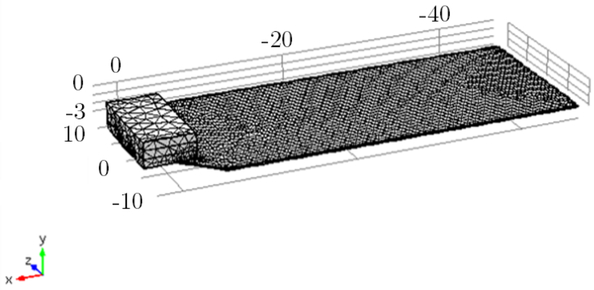

Figure 5.24: Mesh of the simulation model for the modal frequency analysis

where E_c is the elastic modulus of the beam material, l_c is the length of the cantilever and I_c is the second moment of area about the neutral axis and is given by Equation 5.20 as a function of the width b_c and the thickness h_c of the beam.

$$I_c = \frac{b_c h_c^3}{12} \tag{5.20}$$

For instance, based on the approximate formula (Equation 5.18), the estimated theoretical resonance frequency of the converter with 0.2 mm thickness is about 25 Hz.
In order to select the suitable thickness of the cantilever to obtain the first resonance frequency of the beam in the range of 20 Hz to 50 Hz (Frequency range for most of environmental vibration [145]), a modal frequency analysis is performed with a parametric sweep for the thickness of the beam.
Figure 5.24 shows the mesh for the model used for the modal analysis. Another advantage of the simulation model is that it takes into consideration the two chamfers on the beam at the free end. The parametric sweep is performed for 3 thicknesses, which are 0.1 mm, 0.2 mm and 0.3 mm.
Results are presented in Table 5.4. As it can be seen, for the first mode, the natural frequency of the converter is 8.54 Hz, 23.36 Hz and 41.61 Hz respectively for 0.1 mm, 0.2 mm and 0.3 mm thicknesses. Therefore, the selected thickness of the beam is 0.2 mm.
Figure 5.25 shows the first six modes obtained in the modal analysis for the structure with 0.2 mm thickness. It can be seen that the mode shape at the first, third, fourth and sixth order is flexural along the length direction (x axis); the mode shape at the second and fifth order is flexural along the width direction (z axis) combined with torsion.

5.4.2.2 Non-linear magnetic force

The magnetic force and the magnetic stiffness resulting from the interaction between the magnetic circuit and the ME transducer are investigated using finite element analysis for the three proposed magnetic circuit configurations. The position of the magnetoelectric transducers in the air gap of the magnetic circuit introduces additional

Table 5.4: Modal analysis results

		Thickness in mm		
		0.1	0.2	0.3
Eigenfrequency in Hz	First mode	8.54	23.36	41.61
	Second mode	75.57	190.41	319.69
	Third mode	113.12	241.08	374.85
	Fourth mode	323.04	700.47	1101
	Fifth mode	368.46	750.03	1160.1
	Sixth mode	659.99	1372.8	2155.7

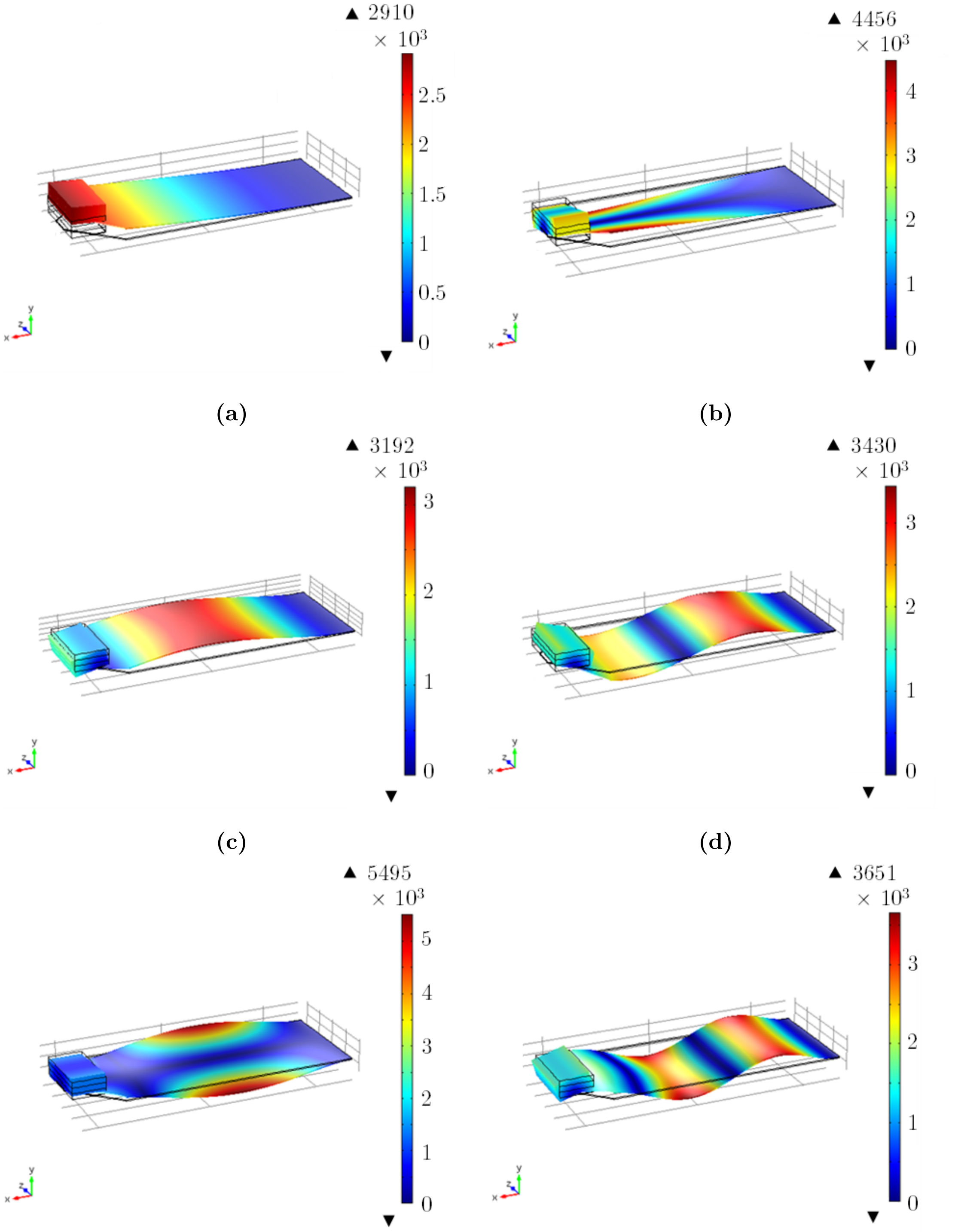

(a) **(b)**

(c) **(d)**

(e) **(f)**

Figure 5.25: Modal analysis results. The first six modes for a 0.2 mm beam thickness (a) 23.36 Hz, (b) 190.41 Hz, (c) 241.08 Hz, (d) 700.47 Hz, (e) 750.03 Hz, and (f) 1372.8 Hz

stiffness K_{mc}, which affects the resonance frequency of the device as it is confirmed experimentally in the next chapter. K_{mc} can be given in Equation 5.21.

$$K_{mc} = |\frac{\partial F_M(z)}{\partial z}| \tag{5.21}$$

The simulation model consists of the magnetic circuit, the transducer and an air domain. A parametric sweep for the position of ME transducer along the z axis is performed. The initial position of the magnets along z axis is chosen so that the lower surface of the transducer and the magnets are in the same x-y plane as shown in Figure 5.26 for configuration A1. The magnetic flux density distribution for the three proposed configurations is presented in Figure 5.27. As it can be seen, the magnetic field in the case of configuration C1 (Figure 5.27 (c)) can reach higher magnetic flux density amplitudes up to about 1.3 T due to the use of two stacked magnets in each side of the plate.

The magnetic forces for the three configurations for different positions of the ME transducer are presented in Figure 5.28 (a), (b) and (c) respectively. It can be observed that the highest variation of the magnetic force in function of the position of the ME transducer is obtained for configuration C1 (Figure 5.28 (c)).

5.4.2.3 Induced magnetic flux density

On the basis of the same simulation model, the induced magnetic flux density of the ME transducer is determined. Since the magnetic field in the air gap is non-uniform, the lower and the upper Terfenol-D layers undergo different magnetic field variations and induced magnetic field density, in one layer, is not identically distributed.

Both x and z components of the magnetic flux density are ignored in this analysis due to the position of the transducer in the air gap and to the magnetization direction of the two Terfenol-D layers, which is parallel to the y axis.

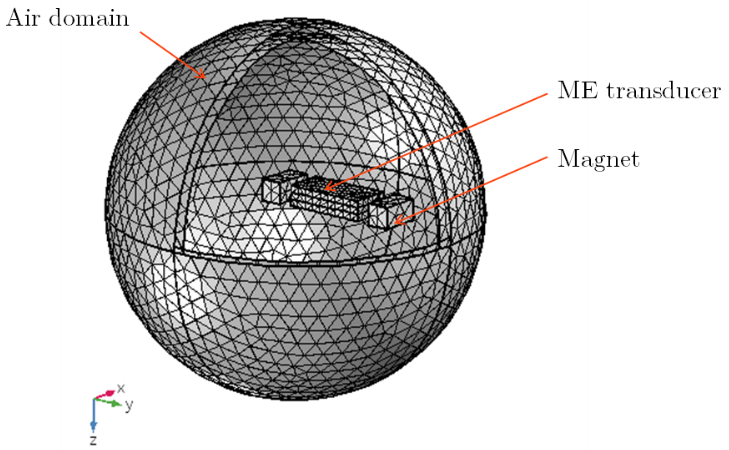

Figure 5.26: Mesh of the simulation model used for the investigation of the magnetic force

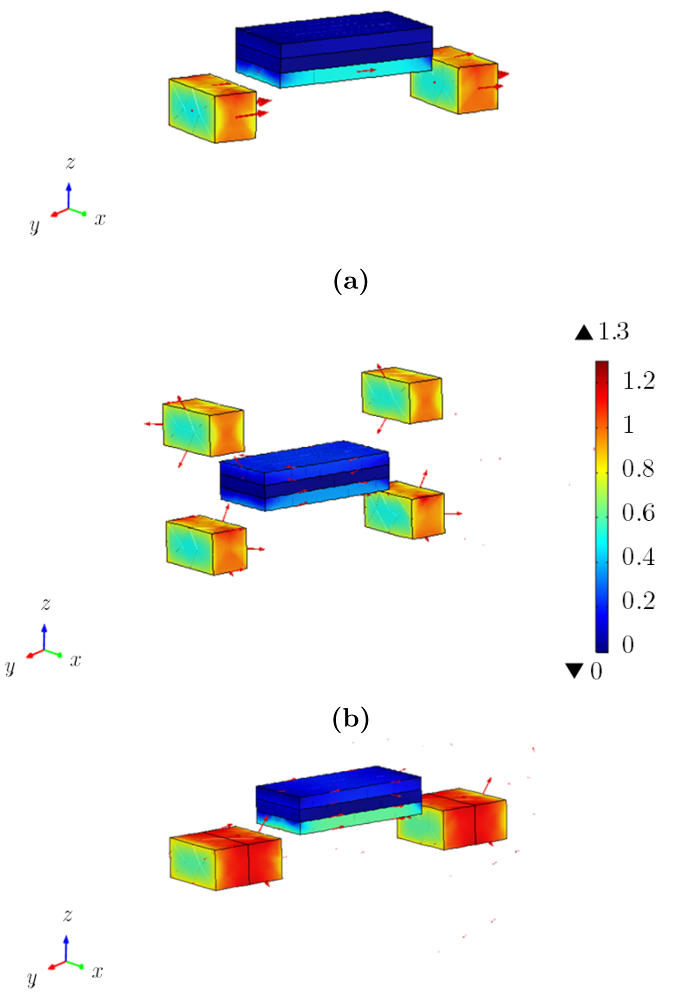

(c)

Figure 5.27: Magnetic flux density distribution for (a) Configuration A1, (b) Configuration B2, and (c) Configuration C1. Red arrow lines refer to the spatial magnetic flux density

The magnetic flux densities are taken as absolute values because the Terfenol-D layers are able to elongate both in the forward and reverse magnetic field.

The aim is to get high magnetic field variation for low displacement of the transducer. The prediction of the induced B in the upper and in the lower Ms layers in addition to the average value, $|B_t|$, $|B_l|$ and $|B_u|$ respectively, for different positions of the transducer along the z axis is given in Figure 5.29 (a), (b), and (c) for the three configurations, respectively.

Results demonstrate that the maximum variation of the average magnetic flux density $|B_u|$ is about 0.45 T, 0.41 T, and 0.57 T when the magnetic circuit is formed of 2 magnets (configuration A1), 4 magnets (configuration B2) and 4 stacked magnets (configuration C1) respectively.

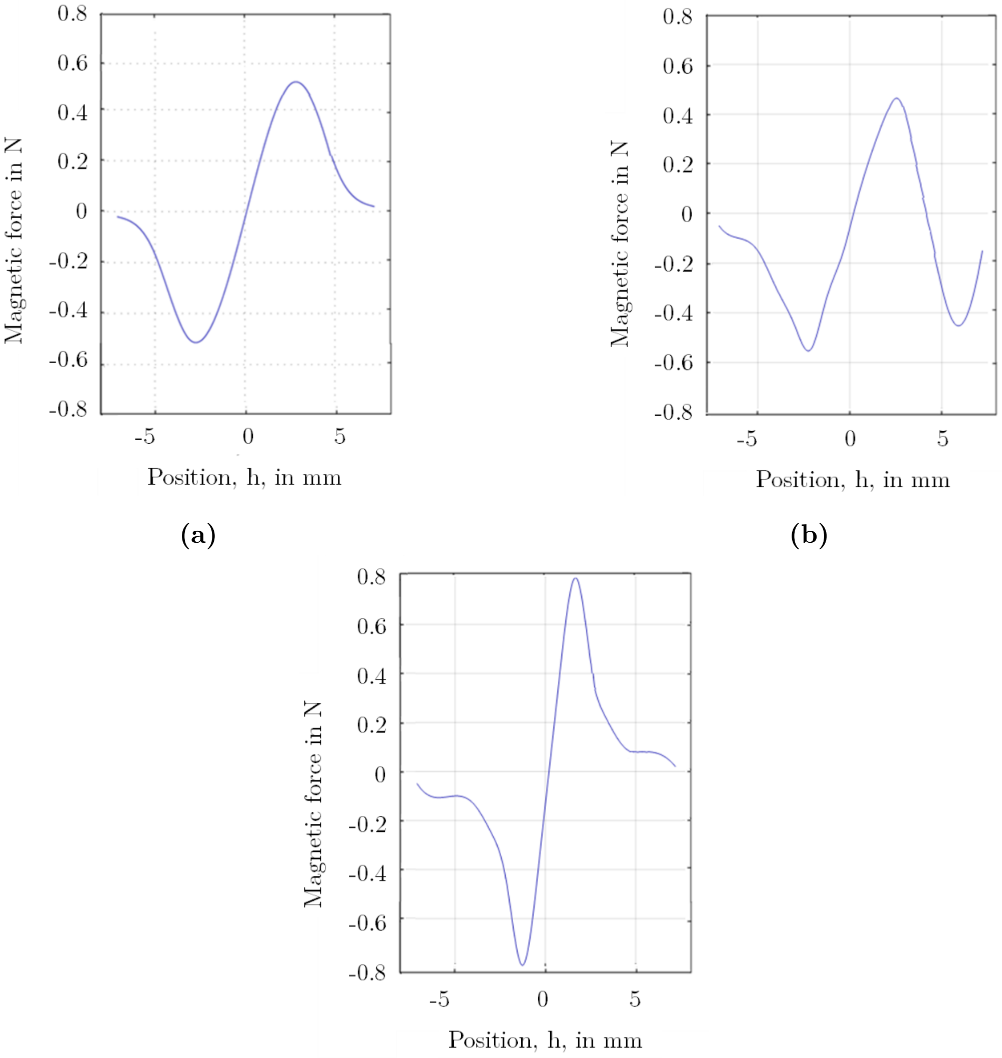

(a)

(b)

(c)

Figure 5.28: Magnetic force resulting from the interaction between the magnetic circuit and the transducer for (a) Configuration A1, (b) Configuration B2, and (c) Configuration C1

The average induced magnetic flux density in both the lower and the upper magnetostrictive layers can be given by Equation 5.22.

$$B_u(z) = \sum_{i=0}^{r} b_{ui} z^i \tag{5.22}$$

Using the method of curve fitting in Figure 5.29, the coefficients b_{ui} shown in Equation 5.22 are:

- Configuration A1:
  b_{u0}=0.26 T, b_{u1}=-0.067 T/m, b_{u1}=-0.0068 T/m^2, b_{u1}=0.0028 T/m^3.

- Configuration B2:
  b_{u0}=0.32 T, b_{u1}=-0.038 T/m, b_{u1}=-0.017 T/m^2, b_{u1}=0.0028 T/m^3.

- Configuration C1:
  b_{u0}=0.44 T, b_{u1}=-0.014 T/m, b_{u1}=-0.023 T/m^2, b_{u1}=0.0025 T/m^3.

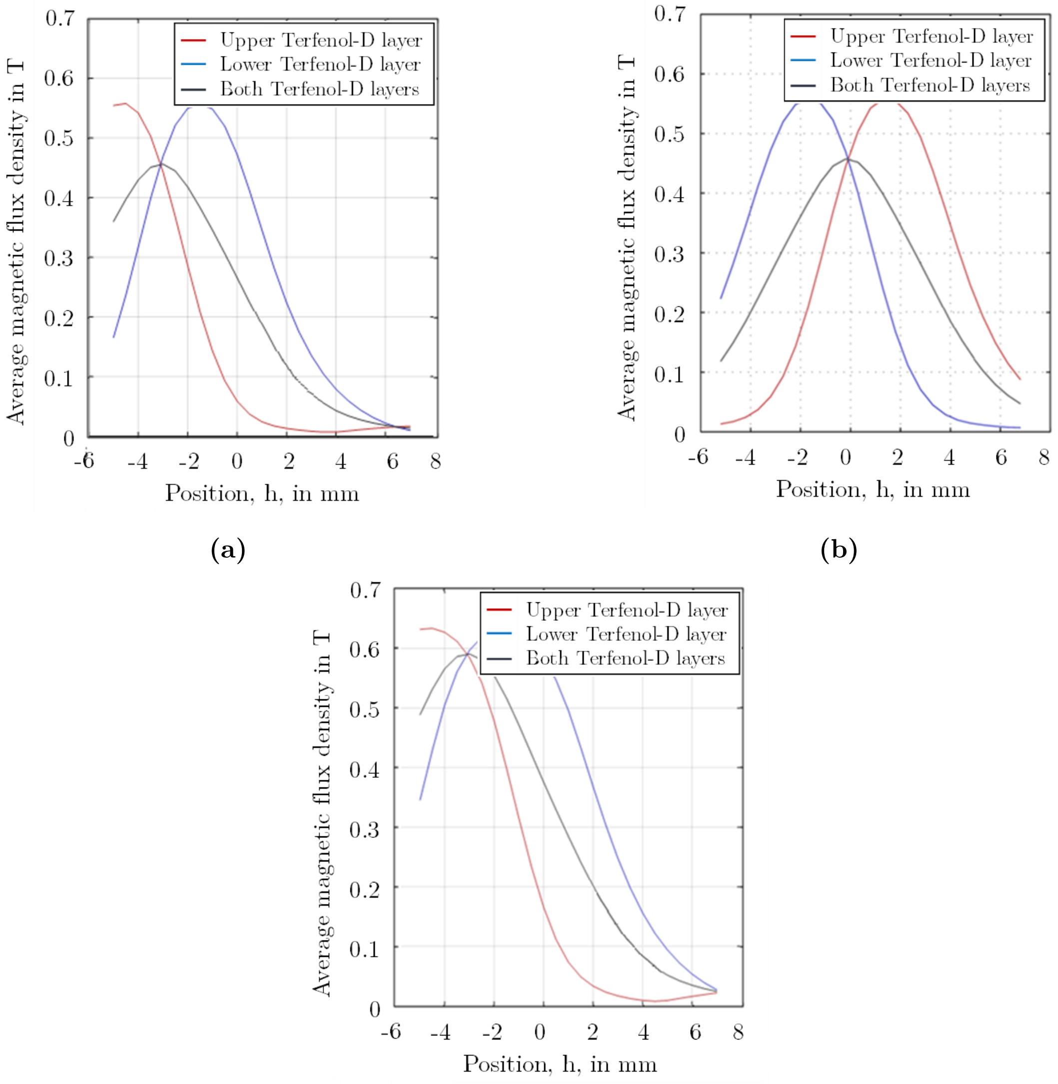

(a)

(b)

(c)

Figure 5.29: Magnetic flux density versus position of the transducer in the magnetic circuit for (a) Configuration A1, (b) Configuration B2, and (c) Configuration C1

Similarly, the interaction force between the magnetic circuit and the ME transducer F_M can be deduced based on results shown in Figure 5.28 as given in Equation 5.23.

$$F_M(z) = \sum_{i=0}^{n} \alpha_i z^i \tag{5.23}$$

where

- Configuration A1:
  α_0=1.15 N, α_1=-1.38 N/m, α_2=-0.352 N/m^2, α_3=-0.026 N/m^3.

- Configuration B2:
  α_0=1.9 N, α_1=-0.94 N/m, α_2=0.16 N/m^2, α_3=0.0093 N/m^3.

- Configuration C1:
  α_0=-1.5 N, α_1= 1.9 N/m, α_2=-0.55 N/m^2, α_3=-0.04 N/m^3.

5.4.3 Theoretical power outcome

In this section, the harvester power outcome is analysed based on the ME equivalent circuit. In the analysis we use an approach, which is similar to [83]. The resonance frequency of the harvester working on the L-T mode is around 24 Hz (without considering the effect of the non-linear magnetic force, which is different for the three configurations). In this case (under 1000 Hz), the magnetoelectric equivalent circuit of the transducer under free-free boundary conditions is shown in Figure 5.30 [146]. Then, the open circuit voltage can be written as given in Equation 5.24.

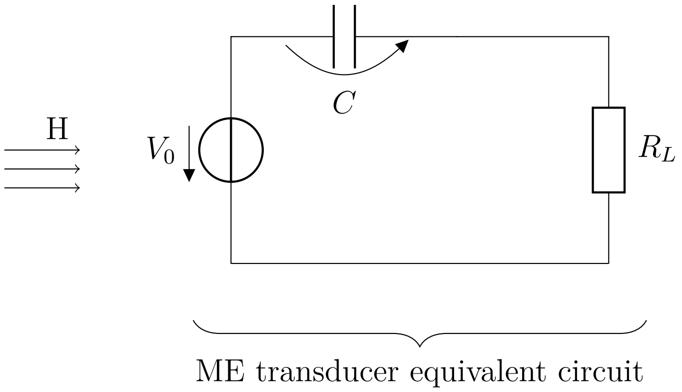

Figure 5.30: Magnetoelectric transducer equivalent circuit under free-free conditions

$$V_0 = \frac{\lambda_f \alpha_{ME} B_{rms}}{\mu_0} \tag{5.24}$$

where μ_0 is the vacuum permeability ($\mu_0 = 4\ \pi\ 10^{-7}$ N/A^2), α_{ME} is the theoretical ME voltage coefficient of the laminate composite, λ_f is the adjustment factor between

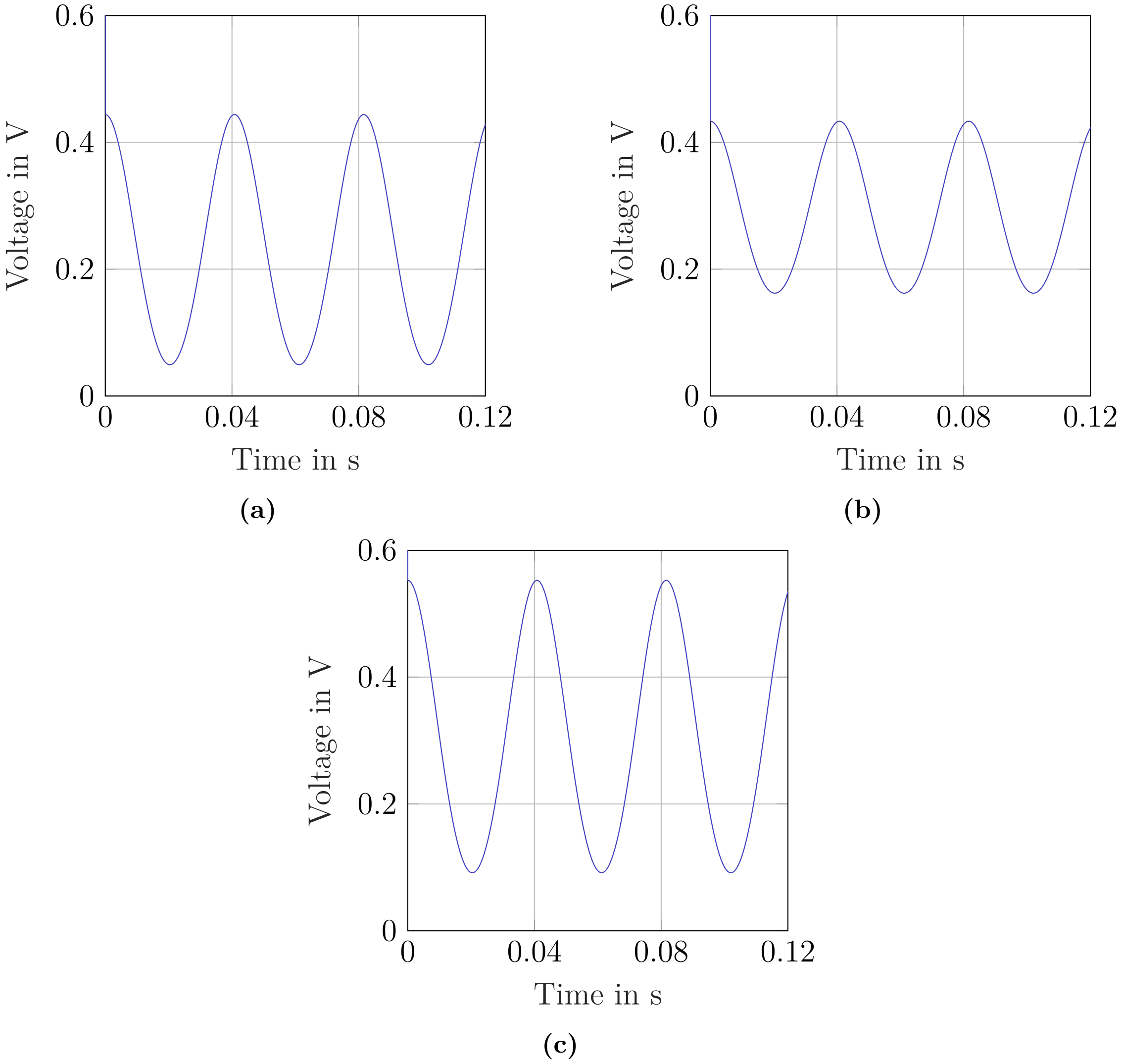

Figure 5.31: Theoretical magnetic flux density versus time at resonance for (a) Configuration A1, (b) Configuration B2, and (c) Configuration C1

the theoretical and the experimental ME voltage coefficient.
B_{rms} represents the root mean square of the alternating magnetic flux density. In fact, the magnetic flux density B can be decomposed in two terms, static and alternating term. The alternating magnetic flux density B_a can be given as an arbitrary function η(z), then B_{rms} can be determined as given in Equation 5.25. Figures 5.31 (a), (b), and (c) show the theoretical magnetic flux density versus time and the open circuit voltage versus time at resonance for the three configurations. The amplitudes of the open circuit voltages are calculated based on Equation 5.24 where $\lambda_f \alpha_{ME} = 20$ mV/Oe and B_{rms} is 0.22 T, 0.19 T, and 0.23 T for configuration A1, B2, and C1, respectively.

$$B_{rms} = \frac{1}{T}\int_a^b B_a(t)dt = \frac{1}{T}\int_a^b \eta(z(t))dt \tag{5.25}$$

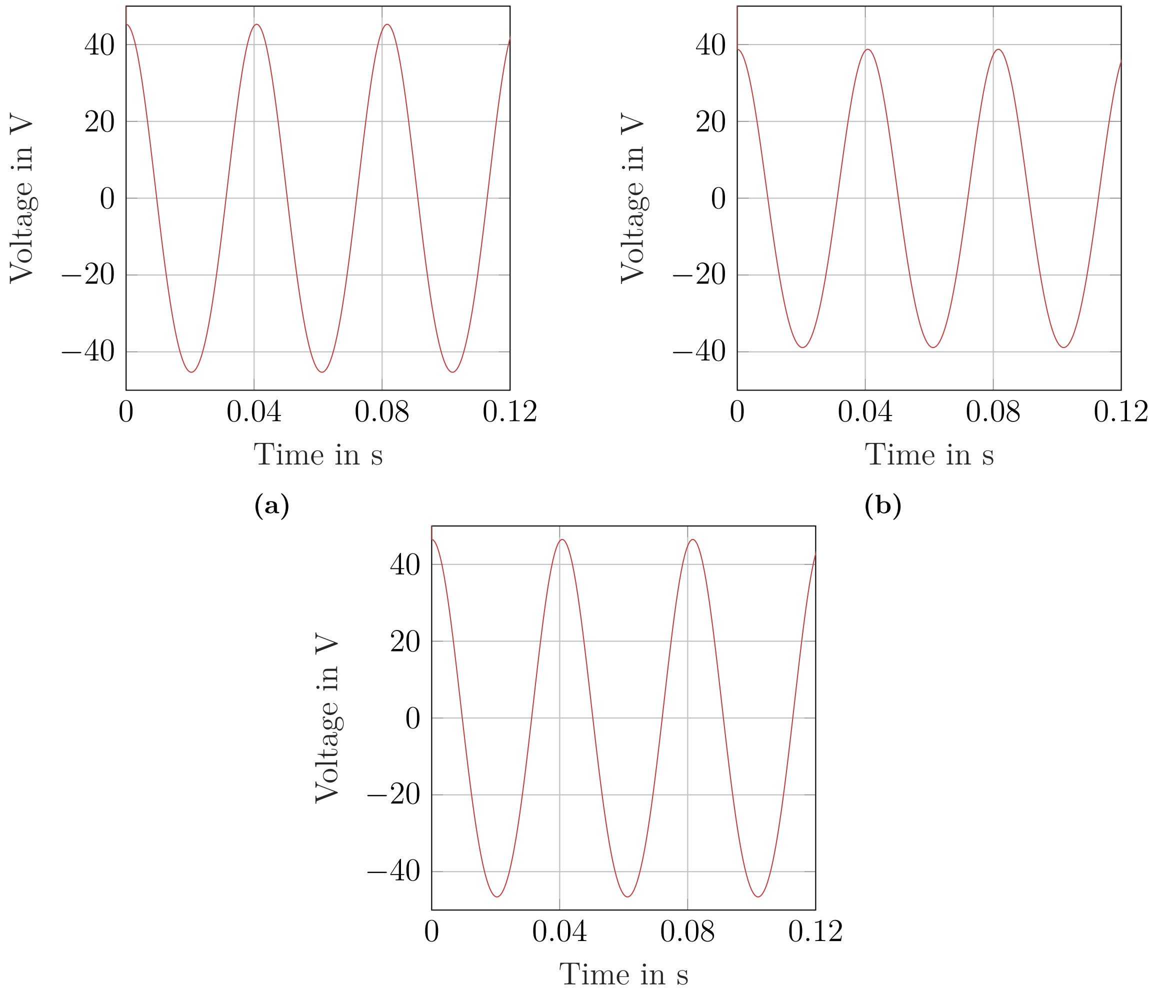

(a) (b) (c)

Figure 5.32: Theoretical open circuit voltage versus time at resonance for (a) Configuration A1, (b) Configuration B2, and (c) Configuration C1

Furthermore, the output voltage V and the output power P in function of the load resistance R_L can be written as follows (Equation 5.26):

$$V = |\frac{\lambda_f \alpha_{ME} B_{rms} R_L}{\mu_0[(1/j\bar{\omega}C) + R_L]}| = \frac{\lambda_f \alpha_{ME} B_{rms} R_L \bar{\omega} C}{\mu_0 \sqrt{(1 + (\bar{\omega} C R_L)^2}} \tag{5.26}$$

In Equation 5.26, C refers to the capacitance of the whole transducer, i.e., the two Ms layers and the PE layer.
The maximum power output can be obtained at the optimal load resistance as given by Equation 5.27.

$$P_{max} = P(R_L = \frac{1}{\bar{\omega}C}) = \frac{(\lambda_f \alpha_{ME} B_{rms})^2 \bar{\omega} C}{2\mu_0^2} \tag{5.27}$$

The output voltages of the transducer for the three proposed configurations versus load resistances at resonance is given in Figure 5.33. As it can be seen, the converter, which uses the 4 stacked magnets (configuration C1), can generate higher output voltage than the converter with the two other configurations. For instance, at 1 MΩ load resistance, the voltage generated by the converter with 4 stacked magnets is 1 V and 7 V higher of that generated by the converter with configuration A1 and configuration C1, respectively.

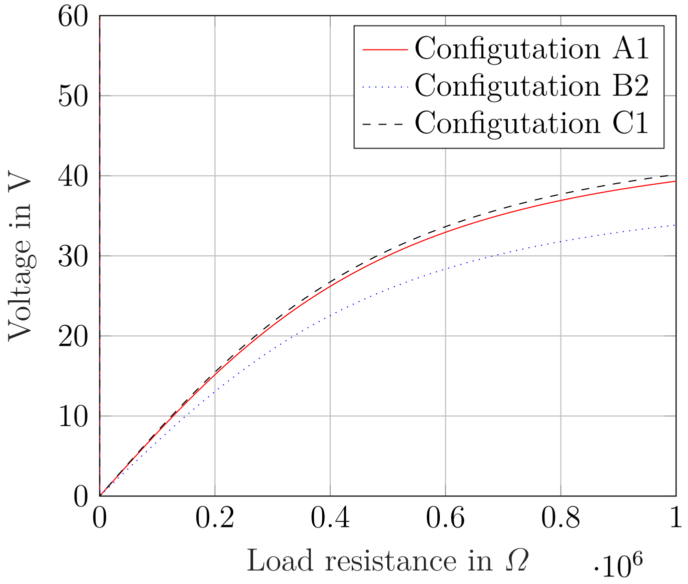

Figure 5.33: Output voltage versus load resistance at resonance

5.5 Conclusion

In this section, the design of the vibration energy converter is presented and analysed. An improved finite element analyses is used to determine the suitable design and different structure parameters. The corresponding system is analysed analytically, and the governing equation is solved with the Lindstedt-Poincaré method taking into account the addition magnetic stiffness created by the magnetic forces between the ME transducer and the magnetic circuit. The non-linear magnetic forces, magnetic field distribution and electrical output performances of the harvester are studied in detail by the ME equivalent circuit method.

CHAPTER 6

Experimental investigations

In this chapter, experiments are performed on the proposed magnetoelectric converter under both harmonic and measured vibration profiles reproduced by an artificial vibration source.
The converter is tested with three different designs of the magnetic circuit which are presented in the previous chapter in section 5.2.1.2 in order to evaluate simulation results. Three ME transducers with three different bonding adhesives are proposed using conductive epoxy resin, epoxy mixed with 1 wt.% and 2 wt.% concentrations of multi-walled carbon nanotubes, respectively, in order to investigate the effect of the used bonding adhesive. Here, besides the power output investigation, the resonance frequency and the bandwidth of the converter under different air gap widths are studied.

6.1 Prototype design and experimental setup

6.1.1 Experimental setup

The set-up used in experimental investigations is shown in Figure 6.1. It consists of an electro-dynamical vibration shaker (VebRobotron Type 11077) driven by a Labview routine through a closed loop controller. A measurement card NI PCI 6259 is used as a signal source. Meanwhile a triangulation sensor OptoNCDT ILD 1800 measures the time-varying displacement of the converter. An amplifier is employed to control the shaker and to adjust the output current of the measurement card. Additionally, two power supplied are used for the laser sensor and the shaker controller. The output voltage is measured and acquired using an oscilloscope (LeCroyWaveRunner 6050A). During the experimental investigations, the housing of the converter is screwed on the top of the shaker as shown in Figure 6.1(b).
So far, the developed LabVIEW code is implemented to fully control the measurement card [147]. It comprises the following parts:

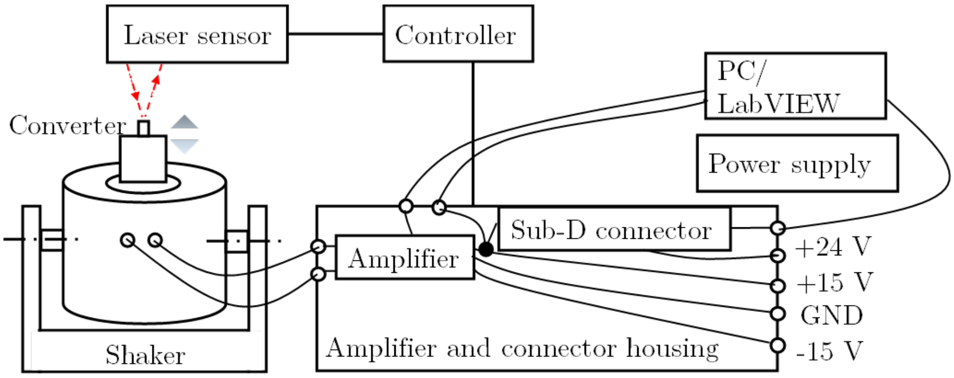

(a)

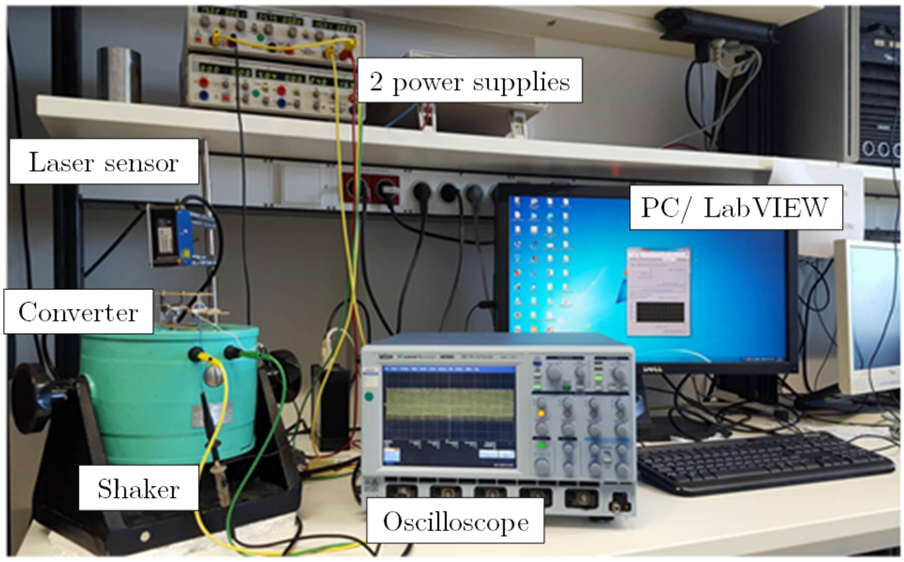

(b)

Figure 6.1: Experimental setup (a) Schematic, and (b) Photograph

- Calibration

  Figure 6.2 shows the tab for the calibration of the experimental set-up. This step is mandatory to control the shaker and all investigated excitations have to be in the frequency range of the calibration.
  In the proposed experimental investigations, the system is calibrated for a frequency range from 1 to 80 Hz using 3 calibration steps of 10 frequencies by a linear sweep with a calibration duration of 10s.

- Excitation with sinusoidal signals

  Measurements with the shaker can be done with the LabVIEW program with sinusoidal signals. Two excitation types are possible which are single frequency or sweep. For both cases, the shaker amplitude or acceleration have to be fixed. The tab for determining the excitation signals is shown in Figure 6.3.

- Excitation with measured vibration profiles

  Measured vibration can be reproduced with the shaker with the same amplitudes and frequency behaviour. Vibration profiles have to be saved as an audio file (.wav). The data is digitally filtered and frequencies. Additionally, the amplitude of the signal can be controlled by varying the scale factor which is defined in the user interface as presented in Figure 6.4.

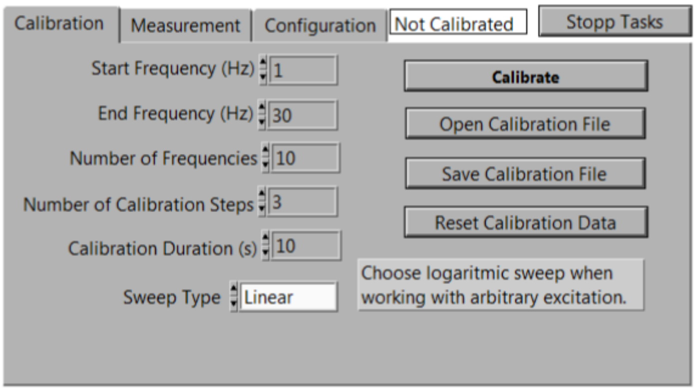

Start Frequency (Hz) 1
End Frequency (Hz) 30
Number of Frequencies 10
Number of Calibration Steps 3
Calibration Duration (s) 10
Sweep Type Linear
Choose logaritmic sweep when working with arbitrary excitation.

Figure 6.2: Calibration tab

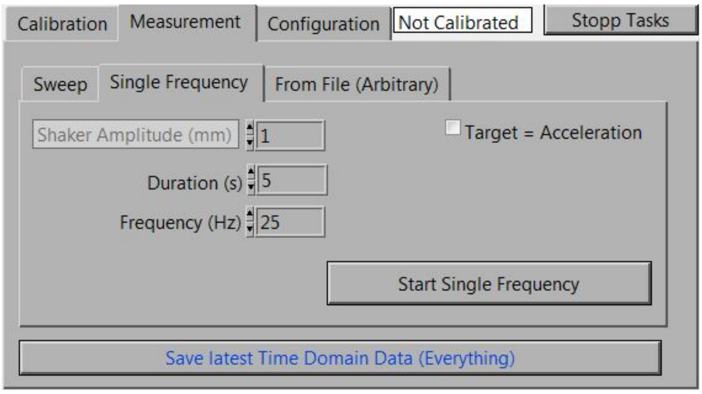

Shaker Amplitude (mm) 1
☐ Target = Acceleration
Duration (s) 5
Frequency (Hz) 25

Figure 6.3: Sinusoidal excitation tab

6.1.2 Prototype fabrication

The ME converter prototype consists of an easy mounting structure. The cantilever beam is made of brass and is 50 mm × 20 mm × 0.2 mm in size. The rectangular magnets are 6.3 mm width, 3.2 mm height and 3.2 mm thickness. The remnant flux density and relative permeability of the magnets are 1.32 T and 1.09, respectively.
The ME transducer is formed of a PMNT plate bonded to two Terfenol-D layers. Both the dimensions of the PMNT and the Terfenol-D layers are 12 mm × 6 mm × 1 mm, being 12 mm in the longitudinal direction and 1 mm thickness. Terfenol-D is produced by ETREMA Products, Inc. USA. PMNT is produced by Shanghai Institute of Ceramics Chinese Academy of Sciences.

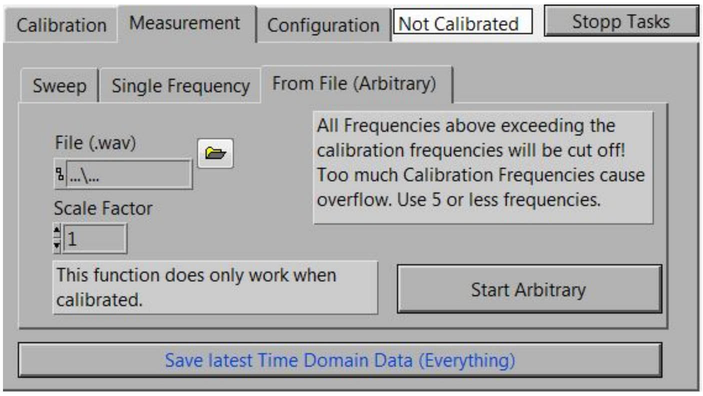

File (.wav) ...\...

Scale Factor 1

All Frequencies above exceeding the calibration frequencies will be cut off! Too much Calibration Frequencies cause overflow. Use 5 or less frequencies.

This function does only work when calibrated.

Figure 6.4: Measured vibration profile tab

6.1.2.1 Magnetic circuit design

The proposed designs for the magnetic circuit are shown in Figure 6.5. The selected configurations for the magnets arrangement and their magnetization directions are selected based on simulation results presented in section 5.2.1.2. The width of the air gap .i.e., the distance between the left and the right parts of the magnetic circuit, d_{mc}, can be adjusted using a simple screw/nut system between the magnet supports and the housing of the converter. The variation of d_{mc} yields to a change of the magnetic force resulting from the interaction between the magnets and the two Terfenol-D layers. This causes variation of the resonance frequency of the structure in addition to the variation of the generated voltage from the transducer due to the change of the magnetic field acting on the ME composite.

6.1.2.2 Magnetoelectric transducer

Three ME transducers are fabricated. The layers of the ME transducers are bonded using three different epoxy adhesives.
The first transducer is fabricated using a similar approach which was reported in [91]. The three layers are bonded with a conductive epoxy resin (CircuitWorks Conductive Epoxy) and cured at 65 °C for 2 h under mechanical load to provide a strong bond between the Terfenol-D and the PMNT plates.
The two other transducers are fabricated using a novel bonding adhesive based on carbon nanotubes (CNTs). It should be noted that this method is used for the first time for the fabrication of magnetoelectric transducers. More details about the preparation and the fabrication process of the ME transducers using this novel method are presented in the following section (6.1.2.3).

6.1.2.3 Novel fabrication method of magnetoelectric laminate composites

An increasing attention has been drawn to carbon nanotubes since their discovery by Sumio Iijima in 1991 [148]. CNTs are cylindrical shells made by rolling grapheme sheets into a seamless cylinder [149]. Due to their unique electronic structure of graphite and

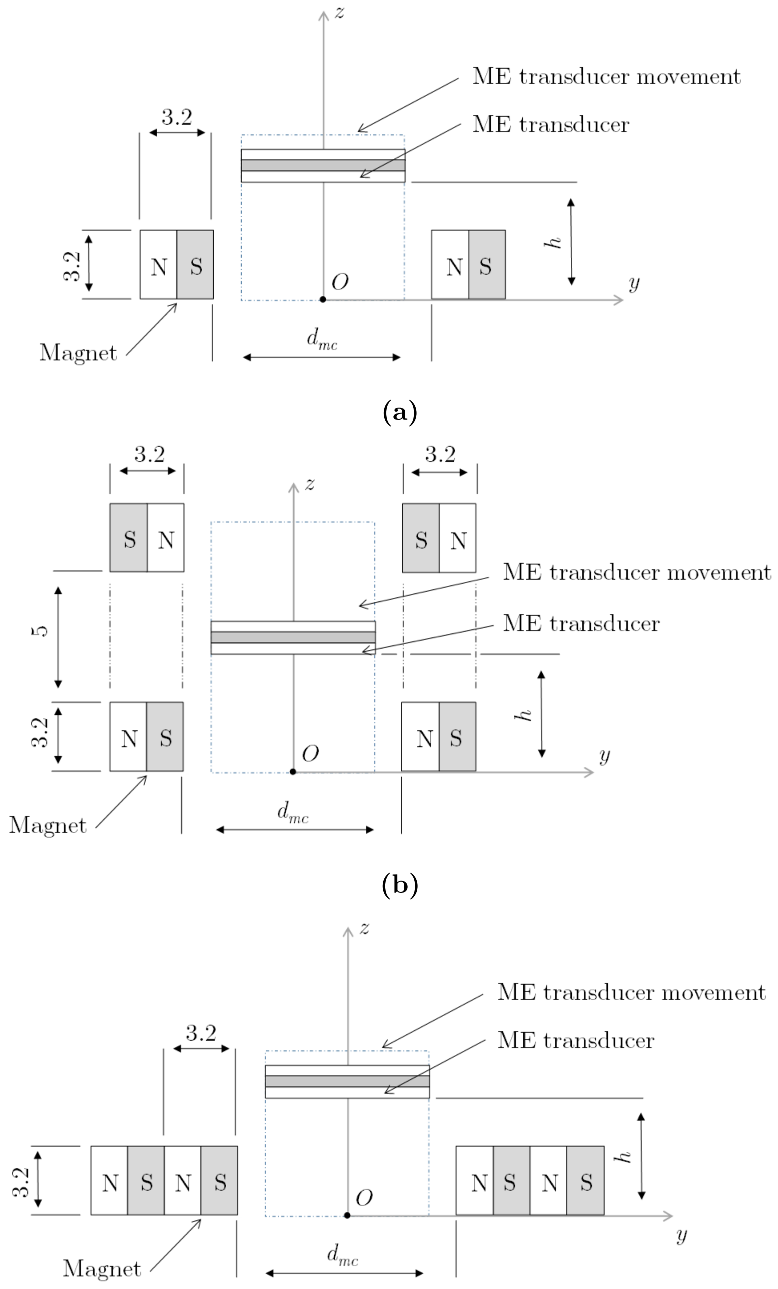

(a)

(b)

(c)

Figure 6.5: ME transducer and magnets and their relative placements for (a) Two magnets magnetic circuit design, (b) Four magnets magnetic circuit design, and (c) Four stacked magnets magnetic circuit design

their 1-D structure, CNTs have outstanding electrical properties [150, 151]. It was reported that CNTs have extremely high current densities (10^9 - 10^{10} A/cm^{-2}) [152, 153], which is more higher than in copper.

CNTs can be divided into two main categories; single-wall nanotubes (SWNTs) and multi-walled nanotubes (MWNTs). It was found that the electron transport in MWCNTs and SWCNTs are similar.

For these reasons, MWCNTs are mixed with an epoxy resin for bonding the piezoelectric layer to the two Terfenol-D plates in order to ensure good electrical and mechanical properties. A great advantage of the proposed technique is that a strong bond between the layers can be obtained at room temperature contrarily to traditional bonding methods. This is important to avoid depolarization of the PMNT layer. Furthermore, the use of the polymer (epoxy resin with hardener) can protect CNTs from slippage phenomena and ensure better load transfer.

Two dispersions with different concentrations of MWCNTs are proposed in order to study the effect of the CNTs concentration on the performance of the ME transducer and to compare it to the case when the conductive epoxy resin proposed in section 6.1.2.2 is used as a bonding interface for the layers.

Materials

The MWCNTs employed in this study were obtained from Southwest Nano Technology and used without purification or any further chemical treatment. The degree of purity of the MWCNTs is more than 95 %, with a diameter ranging from 6 to 9 nm and a length around 5 μm.

The epoxy resin used in this study is epoxy L20 purchased from R&G Faserverbundwerkstoffe composite technology, GmbH, Germany which is a bisphenol A/F resin diluted with a difunctional butanediol diglycidyl ether. The presence of bisphenol F component reduces the viscosity and prevents the resin from forming crystals at low storage temperatures. This resin has a low surface tension and excellent wetting properties which induce good filler wetting with fibre materials.

Preparation

Nanotubes with different weight percentages of MWCNTs (1 wt.% and 2 wt.%) were prepared using direct mixing method. Firstly, MWCNTs were added to epoxy resin

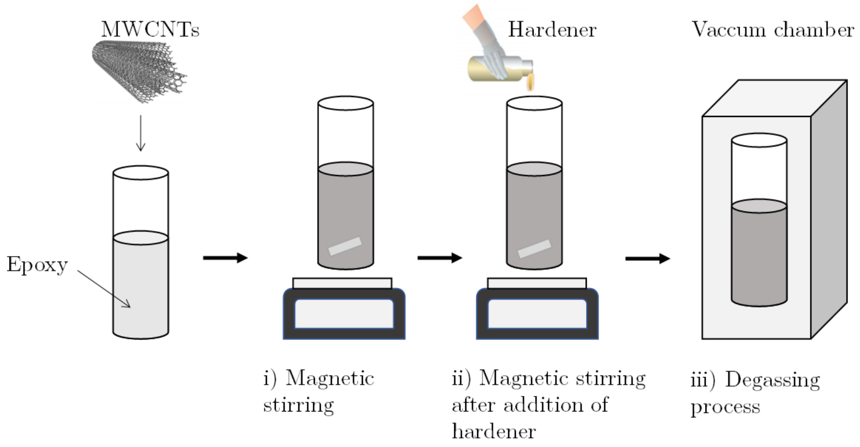

Figure 6.6: Preparation process of the polymer/ MWCNTs

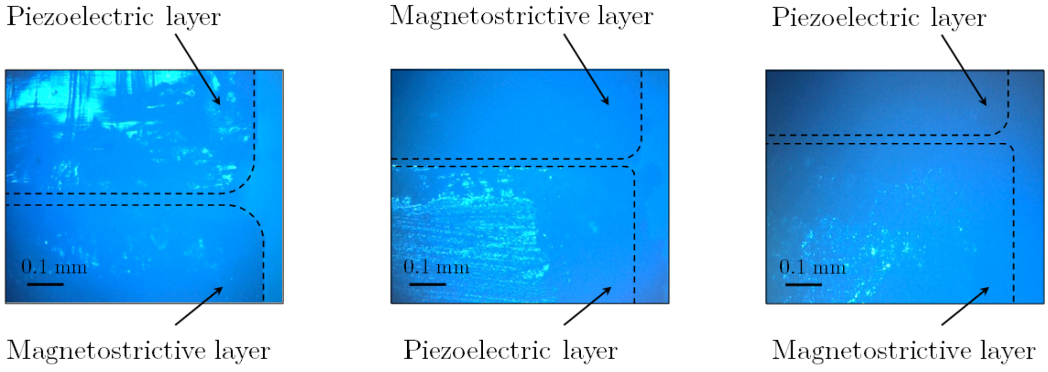

(a) ME (Conductive epoxy) **(b)** ME (1 % CNTs) **(c)** ME (2 % CNTs)

Figure 6.7: AFM camera view of the bonding interfaces for the three ME transducers. Dashed lines present the borders of the layers

followed by magnetic stirring at 600 rpm at a temperature of 80 °C to reduce the viscosity and enhance the mobility of the MWCNTs in the polymer matrix. Then, after 2 h of mixing, the needed amount of hardener was added and mixed with same condition for 10 min. At the end, the mixtures were vacuumed for 30 min to remove bubbles at room temperature. Two magnetoelectric transducer are formed using the two dispersions with different weight percentages of MWCNTs (1 wt.% and 2 wt.%). Figure 6.6 presents a schematic of the fabrication process of the solution.

In the following, we refer to the ME converters bonded using the conductive epoxy resin, epoxy with 1 wt.% MWCNTs and epoxy with the 2 wt.% MWCNTs by ME (conductive epoxy), ME (1 % CNTs) and ME (2 % CNTs) respectively.

In order to evaluate the bonding of the three ME transducers, Figure 6.7 shows an AFM camera view of the bonding interfaces. It can be seen that the thicknesses of the resulting bonding interfaces are similar in the case of ME (1 % CNTs) and ME (2 % CNTs) while a thicker bonding interface is observed in the case of ME (conductive epoxy).

Additionally, the measurement of the complete thicknesses of the three ME transducers by means of a digital caliper proves that the ME (2 % CNTs) is thinner than the ME (1 % CNTs) and ME (conductive epoxy) by 0.1 and 0.2 mm respectively.

6.1.3 Output characteristics under harmonic excitations for different magnetic circuit designs

6.1.3.1 Four magnet magnetic circuit design

In this section, the characterization of the converter having four magnets magnetic circuit (see Figure 6.5 (b)) is accomplished under harmonic excitations. In this case, the ME (2 % CNTs) is used and the width of the air gap between the magnets is fixed to $d_{mc} = 17$ mm. The first investigation focuses on the influence of the applied vibration amplitude. Figure 6.8 (a) and (b) show the peak to peak (pk-pk) open circuit

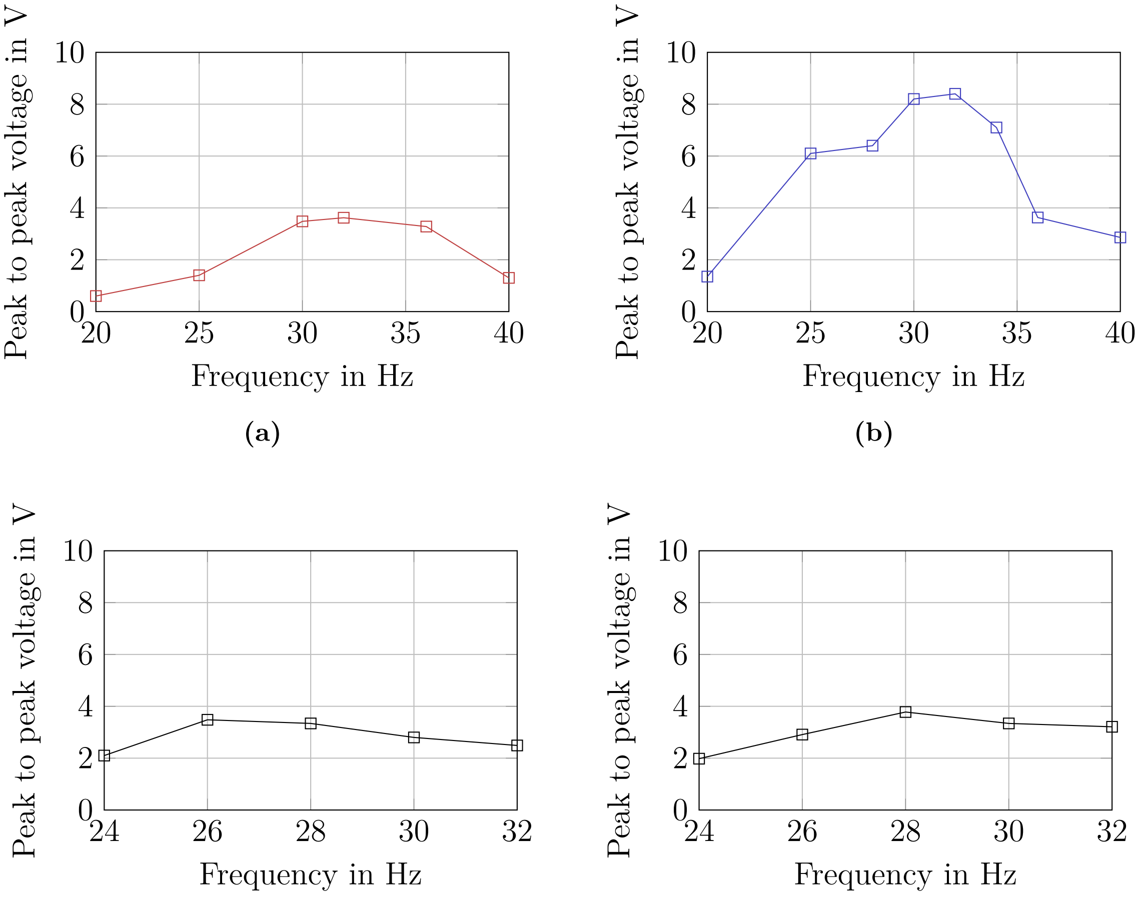

(a) **(b)** **(c)** **(d)**

Figure 6.8: Output characteristics of the converter with a four magnets magnetic circuit design for different applied amplitudes: (a) 0.5 mm (b) 1 mm, and accelerations: (c) 1 g, (d) 2g

voltage of the transducer in response to 0.5 mm and 1.5 mm vibration amplitudes, respectively, for a frequency range from 20 Hz to 40 Hz. As it can be seen the maximum pk-pk voltages are about 3.6 V and 8.4 V at 32 Hz for the two applied amplitudes, respectively.

Results of the experimental investigations for 1 g and 2 g accelerations are depicted in Figure 6.8 (c) and (d), respectively. Measurements are performed for a frequency range between 24 Hz and 32 Hz. It can be clearly seen that the resonance frequency of the converter changes with acceleration. In fact, around 3.5 V and 3.8 V maximum pk-pk voltages are obtained for 26 Hz and 28 Hz resonance frequencies for 1 g and 2 g applied accelerations, respectively. This change of resonance frequency in response to the change of acceleration is typical for non-linear system [85, 142].

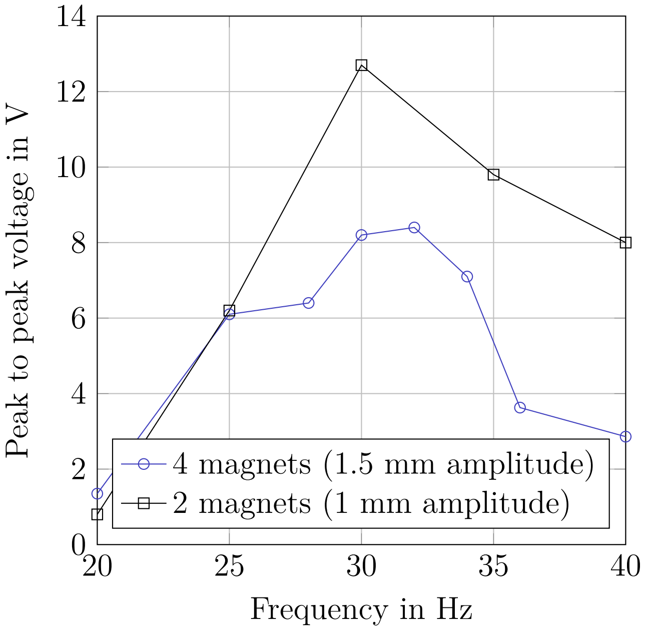

Figure 6.9: Output characteristics of the converter with two and four magnets magnetic circuit designs for 1 mm and 1.5 mm vibration amplitudes, respectively

6.1.3.2 Two magnets magnetic circuit design

Comparison to the four magnets magnetic circuit design

The converter is tested when the magnetic circuit is formed of two magnets (see Figure 6.5 (a)). The ME transducer and the width of the air gap between the magnets are similar to those mentioned in section 6.1.3.1, i.e., ME (2 % CNTs) and $d_{mc} = 17$ mm. The output voltage of the converter is investigated for a frequency range from 20 Hz to 40 Hz under an applied harmonic excitation with 1 mm amplitude. Experimental results are shown in Figure 6.9 and are compared to the case when a four magnets magnetic circuit design is implemented. It can be observed that the open circuit pk-pk voltage which is generated in the configuration under consideration is higher than that of the four magnets configuration even for a 0.5 mm lower vibration amplitude. This confirms the simulation results reported in the previous chapter in section 5.2.1.2. Additionally, different resonance frequencies are obtained for the converter for the two magnetic circuit designs due to the difference of the magnetic force resulting from the interaction between the magnets and the transducers.

Influence of the air gap width

In this section, the aim is to evaluate the influence of the variation of the air gap width d_{mc} on both the voltage outcome generated by the transducer and the resonance frequency of the converter. For these purposes, measurements are proposed for two different d_{mc} values which are 17 mm (Similar to that used in the previous sections) and 16 mm. The applied excitation amplitude for both cases is fixed to 1 mm. Figure 6.10 (a) and (b) show, respectively, the open circuit pk-pk voltage output of the ME for $d_{mc} = 17$ mm and 16 mm.

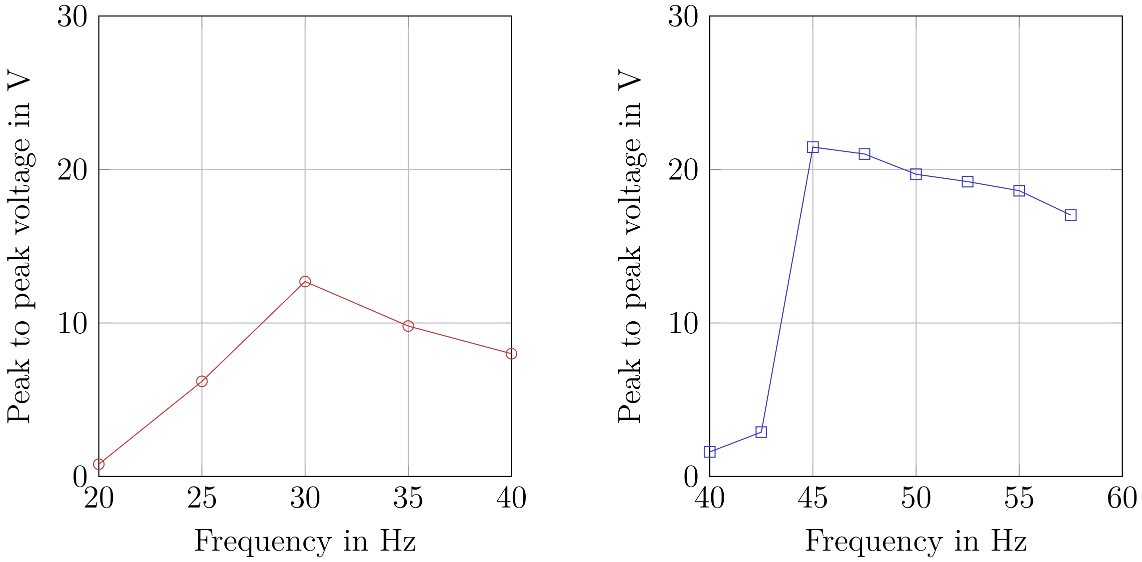

(a) **(b)**

Figure 6.10: Output characteristics of the converter with two magnets magnetic circuit design under 1 mm harmonic excitations amplitude for (a) 17 mm air gap width (b) 16 mm air gap width

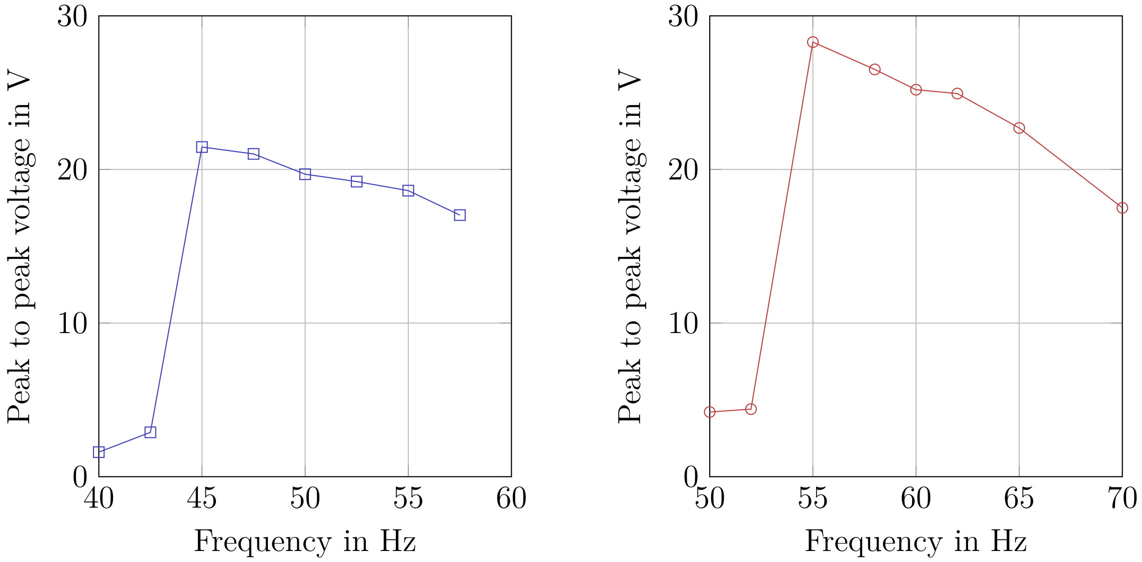

(a) **(b)**

Figure 6.11: Output characteristics of the converter with two magnets magnetic circuit design under 1 mm harmonic excitations amplitude for (a) 16 mm air gap width (b) 15 mm air gap width

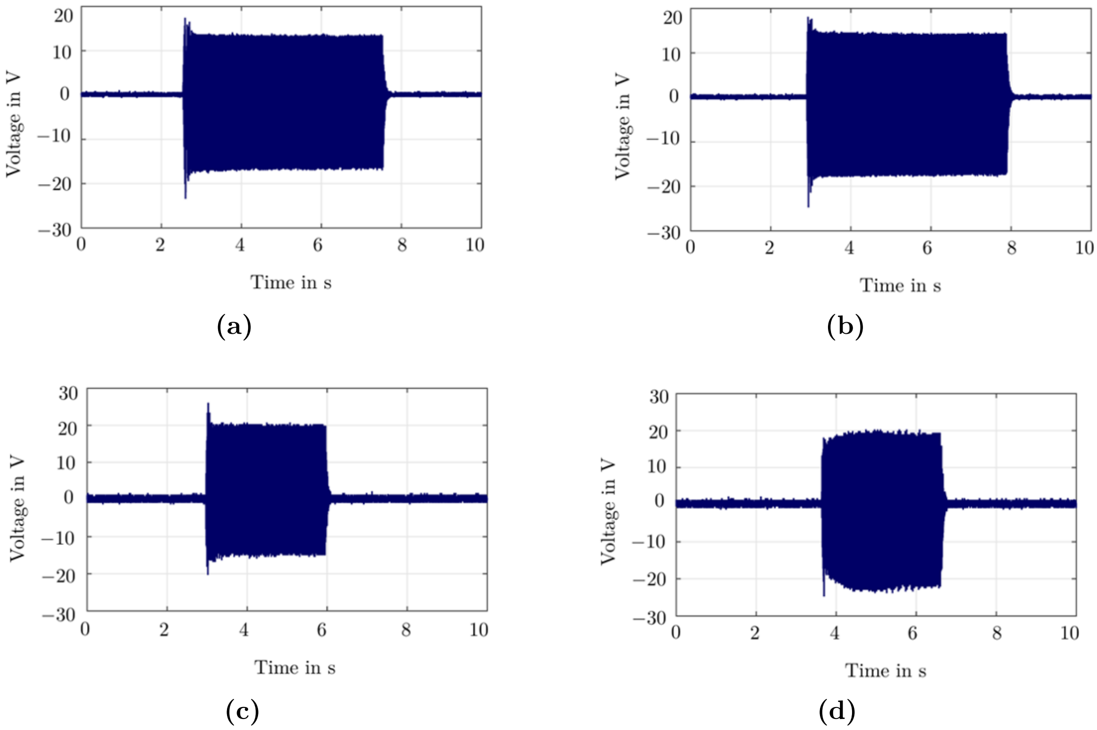

(a) (b) (c) (d)

Figure 6.12: Influence of increasing the excitation amplitudes on the output characteristics of the converter with two magnets magnetic circuit design for $d_{mc} = 15$ mm at 55 Hz for (a) 1.2 mm, (b) 1.5 mm, (c) 1.8 mm and (d) 2 mm

For a shorter gap width ($d_{mc} = 16$ mm), it is demonstrated that the converter is able to generate about 21.8 V pk-pk open circuit voltage which is about 170 % of that generated by the converter for $d_{mc} = 17$ mm under the same excitation amplitude.
On the other hand, by taking the effect on the frequency into consideration, it is found that the resonance frequencies of the converter are 30 Hz and 45 Hz for $d_{mc} = 17$ mm and $d_{mc} = 16$ mm which correspond, respectively, to 5 Hz and 20 Hz deviations from the natural frequency of the structure found by finite element simulation in section 5.4.2.1. This is due to the magnetic force between the magnetic circuit and the transducers which is increased significantly by reducing the separation distance between the magnets and the Terfenol-D layers. Furthermore, the converter is tested for a shorter air gap width, $d_{mc} = 15$ mm and compared to the case when $d_{mc} = 16$ mm.
Experimental results are depicted in Figure 6.11. It can be seen that the voltage curve and the resonance frequency is shifted towards right by 10 Hz. Additionally, the maximum pk-pk voltage for $d_{mc} = 15$ mm is slightly higher than that for $d_{mc} = 16$ mm. These results indicate that the magnetic force has increased for $d_{mc} = 15$ mm compared to $d_{mc} = 16$ mm but this variation is less than that obtained in case of an air gap between $d_{mc} = 16$ mm and $d_{mc} = 17$ mm.

The influence of increasing the excitation amplitudes at this short air gap width, d_{mc} = 15 mm, is investigated. Measurements are done at the resonance frequency of the converter which is 55 Hz and results are shown in Figure 6.12.
As shown in Figure 6.12, the open circuit pk-pk voltage increases from 28.1 V to around 44 V for 1 mm to 2 mm applied amplitudes, respectively.
Investigations of the output characteristics of the converter under resistive loads are carried out in order to evaluate the power output of the transducer. Measurements are made for 2 mm vibration amplitude at 55 Hz. Figure 6.13 (a) and (b) show the pk-pk voltage and the power which can be generated by the transducer at resonance for 2 mm amplitude of vibration. Results indicate that the maximum generated power for this configuration is about 0.4 mW at a 560 kΩ load resistance.

6.1.3.3 Four stacked magnets magnetic circuit design

The third investigated magnetic circuit design is the one which uses two stacked rectangular magnets on the left and the right side of the magnetic circuit as depicted in Figure 6.5 (c)). In this section, the ME (2 % CNTs) is used and the width of the air gap between the magnets is fixed to d_{mc} = 15 mm.
The open circuit peak to peak voltage of the converter under 1 mm amplitude of excitations for a frequency range from 60 Hz to 80 Hz is shown in Figure 6.14. The variation of the voltage output has similar behaviour to those obtained in the case of two magnets magnetic circuit design (see Figure 6.11).

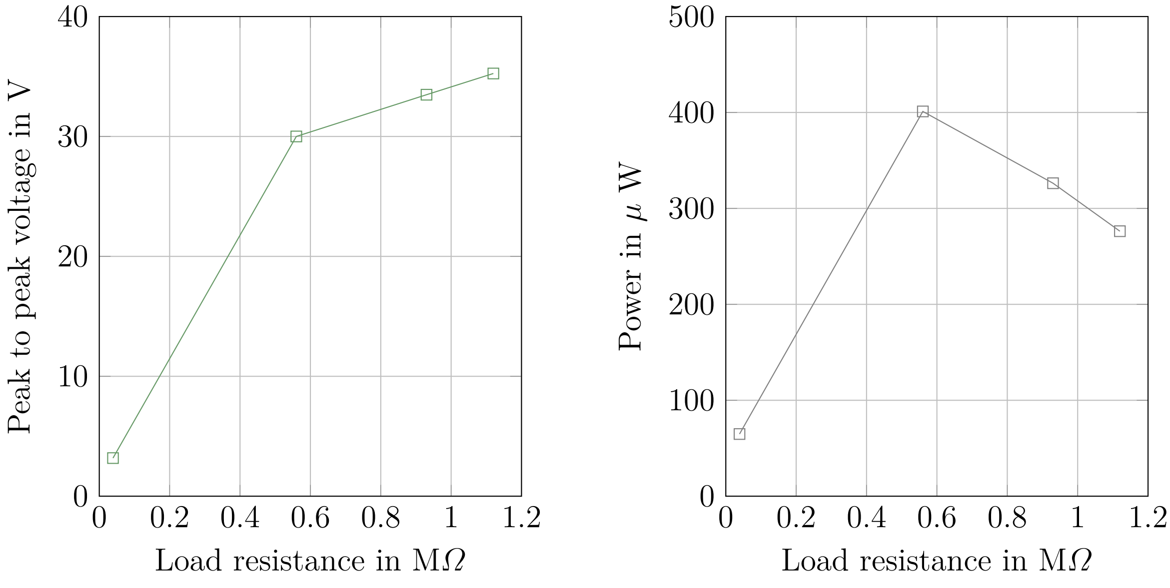

(a) **(b)**

Figure 6.13: Case of the converter with two magnets magnetic circuit design for 2 mm amplitudes and d_{mc} = 15 mm at 55 Hz under resistive loads (a) Measured peak to peak voltage, (b) Measured power

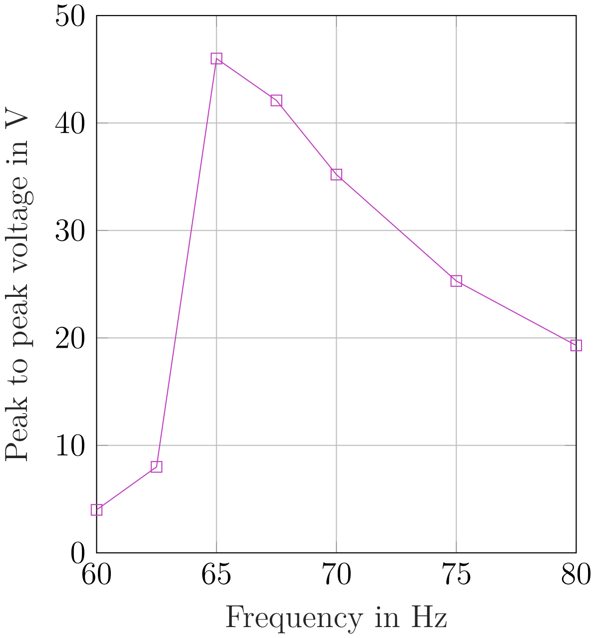

Figure 6.14: Output characteristics of the converter with four staked magnets magnetic circuit design under 1 mm harmonic excitations amplitude for a 15 mm air gap width

However, higher pk-pk voltage outputs are observed which is about 18 V higher than that obtained in the case of two magnets magnetic circuit design at resonance frequency. Furthermore, the resonance frequency of the converter in this case is 65 Hz which is 10 Hz higher than that in the case with two magnets, and about 41 Hz higher than the natural frequency of the structure obtained with finite element analysis. This is mainly related to the higher magnetic field strength which can be generated by the four stacked magnets. In other words, the magnetic force between the magnets and the Terfenol-D layers is much more higher in this case (see Figure 6.5 (c)) than the two other magnetic circuit designs (see Figure 6.5 (a) and (b)). Besides, the output characteristic of the converter under resistive loads is investigated. Measurements are made for 1 mm vibration amplitude at 65 Hz. Figure 6.15 (a) and (b) show the pk-pk voltage and the power which can be generated by the transducer. It can be seen that the maximum generated power for is about 0.57 mW at a 560 kΩ load resistance which is higher than that obtained in the two magnets magnetic circuit configuration measured for 2 mm vibration amplitudes.

Furthermore, it is found that for the four stacked magnets arrangement, reducing the air gap width d_{mc} to about 14 mm leads to opposite magnetic force variation compared to that found in section 6.1.3.2. In this case the resonance frequency of the converter is 40 Hz, while 65 Hz is found for $d_{mc} = 15$ mm.

Figure 6.16 (a) and (b) shows respectively the open circuit voltage output and the voltage of the converter under 560 kΩ load resistance for 1 mm excitation amplitude at 40 Hz. Results demonstrate that a maximum output power of 2.42 mW can be generated by the converter under an excitation with these parameters.

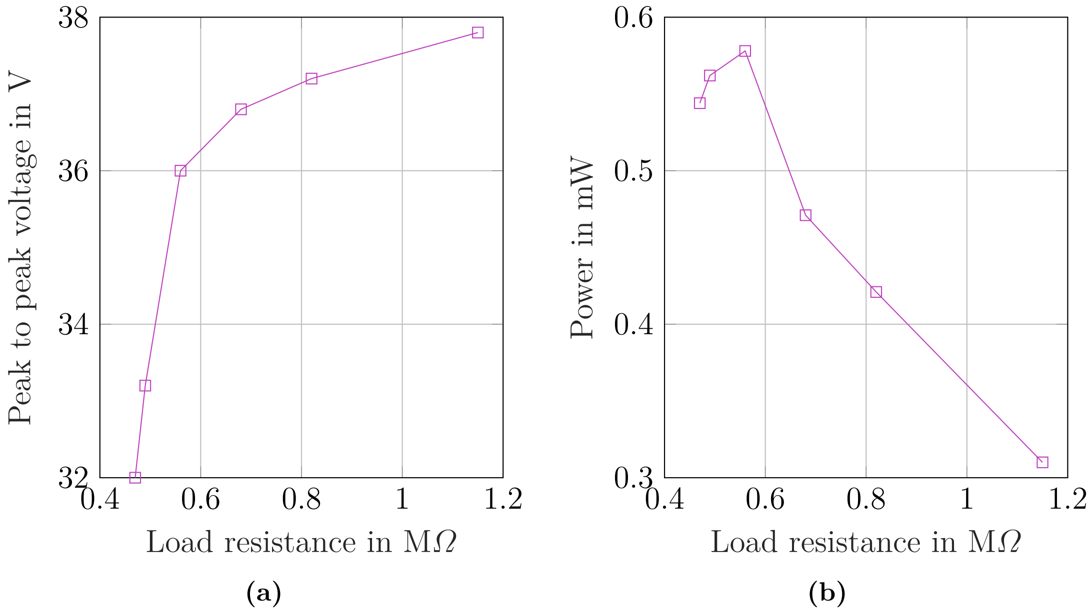

Figure 6.15: Case of the converter with four stacked magnets magnetic circuit design for 1 mm amplitude and $d_{mc} = 15$ mm at 65 Hz under resistive loads (a) Measured peak to peak voltage, (b) Measured power

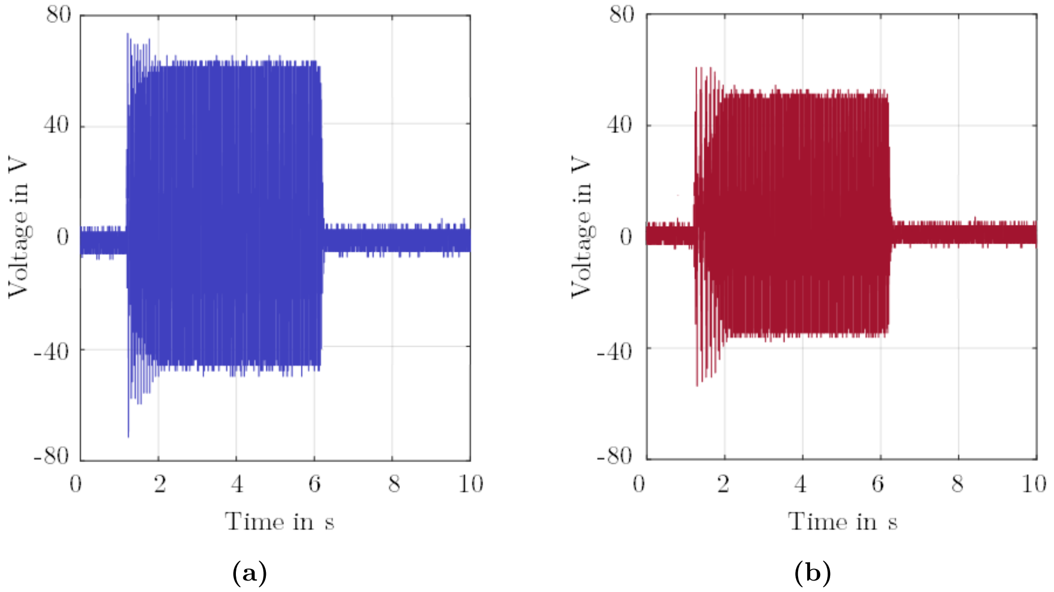

Figure 6.16: Voltage output of the converter with ME (2 % CNTs) for $d_{mc} = 14$ mm under 1 mm vibration amplitude at 40 Hz (a) Open circuit voltage (b) Voltage under 560 kΩ load resistance

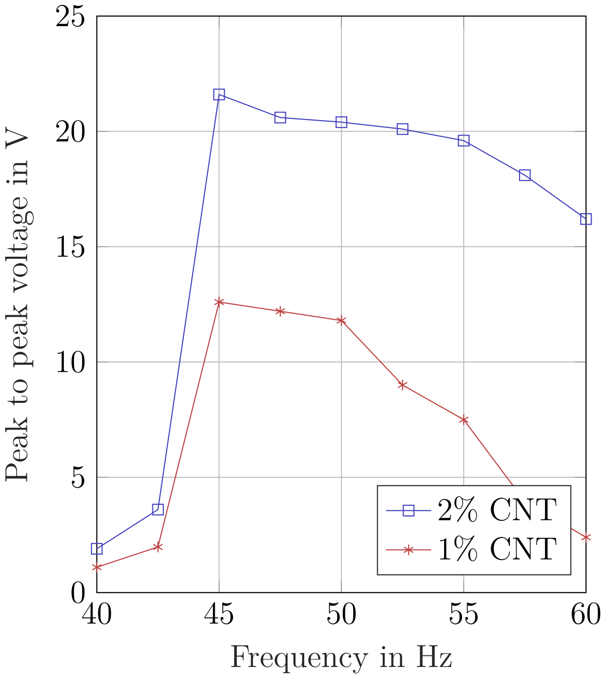

Figure 6.17: Open circuit pk-pk voltage of the converter with ME (2 % CNTs) and ME (1 % CNTs) under 1 mm vibration amplitude for $d_{mc} = 16$ mm

6.1.4 Output characteristics under harmonic excitations for different bonding adhesives

Here, the aim is to compare the output characteristics of the transducers, fabricated with different bonding adhesives, under similar operating conditions in terms of frequency, amplitude, magnetic circuit design and air gap width, d_{mc}.

Furthermore, since the three ME transducers have different bonding adhesives and therefore different equivalent capacitances, evaluation of the power output under resistive loads is proposed. Prior to the investigation under resistive loads, determination of similar operating condition is required since the three transducers are attached to different cantilever beams having same dimensions. The magnetic circuit and the housing of the converter are the same for the three cases. For the comparison, the air gap width, d_{mc}, is fixed to 16 mm. Additionally, the two magnets magnetic circuit design is selected for the experimental investigations which are performed under 1 mm harmonic excitations amplitude.

The resonance frequency of the structure is employed to verify that the converters with different ME transducers are placed correctly. Figure 6.17 shows the voltage output of the two ME transducers: ME (2 % CNTs) and ME (1 % CNTs). As It can be seen, the two converters have the same resonance frequency of 45 Hz.

With maintaining the same operating conditions, the voltage and power output of the three ME transducers are investigated at the resonance frequency (45 Hz) under resistive loads from 120 kΩ to 1.18 MΩ.

Results are presented in Figure 6.18. It is found that the highest power is obtained with ME (2 % CNTs) which is about 3 times and 10 times the power output in case of

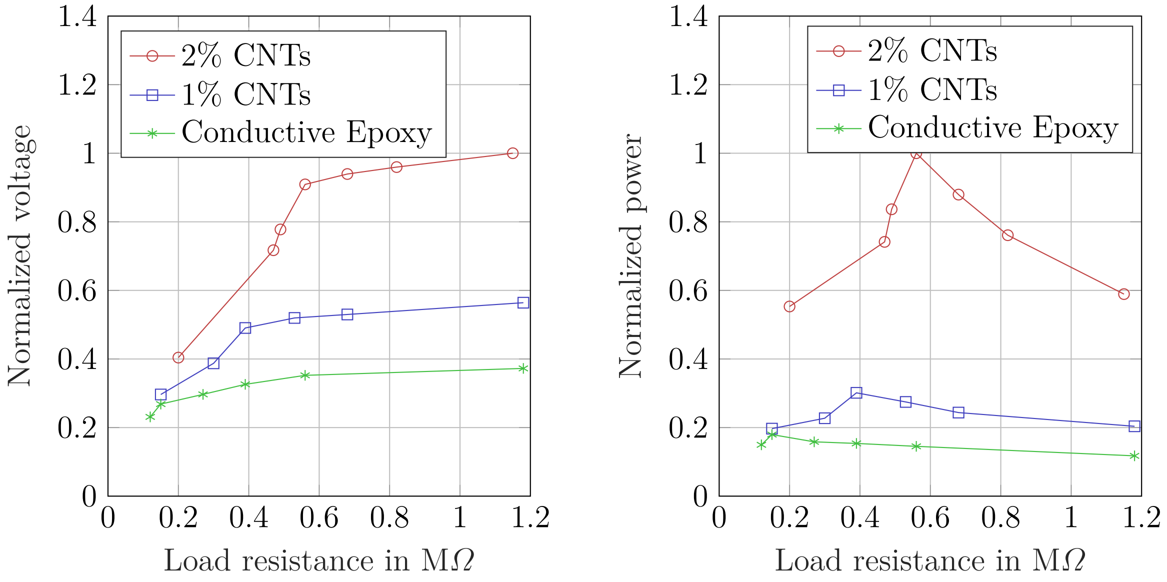

(a) **(b)**

Figure 6.18: Comparison of the output characteristics of the transducers, fabricated with different bonding adhesives (a) Normalized output voltage under load resistances, and (b) Normalized output power under load resistances

ME (1 % CNTs) and ME (Conductive epoxy), respectively. These results prove that the use of epoxy/CNTs dispersion for the bonding of the three layers can significantly improve the efficiency of the ME converter.

6.1.5 Output characteristics under real vibration profiles

In the following, measurements are conducted using random vibration profiles in order to evaluate the ME converter under real applied excitations. In fact, two random vibration profiles are proposed for the experimental investigations. The first one is a random signal generated with Matlab. The duration of the signal is fixed to 10 s, while the maximum amplitude is 1 mm.

The second signal is resulting from real vibration measurement in a lawn mower. The measurement system was attached to a lawn mower, and the vibration data are recorded for about 35 s of working time. Data along the three axes x (horizontal axis in the direction of the lawn mower movement), y (horizontal axis perpendicular to the direction of the lawn mower movement) and z (vertical axis) are measured.

Figure 6.19 (a), (c), and (e) present the recorded vibration profiles along x-axis, y-axis and z-axis respectively. It can be seen that low acceleration levels are obtained and are comparable in the three axes x, y and z. It is noticed that the maximum measured average acceleration is around 3 m/s^2. Fourier spectrum for the measured accelerations along x-axis, y-axis and z-axis are shown in Figure 6.19 (b), (d), and (f), respectively, in order to characterize typical frequencies in the measured profiles.

Because of the limitation of the used shaker control system, the maximum calibration frequency of the shaker was fixed to 80 Hz. In other words, all frequencies above 80 Hz are removed when the vibration profiles are reproduced by the shaker. Two magnetic circuit designs are used for the characterization of the voltage output under real vibration excitations. The designs are; the one with two magnets arrangement for

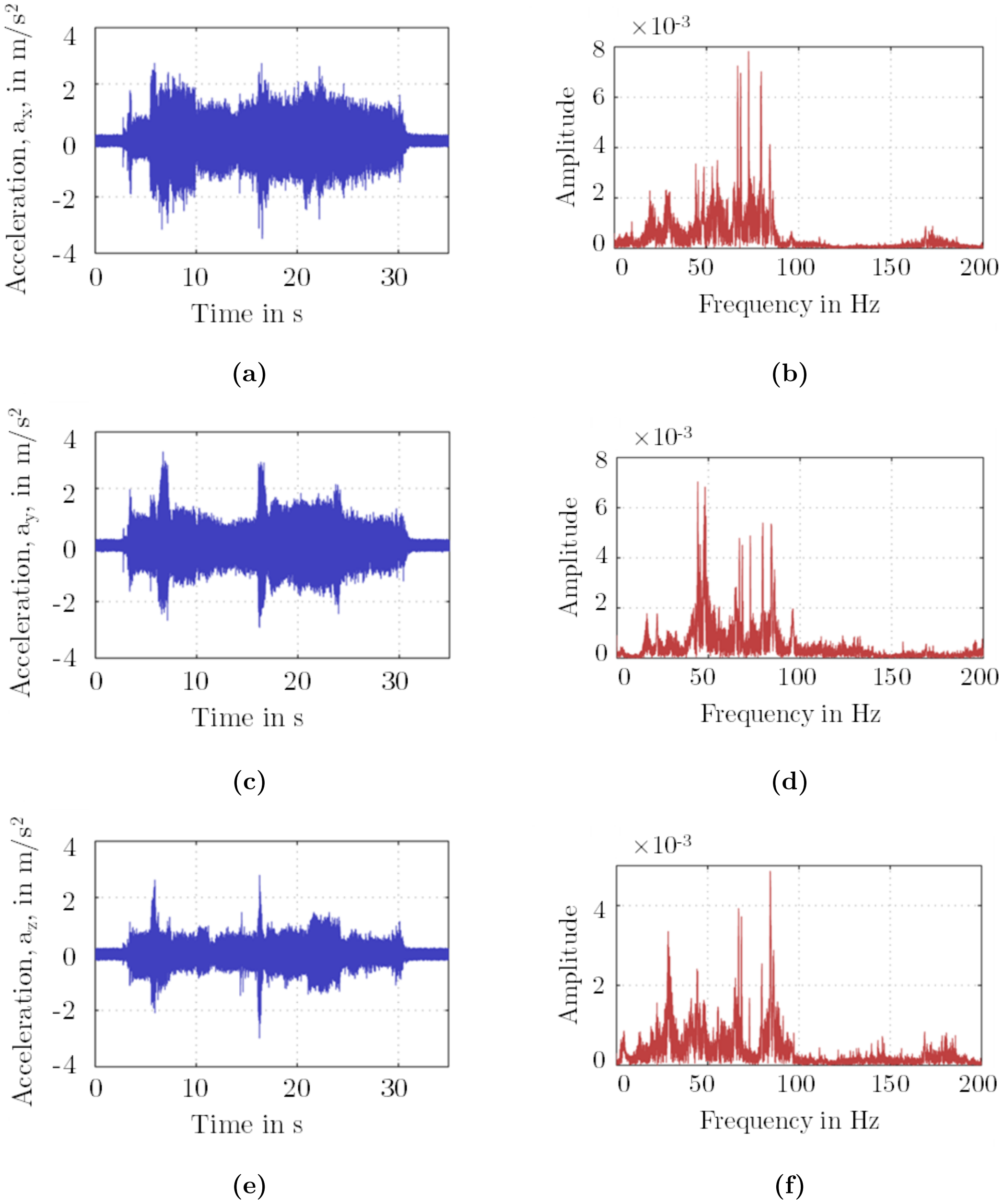

(a) (b)

(c) (d)

(e) (f)

Figure 6.19: Acceleration profiles measured in the lawn mower along the three axes (a) x-axis, (c) y-axis, (e) z-axis and the corresponding Fourier transform for the accelerations (b) a_x, (d) a_y, (f) a_z

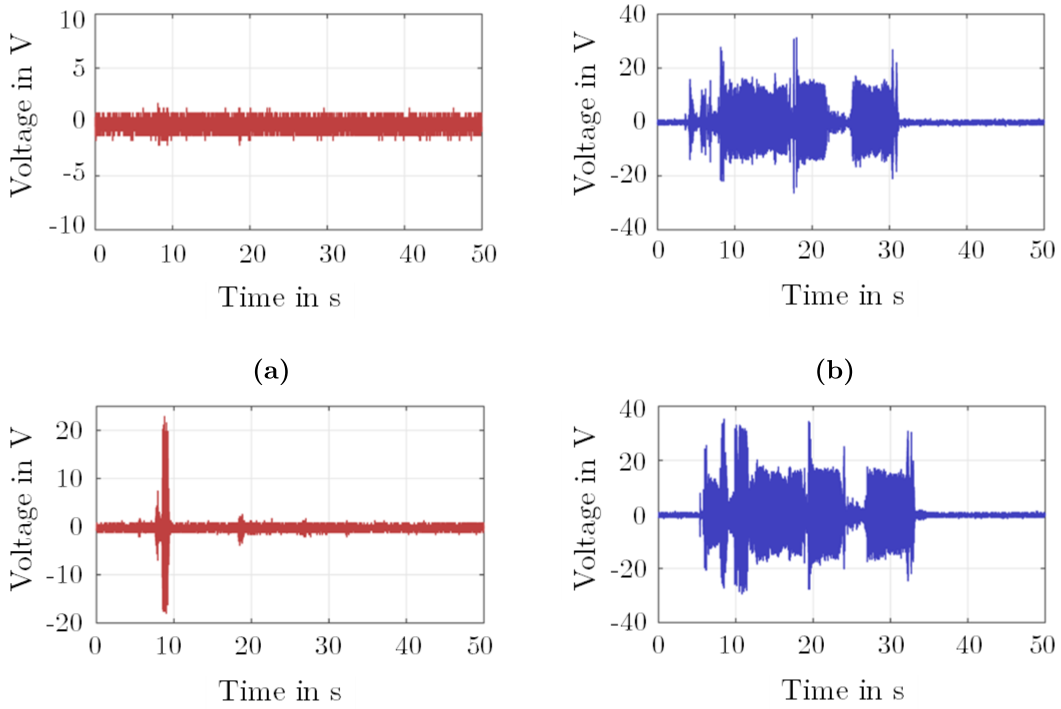

(a) **(b)**

(c) **(d)**

Figure 6.20: Open circuit voltage output of the converter with 2 magnets magnetic circuit in response to the measured lawn mower acceleration along x-axis for (a) 1 scale factor, and (c) 2 scale factor. Open circuit voltage output of the converter with 4 stacked magnets magnetic circuit in response to the measured lawn mower acceleration along x-axis for (b) 0.5 scale factor, and (d) 0.7 scale factor

$d_{mc} = 16$ mm and the demonstrator with four stacked magnets for $d_{mc} = 15$ mm. The resonance frequencies for the two demonstrators are 45 Hz and 65 Hz, respectively. The prototype with a magnetic circuit design with 2 magnets was tested under respectively 1 and 2 scale factors of the real profiles, while the converter based on four stacked magnets arrangement is tested under 0.5 and 0.7 scale factors of the same profiles. Figures 6.20, 6.21 and 6.22 show the open circuit output voltage of the two prototypes in response to measured vibration along x-axis, y-axis and z-axis respectively. As it can be seen, the prototype using 2 magnets arrangement is able to generate valuable voltage output (40 V pk-pk) only in the case of vibration profile along y-axis that can be explained by the fact that the characteristic frequency in this profile is close to the resonance frequency of the prototype (45 Hz). On the other hand, higher voltage outputs are observed with the prototype which uses four stacked magnets arrangement. Around 60.4 V, 65.2 V and 44.1 V pk-pk voltages were obtained with this design under 0.7 scale factor of the three applied profiles along x-axis, y-axis and z-axis respectively.

Furthermore, the two prototypes (with two magnets and with four stacked magnets) were tested using the random profile generated with Matlab whit different scale factors.

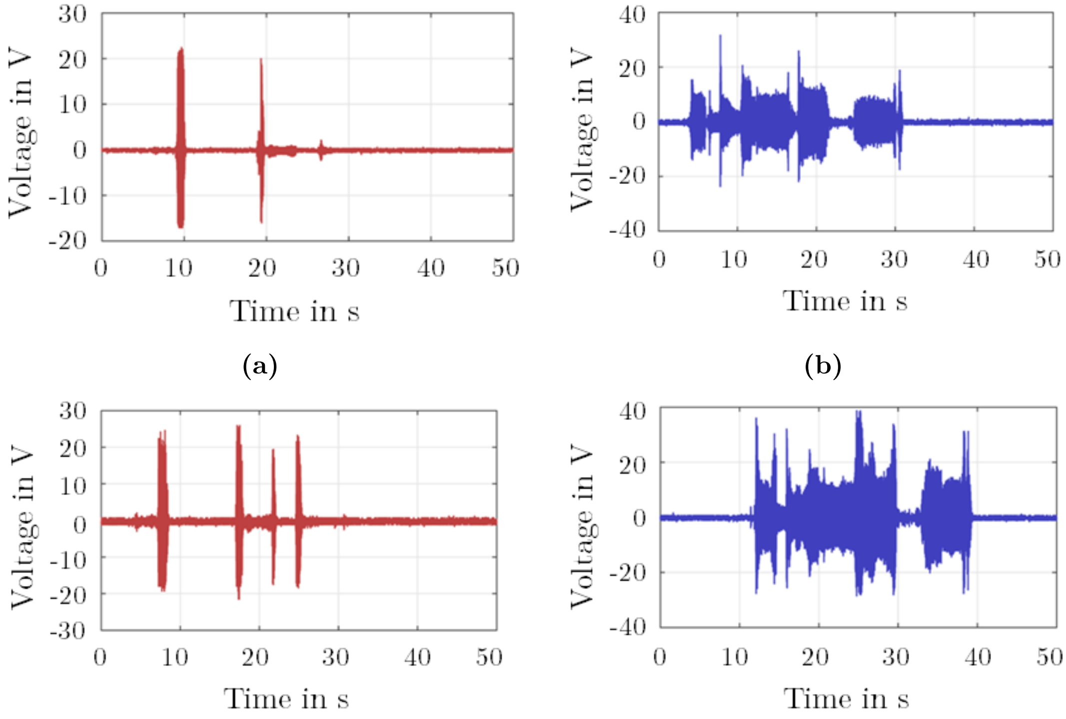

(a) (b)

(c) (d)

Figure 6.21: Open circuit voltage output of the converter with 2 magnets magnetic circuit in response to the measured lawn mower acceleration along y-axis for (a) 1 scale factor, and (c) 2 scale factor. Open circuit voltage output of the converter with 4 stacked magnets magnetic circuit in response to the measured lawn mower acceleration along y-axis for (b) 0.5 scale factor, and (d) 0.7 scale factor

The main difference to the previous investigations is that there is no dominant frequency which can be found in this random vibration profile. The applied scale factor for the prototype with two magnets design is 1 while 0.3 scale factor of the vibration profile is applied for the prototype with four stacked magnets arrangement.

Experimental results are shown in Figure 6.23. It is found that maximum 38 V (with the 2 magnets design) and 61 V pk-pk (with the four stacked magnets design) output voltages can be generated under 1 and 0.3 scale factors of applied vibration respectively. These results prove the significant improvement in the ME converter performance which is reached using the four stacked magnets design not only in terms of increasing the magnetic field variation acting on the ME transducer at a fixed amplitude but also by the ability of tuning the resonance frequency of the structure by varying d_{mc} to match the characteristic frequencies of random applied excitations.

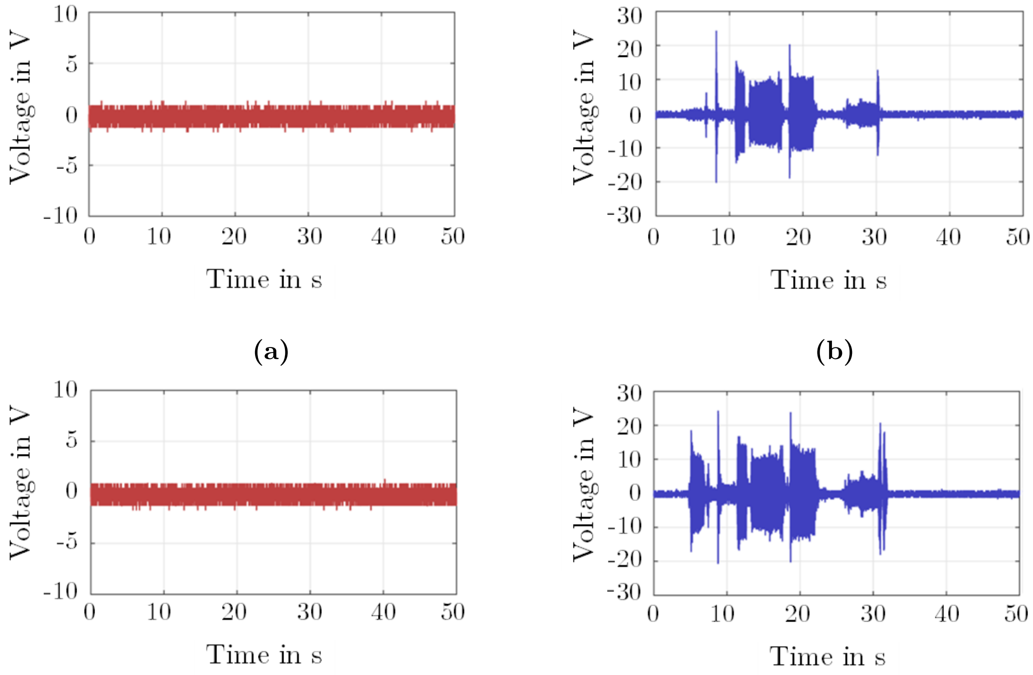

(a) **(b)**

(c) **(d)**

Figure 6.22: Open circuit voltage output of the converter with 2 magnets magnetic circuit in response to the measured lawn mower acceleration along z-axis for (a) 1 scale factor, and (c) 2 scale factor. Open circuit voltage output of the converter with 4 stacked magnets magnetic circuit in response to the measured lawn mower acceleration along z-axis for (b) 0.5 scale factor, and (d) 0.7 scale factor

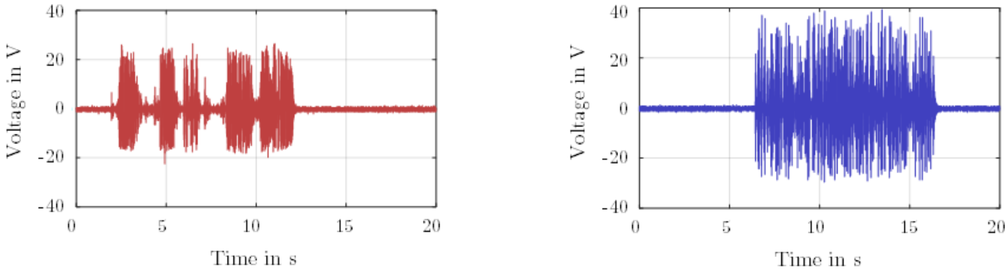

(a) **(b)**

Figure 6.23: (a) Open circuit voltage of the converter with 2 magnets magnetic circuit design in response to the random vibration profile generated by Matlab for 1 scale factor, and (b) Open circuit voltage of the converter with four stacked magnets magnetic circuit design in response to the random vibration profile generated by Matlab for 0.3 scale factor

6.2 Summary

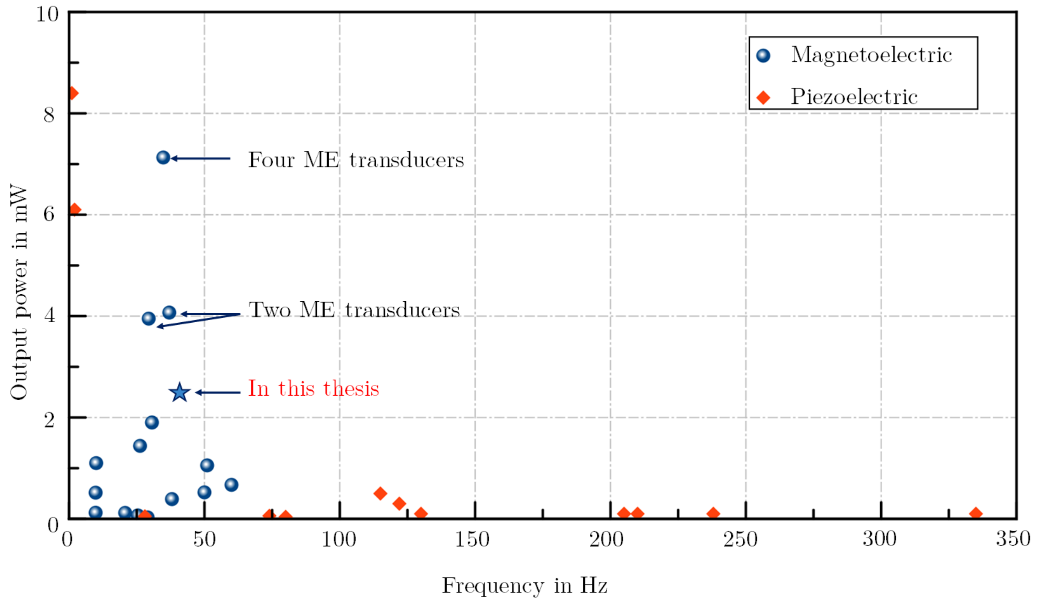

Figure 6.24: Comparison with other publications by the maximum reached output power

Different designs of ME converters are fabricated and evaluated experimentally. Three ME laminate composites are formed of a PMNT plate bonded to two Terfenol-D plates using a conductive epoxy resin, epoxy with MWCNTs concentrations of 1 % and epoxy with MWCNTs concentrations of 2 %. In total, three designs of the magnetic circuit are investigated which are; (i) a magnetic circuit formed of two magnets, (ii) a magnetic circuit formed of four magnets, and (iii) a magnetic circuit formed of four stacked magnets. Experimental investigations under harmonic and real measured vibration profiles demonstrate that the prototype using ME (2 % CNTs) and a magnetic circuit formed of four stacked magnets has better performance than the other proposed designs. Additionally, compared to other published results for magnetoelectric and piezoelectric energy harvesters, the proposed prototype shows an excellent performance (see Figure 6.24). For instance, the proposed design in this thesis is able to generate a maximum power output of 2.42 mW at 40 Hz and 1 mm vibration amplitude which exceeds the reported power outputs of other published prototypes which uses a single ME transducer. Furthermore, the proposed design allows to easily modify the resonance frequency of the converter using a simple screw/nut system which makes it very suitable for implementation in real applications.

Another advantage of using magnetoelectric converters rather than conventional cantilever beam based piezeoelectric converters is investigated in this thesis which is their longer fatigue lives. In Appendix C, an assessment of fatigue behaviour of piezo ceramics is presented in order to compare this behaviour in PE layers when they are used in ME and PE energy harvesting.

CHAPTER 7

Conclusions and outlook

The outstanding properties of magnetostrictive and piezoelectric laminate composites make them suitable for numerous applications including vibration energy harvesting. In this research ME laminate composites formed of the giant magnetostrictive material, Terfenol-D, and a piezoelectric layer, PMNT, are investigated in details aiming to develop a model based harvester design for ME converters. Several tasks were addressed in this thesis including measurement of magnetostriction, development of an accurate model for the ME composites and investigation of bonding effects in ME transducers. A prototype having three different magnetic circuit designs was fabricated. The prototype was tested using different ME transducers bonded with different adhesive layers. Experimental investigations were carried out under harmonic excitations and under random vibration profiles.

7.1 Conclusions

Energy harvesting has attracted great attention aiming to develop self-powered autonomous systems. Vibration is one of the most important sources for energy harvesting. It has considerable potential to be exploited for various indoor and outdoor applications. However, the design of an efficient vibration energy harvesting converter remains one challenging task because of the weakness, in terms of amplitude, and variable characteristic frequencies of environmental vibration. The excellent properties of the giant magnetostrictive material, Terfenol-D, have been leading to a high amount of research into the usage of the magnetoelectric principle to harvest energy from kinetic energy.

To date, many vibration converters have been proposed. Different used coupling architectures, resonant frequencies and ME laminate composite have been reported. Additionally, a comprehensive review of main developed ME converters has shown their capability to deliver power to the load from microwatts to few milliwatts under different excitations. It is concluded that most of them operate still well below their maximum possible output performance which proves the necessity to investigate various coupling interactions in ME transducers especially during size reduction.

To address this problem, a model based design of magnetoelectric vibration converter is proposed. The proposed approach is based on the investigation of the magneto-mechanical and electro-mechanical couplings in ME converters. The adhesive bonding and the frequency of the structure are also addressed in order to optimize the output energy even at low amplitude and low frequency excitations.

For the investigation of the magneto-mechanical coupling, measurement of magnetostriction in a Terfenol-D plate is performed using AFM for several relative positions between the Ms plate and the magnetic circuit as within ME converters. An approach to accurately measure both longitudinal and transversal deformations is successfully developed under variable non-uniform applied magnetic fields. This approach is based on the tracking of easily identifiable features presented at the surface of the Ms plate. The existence of these features is demonstrated first by SEM investigations. Results are determined based on cross section analyses performed on AFM topographic images with and without magnetic field which is generated by two rectangular NdBFe magnets. So far, magnetic field distribution parameters are investigated by finite element method in the proposed configurations and the correlation between AFM results and the magnetic field components is discussed.

For the investigation of the electromechanical coupling, a finite element model of a ME transducer and magnets is developed. Here, the aim is to simulate different interactions in ME converters including magnetostrictive and piezoelectric effect. The model of magnetostriction in Terfenol-D is implemented using the HB curve and the relation between strain and magnetization of the material. The model of magnetostriction is improved based on AFM investigation results to realistically reflect the Ms effect in Terfenol-D. On the whole, the FE model is able to calculate the induced voltage from the piezoelectric layer in response to magnets displacement through time dependent analysis. So far, a series of simulation models are built to investigate the major parameters in the ME transducer and the magnetic circuit such as the magnets arrangement, optimal initial position of the transducer and polarization direction of the PE layer. Based on these investigations, the design of the harvester is developed based on a cantilever beam structure. The proposed design is analysed analytically by Lindstedt-Poincaré method and the structure parameters are determined to estimate the resonance frequency and the output power using FE analysis and ME equivalent circuit.

To evaluate the proposed design, the ME vibration energy harvester is tested under harmonic excitations and real vibration profiles reproduced by an artificial excitation source. Simulation results in terms of the magnetic circuit design were evaluated. Furthermore, the effect of varying the distance between the magnets and the ME transducer is investigated. The resonance frequency of the converter can be tuned adjusting the separation distance between these two parts. This not only can improve the output energy of the converter but also can allow the use of the same design to harvest energy from different environmental vibration sources with different characteristic frequencies. On the other hand, the output performances of the prototype for three ME transducers having different adhesive layers are evaluated experimentally under the same operating conditions and the same magnetic field design.

In conclusion, it has been demonstrated that using a specific magnetic field design with stacked magnets can significantly improve the induced voltage by the transducer.

Additionally, results indicate that the use of the novel proposed bonding technique, using a dispersion of 2 wt.% CNTs mixed to an epoxy resin, shows better output performance. Specifically, the converter is able to generate 2.42 mW at 560 kΩ load resistance at 40 Hz and for 1 mm amplitude of harmonic vibration. In comparison to other published results, the converter proposed in this thesis shows an excellent output performance for low amplitude and at low frequency excitations.

Besides, assessment of fatigue behaviour of piezo ceramics is proposed at the end of this thesis. Results demonstrate that piezo ceramics used in ME converters has longer life time compared to that used in PE energy harvesters as a cantilever beam when subjected to same excitations.

7.2 Outlook

In short-term future research aspects, it is highly worth to perform some practical investigations with different magnets. Obtained results can be extended to other magnet dimensions and parameters. Specifically, magnets having heights less than that used in this work, i.e. 3.2 mm, and increasing the number of the stacked magnets can yield to further improvement in the performance of ME transducers.

Furthermore, the finite element model presented in this thesis can be optimized by considering the effect of the bonding between the three layers. In fact, the bonding interface can be modelled as one layer with a specific thickness which has an influence on the electrical and mechanical properties transmitted to the PE layer.

Besides, the performance of the proposed energy harvester still has space for further improvements by collecting the energy directly at the piezoelectric material so that the contribution of Ms layers and epoxy resin to the inner resistance are avoided. Although quite good AFM measurements are obtained, it would be interesting to

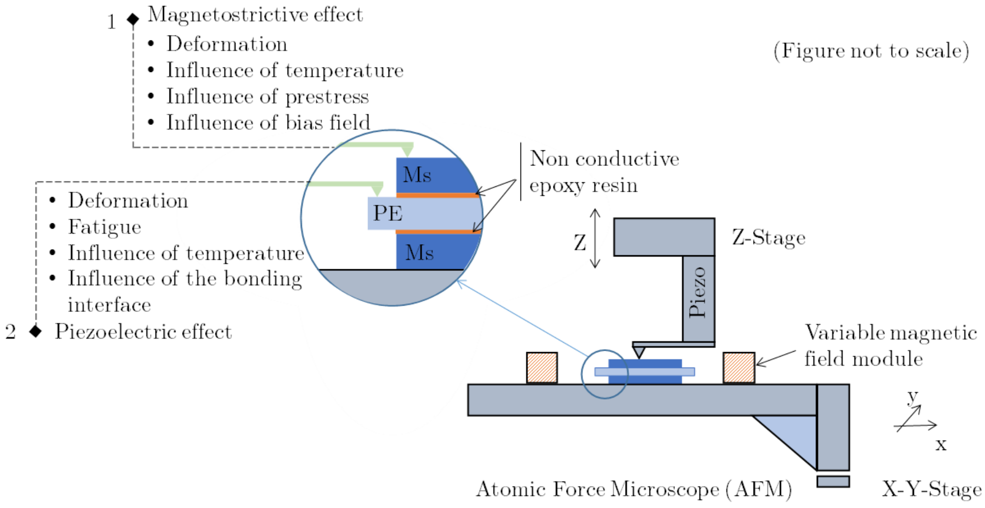

Figure 7.1: Some of the possible investigations and ideas for short and long term future research.

study the magnetostrictive effect using a variable field module (VFM) which can be be employed to generate variable magnetic fields. The VFM is able to produce different magnetic field geometries. The influence of the magnetic field strength and geometry can be studied in details. Additionally, it would be interesting to deeply investigate the deposition technique of the epoxy in order to ensure the maximum transmitted deformation to the piezoelectric layer. To clarify this in more detail, further AFM studies can be performed to address the thickness of the bonding interface and the transmitted deformation to the piezoelectric layer. Overview of some possible future developments is shown in Figure 7.1.

A Harvester design

More details about the proposed design of the harvester are given in this appendix. However, technical drawings and assembly drawing are not included in this report.

A.1 Flowchart of the harvester components

In the flowchart below, the parts in gray rectangles with a dashed border are commercially available components.

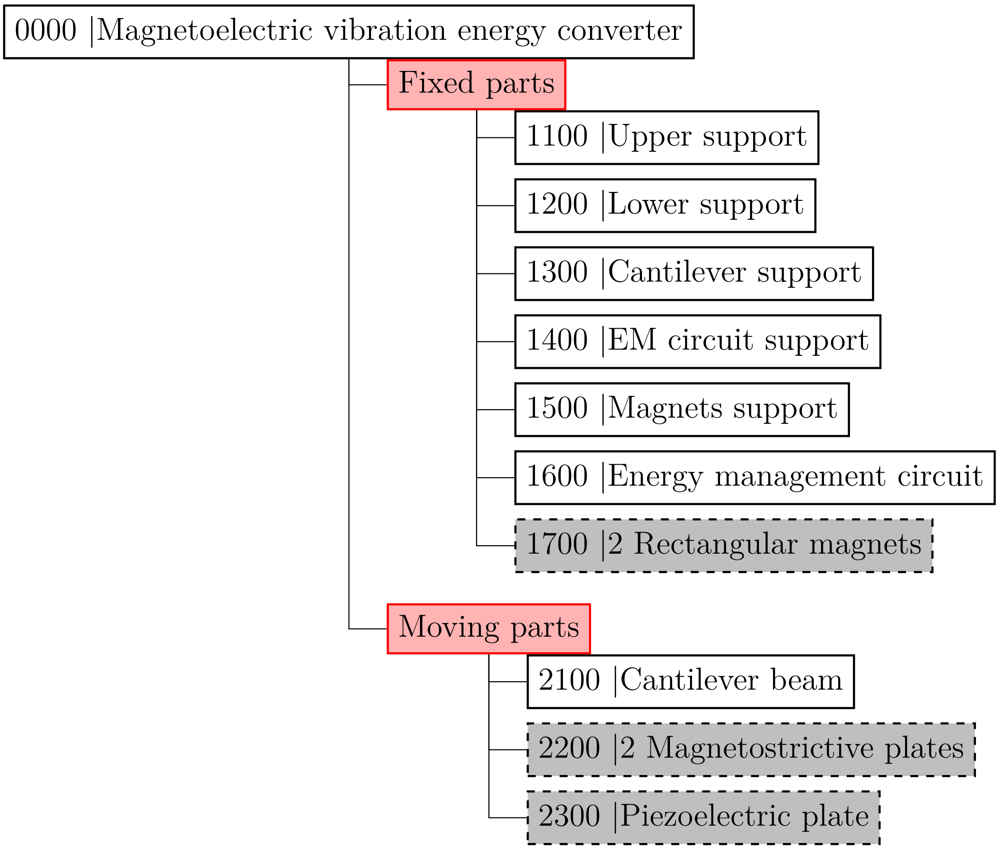

A.2 Cross section views

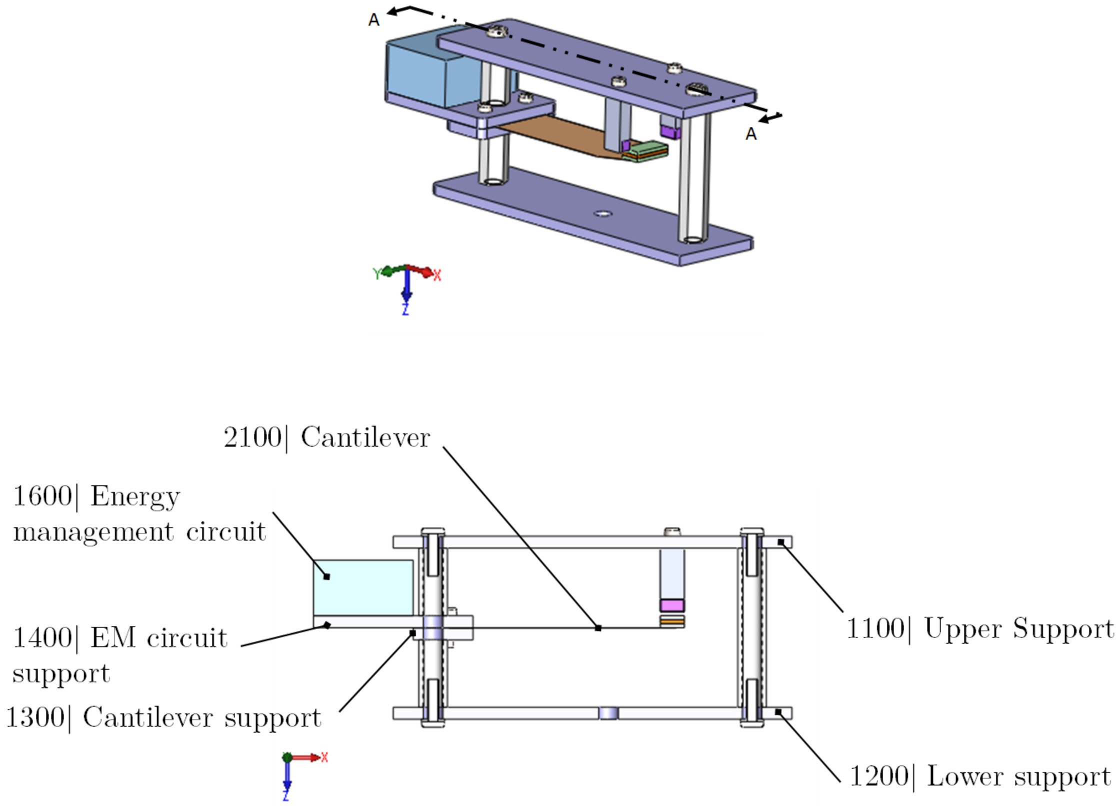

Figure A.1: A section view A-A of the designed converter

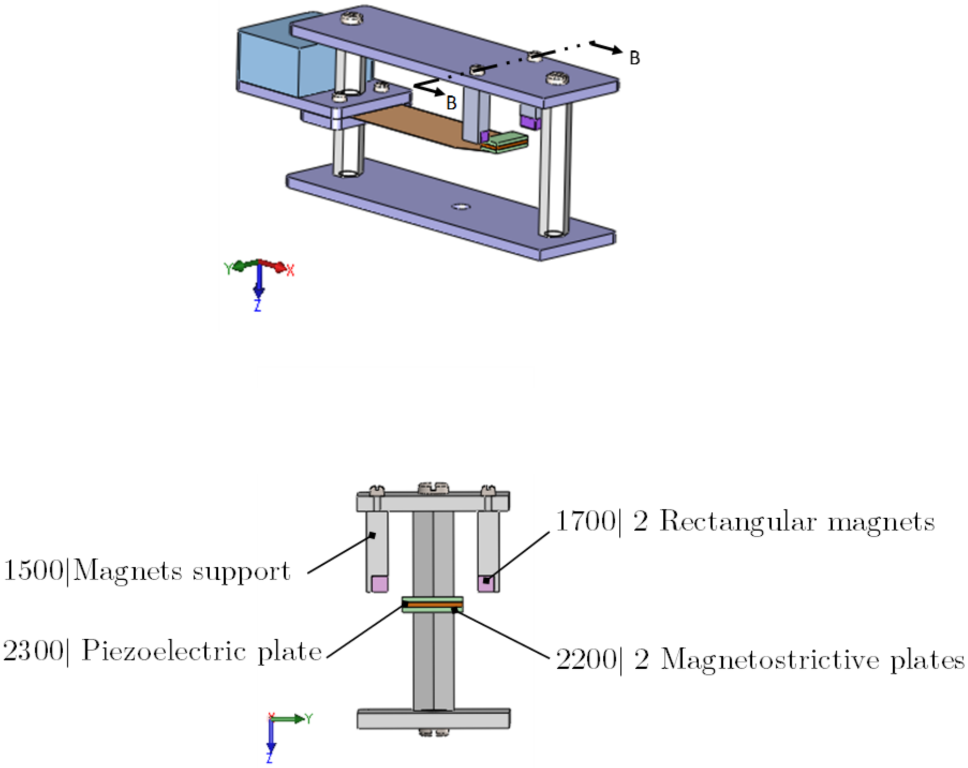

Figure A.2: A section view B-B of the designed converter

Table A.1: All used and designed components for the proposed converter

Ref.	Part	Material	Note	Qty.
2300	Piezoelectric plate	PMNT	SICCAS	1
2200	Magnetostrictive plate	Terfenol-D	Etrema Products, INC.	2
2100	Cantilever	Brass		1
1700	Rectangular magnet	NdFeB	B442 - K&J Magnetics, INC.	2
1600	Energy management circuit			1
1500	Magnets supprt	Aluminuim		2
1400	EM circuit support	Fiberglass		1
1300	Cantilever support	Fiberglass		1
1200	Lower support	Fiberglass		1
1100	Upper support	Fiberglass		1

B Lindstedt-Poincaré method

The governing equation of the 1 DOF is given by Equation 5.15.

$$\ddot{z} + 2\tau\psi\omega\dot{z} + \omega^2 z + \frac{\tau\omega^2}{m}[(\alpha_3+\beta_3)z^3 + (\alpha_2+\beta_2)z^2] = \tau P_0\omega^2 sin(\bar{\omega}t+\phi) \tag{6.15}$$

Equation 5.15 can be solved by Lindstedt-Poincaré method.
This method can be principally used for higher order approximates realizing better accuracy, but because in order to maintain a moderate complexity, we propose to limit the solution to the first approximation
First, two substitution are introduced:

- $\varphi = \bar{\omega}t$
- $d/dt = \bar{\omega}d/d\varphi$

which gives Equation B.1.

$$\bar{\omega}^2\ddot{z} + 2\tau\psi\omega\bar{\omega}\dot{z} + \omega^2 z + \frac{\tau\omega^2}{m}[\alpha_3 z^3 + \alpha_2 z^2] = \tau P_0\omega^2 cos(\varphi+\phi) \tag{B.1}$$

By introducing the detuning parameter Θ defined by

- $\bar{\omega}^2 = \omega^2(1+\tau\Theta)$

Equation B.1 can be represented as:

$$(1+\tau\Theta)\ddot{z} + 2\tau\psi\dot{z} + z + \frac{\tau}{m}[\alpha_3 z^3 + \alpha_2 z^2] = \tau P_0 cos(\varphi+\phi) \tag{B.2}$$

Equation B.2 can be solved in the form of:

$$z = z_0 + \tau z_1 + +\tau^2 z_1 + ... \tag{B.3}$$

Substituting Equation B.3 for Equation B.2 and equating the terms of the same order in τ, we obtain a set of equations as

$$\ddot{z}_0 + z_0 = 0 \tag{B.4}$$

$$\ddot{z}_1 + z_1 = -2\psi\dot{z}_0 - \Theta\ddot{z}_0 + P_0 cos(\varphi+\phi) - \frac{1}{m}[\alpha_3 z_0^3 + (\alpha_2+\beta_2)z_0^2] \tag{B.5}$$

By assuming the solution of the Equation B.5 in the form of Equation B.6:

$$z_0 = \gamma cos(\varphi) \tag{B.6}$$

Substituting Equation B.6 for Equation B.5 gives

$$\begin{aligned}\ddot{z}_1 + z_1 = (2\psi\gamma - P_0 sin(\phi))sin(\varphi) + (\Theta\gamma + P_0 cos(\phi))cos(\varphi) \\ -\frac{\alpha_3\gamma^3}{4m}cos(3\varphi) - 3\frac{\alpha_3\gamma^3}{4m}cos(\varphi) - \frac{\alpha_2\gamma^2}{2m} - \frac{\alpha_2\gamma^2}{2m}cos(2\varphi)\end{aligned} \tag{B.1}$$

In Equation B.1, the terms with $sin(\varphi)$ and $cos(\varphi)$ must be zero which leads to Equation B.8 and Equation B.9 as follows:

$$2\psi\gamma - P_0 sin(\phi) = 0 \tag{B.8}$$

$$\Theta\gamma + P_0 cos(\phi) - 3\frac{\alpha_3\gamma^3}{4m} = 0 \tag{B.9}$$

In the case of primary resonance $\Theta = 0$, and eliminating ϕ, we obtain Equation B.10:

$$(2\psi\gamma)^2 + [3\frac{\alpha_3\gamma^3}{4m}]^2 = P_0 \tag{B.10}$$

By solving Equation B.10 for γ and solving Equation B.1 for z_1, Equation B.11 is obtained:

$$z_1 = \frac{(\alpha_2 + \beta_2)\gamma^2}{6m}cos(2\varphi) + \frac{\alpha_3\gamma^3}{32m}cos(3\varphi) \tag{B.11}$$

Then, the first approximate solution to Equation (B.1) can be given by Equation (B.12):

$$z(t) = z_0 + \gamma z_1 = \gamma cos(\bar{\omega}) + \frac{\alpha_2 + \gamma^2}{6m\omega^2}cos(2\bar{\omega}) + \frac{\alpha_3\gamma^3}{32m\omega^2}cos(3\bar{\omega}) \tag{B.12}$$

C Assessment of fatigue behaviour of piezo ceramics

Fatigue investigation is one of the fundamental parts of mechanical engineering design. Applying repeatedly applied stress to materials or structural components leads in general to damage and fracture [154]. Some materials, such as steel, has an infinite fatigue life when subjected to a repeatedly applied stress below their endurance limit. Other materials, such as piezo ceramics, do not have such behaviour and they are characterized by a limited fatigue life depending on the applied stress and the applied number of cycles.

The aim of this section is to investigate fatigue behaviour of piezoelectric materials used in vibration energy harvesting. To that end, fatigue analysis is carried out on a piezo ceramic plate when used in magnetoelectric converters and when used in piezoelectric converters as a cantilever beam.

C.1 Methodology for fatigue assessment using finite element analysis

Fatigue of materials is usually studied by exposing the sample to cycling stresses. However, experimental investigations are generally expensive since many test specimens are necessary. Recently, finite element analysis has been employed to investigate the fatigue behaviour of materials. In this case, the main challenges are the selection of a suitable fatigue model and finding the appropriate material data.

C.1.1 Fatigue Model

Figure C.1 presents the flowchart for the selection of the fatigue model type in Comsol Multiphysics. Since the load type in vibration converters are generally characterized by non-harmonic cycles, the appropriate model to simulate the fatigue behaviour in the piezo ceramic layer is the cumulative damage model. The cumulative model presents an advanced evaluation technique to quantify the stress response in a structure when applying random loads. In this case, a variety of stresses with different magnitude will be introduced into the structure. Contrarily to other fatigue models, fatigue evaluation using the cumulative damage feature is based on the conversion of a random load into a stress range distribution. In this model, the load history is defined with the Rainflow counting algorithm, and the damage is processed using the Palmgren-Miner linear damage rule [156].

C.1.2 Material data

The S-N curve, also known as Wohler curve, is needed for the Palmgren-Miner linear damage summation. The S-N curve presents the material fatigue performance. It

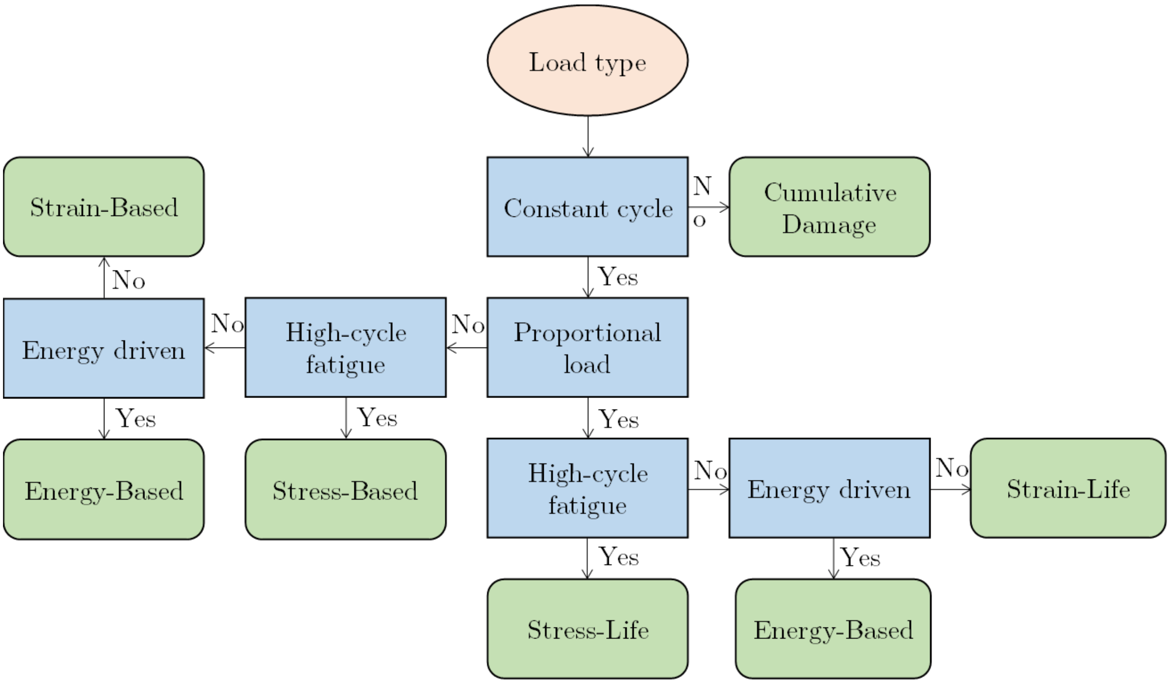

Figure C.1: Flowchart of the selection of the fatigue model type in Comsol Multiphysics [155]

relates the stress amplitude and the life time of the material which is generally given in number of cycles. To obtain the S-N curve of a material, different experimental tests are needed by varying the alternating stress (σ_a) for given mean stress (σ_m), temperature and frequency. σ_a and σ_m are given in Equation C.1 and Equation C.2, respectively.

$$\sigma_a = \frac{\sigma_{max} - \sigma_{min}}{2} \tag{C.1}$$

$$\sigma_m = \frac{\sigma_{max} + \sigma_{min}}{2} \tag{C.2}$$

Where σ_{max} and σ_{min} are the maximum and the minimum stress, respectively. In addition, the S-N curve is characterized by the stress ratio (R) value is accounted for. R presents the ratio between the minimum and maximum stress in the load cycle (Equation C.3).

$$R = \frac{\sigma_{min}}{\sigma_{max}} \tag{C.3}$$

Life time of a material is shorter in fatigue tests performed with a tensile mean stress comparing to compressive mean stress. More generally, with decreasing mean stress (or the stress ratio), the fatigue life increases. Figure C.2 presents the effect of different mean stresses on the S-N curve. The loading applied to a piezo ceramic layer used in piezoelectric vibration converters, which is in the form of a cantilever beam deflected at the free end, is characterized by zero mean stress while the loading in case of a piezo

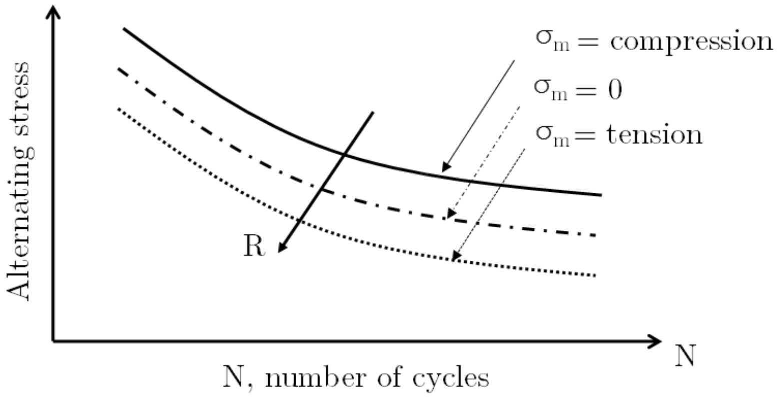

Figure C.2: Effect of different mean stresses (or the stress ration) on the S-N curve

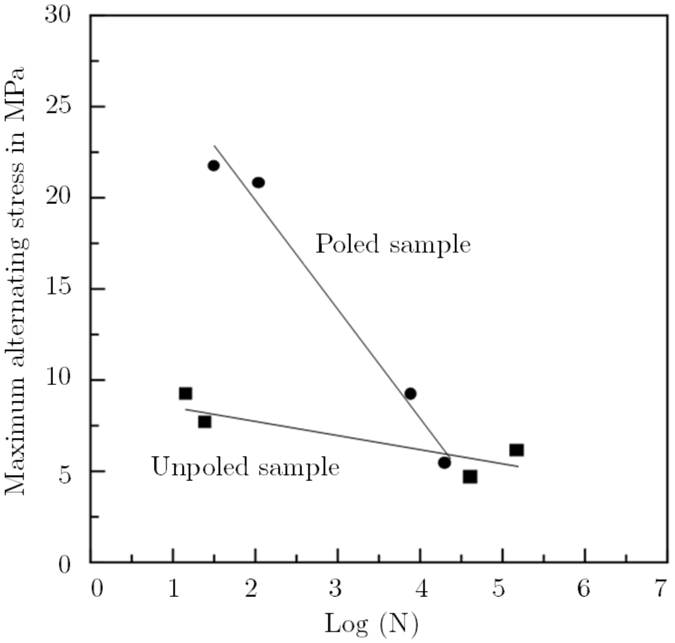

Figure C.3: S-N curve for poled and unpoled PZT [157]

ceramic plate used in ME laminate composites can be tensile or compressive mean stress depending on the direction of the applied magnetic field.

Since the aim of this section is to compare the fatigue behaviour of a piezoelectric layer used in two different types of vibration transducers and not to predict their fatigue life time, the same stress versus life time plot will be employed in the proposed fatigue analysis in Comsol Multiphysics. Figure C.3 presents the S-N curve of poled and unpoled PZT samples. Data of poled PZT sample be employed in the finite element analysis.

C.2 Finite element model

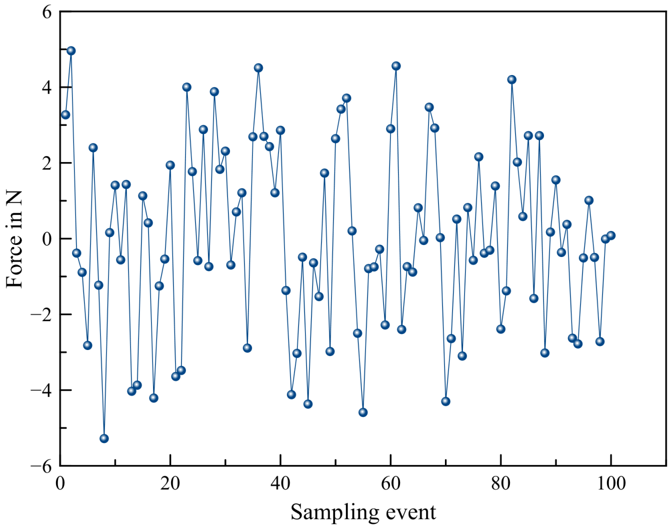

Figure C.4: Applied loading cycle

The piezo ceramic plate used in the finite element investigation has a length of 12 mm, a width of 6 mm and a thickness of 1 mm. Two different cases are investigated; the first is when the plate is used as a cantilever beam and the second when it is bonded to two Terfenol-d layers. In the first scenario, the loading consists of a random excitation vibration applied to the free end of the cantilever while in the second one, the same random excitation will be applied as a compression loading to the piezo ceramic plate. Figure C.4 presents the loading applied to the sample.
The stress versus life time plot of the material is modified in order to be implemented in Comsol Multiphysiscs since the fatigue data have to be specified using the alternating stress amplitude rather than the maximum stress as required by the cumulative damage fatigue feature. Equation C.4 presents the used relation to convert the maximum stress σ_{max} to the alternating stress amplitude σ_a in the two cases.

$$\sigma_a = \frac{\sigma_{max}(1 - R)}{2} \tag{C.4}$$

The applied load is shown in Figure C.4. It consists of one loading cycle formed by 100 non-proportional events.

C.3 Results and discussion

Stresses on the profiles where the plate is fixed in the two cases are more critical because highest stresses are found there. These profiles are shown in Figure C.5. The variation of the Fatigue Usage Factor (FUF) along these profiles are given in Figure C.6 for the two cases. In the cumulative damage analysis, FUF below 1 indicates that the structure will hold while values above 1 indicate that it will fail. As shown in Figure C.6, the maximum FUFs are located at the edges of the profiles and they are equal to 0.19 and 0.014 respectively.

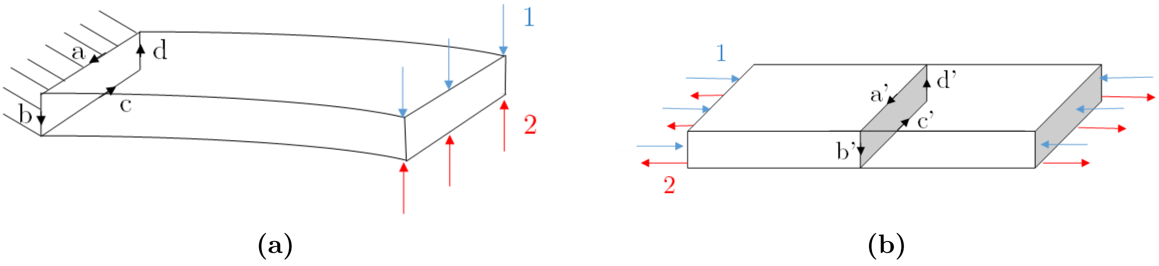

(a) **(b)**

Figure C.5: Profiles where the plates are fixed (a) PE converters (b) ME converters. 1 et 2 indicate the load cases

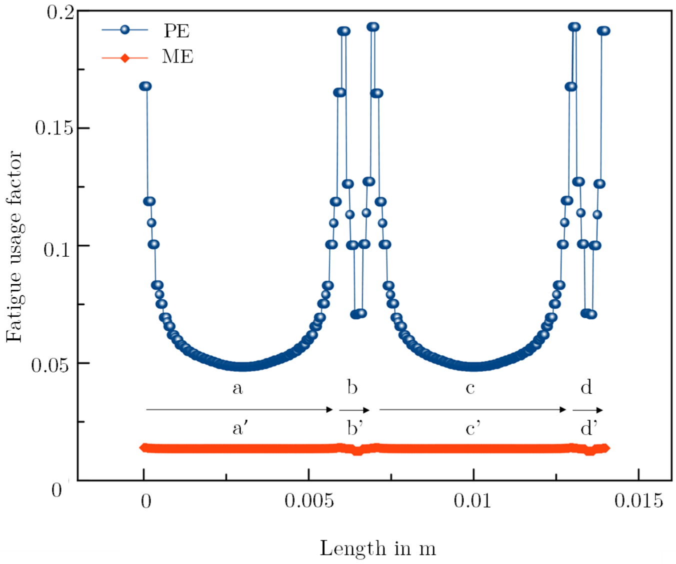

Figure C.6: Fatigue usage factor along the profile where the plate is fixed for the two cases

Since the relation between the damage and the number of cycles in the Palmgren-Miner rule is linear [158], the plate will fail when the number of applied cycles increases with a factor $1/0.19 \simeq 5$ when used as a cantilever beam while in case when used in magnetoelectric transducer, it will fail when increasing the number of cycles with a factor of $1/0.014 \simeq 71$.

In Figure C.7 (a) the load distribution in the point of the highest FUF is shown following the rainflow theory for case 1. The mean stress and the stress amplitude are in the range of -2 MPa to 2 MPa and 0 to 5 MPa, respectively. It is remarked the existence of possible damaging stress cycle having mean stresses around 0, 2 MPa and 4 MPa stress amplitude.

In order to visualize which cycles are most damaging, the relative fatigue usage factor following the Palmgren-Miner damage rule in the same location is investigated and it is presented in Figure C.7 (b). It shows how much of the total damage is done by a specific cycle. Dark blue areas can be considered as non-damaging cycles which are in this case all cycles having a stress amplitude below 2 MPa, while 8 % of the fatigue damage comes from one single event (Mean stress = 0, Stress amplitude = 4 MPa).

Figure C.8 (a) and (b) presents respectively the cycle counting and the relative fatigue usage in the point of the highest usage factor for case 2. The mean stress and the stress amplitude are in the range of -2×10^4 Pa to 6×10^4 Pa and 0 to 7×10^4 Pa, respectively.

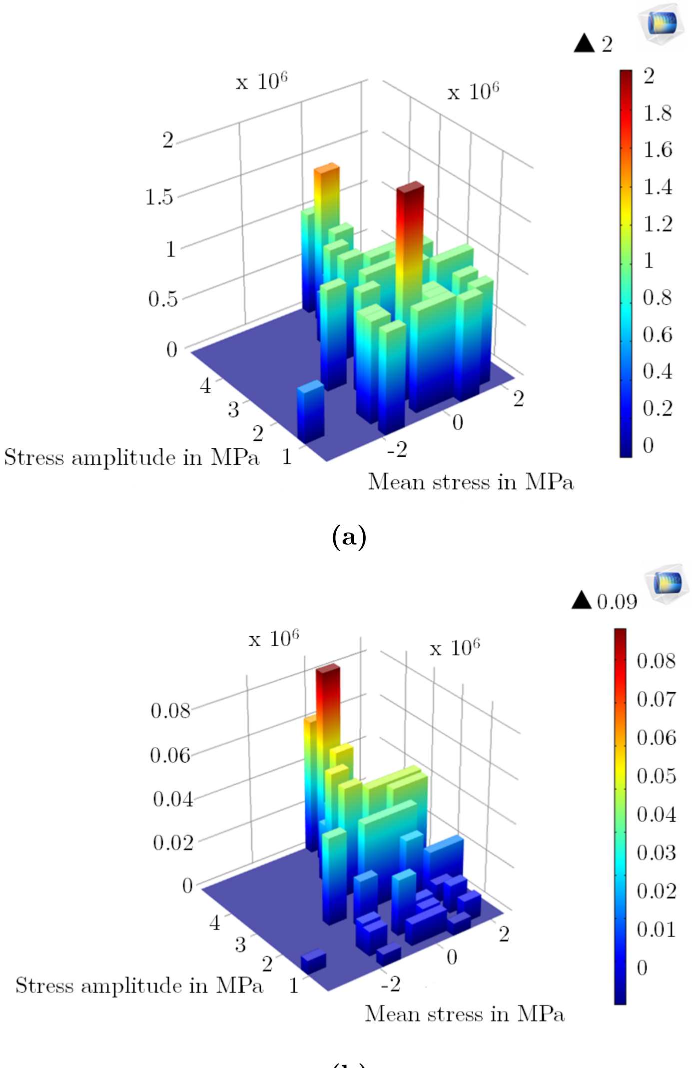

(a)

(b)

Figure C.7: (a) Counted stress cycles following the rainflow theory (b) Relative fatigue usage following the Palmgren-Miner damage rule, in the point of the highest usage factor in case 1

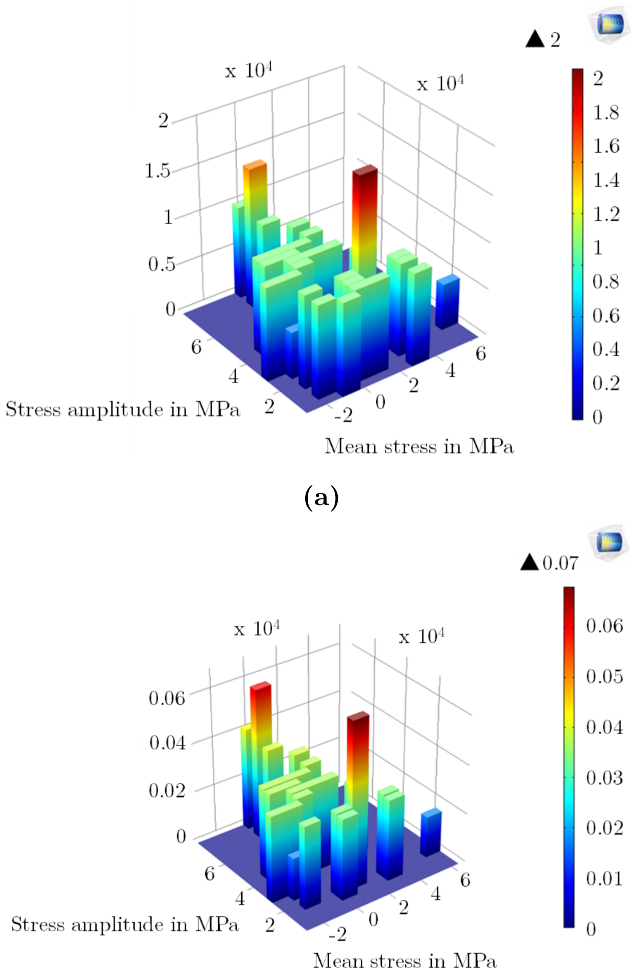

(a)

(b)

Figure C.8: (a) Counted stress cycles following the rainflow theory (b) Relative fatigue usage following the Palmgren-Miner damage rule, in the point of the highest usage factor in case 2

Figure C.8 (a) shows the presence of several low mean stress cycles (around 0), which do not have very high stress amplitudes (below 5$\times 10^4$ MPa) with the existence of several stresses having high mean values and some others having high stress amplitudes, which can be considered as a source of the expected damage. In Figure C.8 (b), it is shown that 6 % of the fatigue damage comes from two single events in the load history (Mean stress = 2$\times 10^4$ MPa, Stress amplitude = 2$\times 10^4$ MPa) and (Mean stress = 0, Stress amplitude =7 $\times 10^4$ MPa).

It should be noticed that the assessment of the fatigue behaviour presented here is an attempt to evaluate the use of piezo ceramics in energy harvesting. However, reported results in this section have to be proved and evaluated with experimental investigations which are the fundamental part in the fatigue analysis.

Bibliography

1. Hadas, Zdenek et al.: ‘Virtual prototypes of energy harvesting systems for industrial applications’. *Mechanical Systems and Signal Processing* (2018), vol. 110: pp. 152–164.
2. Rastegar, Jahangir et al.: *Energy Harvesting for Low-power Autonomous Devices and Systems.* 2017.
3. Chalasani, Sravanthi et al.: ‘A survey of energy harvesting sources for embedded systems’. *Southeastcon, 2008. IEEE.* 2008: pp. 442–447.
4. Jayakumar, Hrishikesh et al.: ‘Powering the internet of things’. *Proceedings of the 2014 international symposium on Low power electronics and design.* 2014: pp. 375–380.
5. Beeby, S.P. et al.: ‘A micro electromagnetic generator for vibration energy harvesting’. *J. Micromech. Microeng.* (2007), vol. 17(7): p. 1257.
6. Khaligh, A. et al.: ‘Kinetic energy harvesting using piezoelectric and electromagnetic technologies-state of the art’. *IEEE Trans. Ind. Electron.* (2010), vol. 57(3): pp. 850–860.
7. Friswell, Michael I et al.: ‘Non-linear piezoelectric vibration energy harvesting from a vertical cantilever beam with tip mass’. *Journal of Intelligent Material Systems and Structures* (2012), vol. 23(13): pp. 1505–1521.
8. Naifar, Slim et al.: ‘A smart energy harvester for axial-force measurements in vibrating environments’. *Sensors Applications Symposium (SAS), 2018 IEEE.* 2018: pp. 1–5.
9. Naifar, S. et al.: ‘Response analysis of a nonlinear magnetoelectric energy harvester under harmonic excitation’. *Eur. Phys. J. Spec. Top.* (2015), vol. 224(14-15): pp. 2897–2907.
10. Tvedt, Lars Geir Whist et al.: ‘Nonlinear behavior of an electrostatic energy harvester under wide-and narrowband excitation’. *Journal of Microelectromechanical systems* (2010), vol. 19(2): pp. 305–316.
11. Mori, Takao et al.: ‘Materials for energy harvesting: At the forefront of a new wave’. *MRS Bulletin* (2018), vol. 43(3): pp. 176–180.
12. Radousky, H.B. et al.: ‘Energy harvesting: an integrated view of materials, devices and applications’. *Nanotechnology* (2012), vol. 23(50): p. 502001.
13. Clark, A.E. et al.: ‘High temperature magnetostriction of TbFe2 and Tb. 27 Dy.73Fe2’. *IEEE. T. Magn.* (1985), vol. 21(5): pp. 1945–1947.

14. Chu, Zhaoqiang et al.: ‘Dual-stimulus magnetoelectric energy harvesting’. *MRS Bulletin* (2018), vol. 43(3): pp. 199–205.
15. Martins, P. et al.: ‘Polymer-based magnetoelectric materials’. *Adv. Funct. Mater.* (2013), vol. 23(27): pp. 3371–3385.
16. Bichurin, M. et al.: *Modeling of Magnetoelectric Effects in Composites.* Springer, 2014.
17. O’Handley, R.C. et al.: ‘Improved Wireless, Transcutaneous Power Transmission for In Vivo Applications’. *IEEE Sensors J.* (2008), vol. 8(1): pp. 57–62.
18. Landau, L.D et al.: *Electrodynamics of continuous media.* Pergamon Press, 1960.
19. Fiebig, M.: ‘Review: Revival of the magnetoelectric effect’. *J. Phys. D* (2005), vol. 38: R123.
20. Park, C-S. et al.: ‘Quantitative understanding of the elastic coupling in magnetoelectric laminate composites through the nonlinear polarization–magnetic (P–H) response’. *Smart Mater. Struct.* (2011), vol. 20(8): p. 082001.
21. Ortega, N. et al.: ‘Multifunctional magnetoelectric materials for device applications’. *J. Phys. Condens. Matter* (2015), vol. 27(50): p. 504002.
22. Kimura, T. et al.: ‘Magnetic control of ferroelectric polarization’. *Nature* (2003), vol. 426(6962): pp. 55–58.
23. Dzyaloshinskii, I. E.: ‘On the magneto-electrical effect in antiferromagnets’. *Soviet Physics Jetp-Ussr* (1960), vol. 10(3): pp. 628–629.
24. Astrov, D.N.: ‘The magnetoelectric effect in antiferromagnetics’. *Sov. Phys. JETP* (1960), vol. 11(3): pp. 708–709.
25. Ascher, E. et al.: ‘Some rties of ferromagnetoelectric Nickel-Iodine Boracite, Ni3B7O13I’. *J. Appl. Phys.* (1966), vol. 37(3): pp. 1404–1405.
26. Santoro, R.P. et al.: ‘Magnetic properties of LiCoPO4 and LiNiPO4’. *J. Phys. Chem. Solids* (1966), vol. 27(6-7): pp. 1192–1193.
27. Roy, S. et al.: ‘Investigations on Flexible Multiferroic Composites’. *Proc. International Workshop on Mesoscopic, Nanoscopic and Macroscopic Materials.* Vol. 1063. 1. 2008: pp. 276–289.
28. Martin, L.W.: ‘Engineering functionality in the multiferroic BiFeO3–controlling chemistry to enable advanced applications’. *Dalton Trans.* (2010), vol. 39(45): pp. 10813–10826.
29. Shin, K.H. et al.: ‘Preparation and properties of elastically coupled electromagnetic elements with a bonding structure’. *IEEE Trans. Magn.* (1998), vol. 34(4): pp. 1324–1326.

30. Yang, F. et al.: ‘Resonant magnetoelectric response of magnetostrictive/piezoelectric laminate composite in consideration of losses’. *Sens. Actuators, A* (2008), vol. 141(1): pp. 129–135.

31. Benatar, J.G.: ‘FEM implementations of magnetostrictive-based applications’. PhD thesis. 2005.

32. Chikazumi, S. et al.: *Physics of ferromagnetism 2e.* 94. Elsevier, 2009.

33. Tumanski, S.: *Handbook of magnetic measurements.* CRC Press, 2011.

34. Palneedi, H. et al.: ‘Status and Perspectives of Multiferroic Magnetoelectric Composite Materials and Applications’. *Actuators* (2016), vol. 5(1): p. 9.

35. Mayergoyz, I.D. et al.: *Handbook of giant magnetostrictive materials.* 1999.

36. Calkins, Frederick T et al.: ‘Overview of magnetostrictive sensor technology’. *Journal of Intelligent Material Systems and Structures* (2007), vol. 18(10): pp. 1057–1066.

37. Dapino, M.J.: ‘On magnetostrictive materials and their use in smart material transducer’. *Struct. Eng. Mech. J.* (2002), vol. 17: pp. 1–28.

38. Dapino, Marcelo Jorge: ‘Nonlinear and hysteretic magnetomechanical model for magnetostrictive transducers’. (1999), vol.

39. Smith, R.C. et al.: ‘Free energy model for hysteresis in magnetostrictive transducers’. *J. Appl. Phys.* (2003), vol. 93(1): pp. 458–466.

40. Olabi, A-G. et al.: ‘Design and application of magnetostrictive materials’. *Materials and Design* (2008), vol. 29(2): pp. 469–483.

41. Malyugin, DV: ‘On the theory of Wiedemann effects’. *Journal of magnetism and magnetic materials* (1991), vol. 97(1): pp. 193–197.

42. De Lacheisserie, E.D.T.: *Magnetostriction: theory and applications of magnetoelasticity.* CRC Press, 1993.

43. Restorff, J. B. et al.: ‘Modern magnetostrictive materials’. *J. Acoust. Soc. Am.* (2001), vol. 109(5): pp. 2434–2434.

44. Clark, AE et al.: ‘Magnetostriction “jumps” in twinned Tb0.3Dy0.7Fe1.9’. *J. Appl. Phys.* (1988), vol. 63(8): pp. 3910–3912.

45. Dapino, M. J. et al.: ‘Statistical analysis of Terfenol-D material properties’. *J. Intell. Mater. Syst. Struct.* (2006), vol. 17(7): pp. 256–267.

46. Gautschi, G.: *Piezoelectric Sensorics: force, strain, pressure, acceleration and acoustic emission sensors, materials and amplifiers.* Springer, 2002.

47. *Terfenol-D physical properties.* http://www.etrema.com/terfenol-d/. Accessed 14 03 2016.

48. *Galfenol physical properties.* http://www.etrema.com/galfenol/. Accessed 14 03 2016.

49. Engdahl, G.: *Handbook of giant magnetostrictive materials*. Elsevier, 2000.
50. Tichy, J. et al.: *Fundamentals of piezoelectric sensorics*. Springer, 2010.
51. Heywang, W. et al.: *Piezoelectricity: evolution and future of a technology*. Springer Science and Business Media, 2008.
52. Fleming, A. J. et al.: *Design, modeling and control of nanopositioning systems*. Springer, 2014.
53. *Physical and Piezoelectric Properties of APC Materials*. http://www.americanpiezo. com/apc-materials/physical-piezoelectric-properties/. Accessed 06 04 2016.
54. *Properties of Barium Titanate ($BaTiO_3$)*. https://www.americanpiezo.com/ table/apc-materials/ single-crystals-non-pzt-materials. Accessed 06 04 2016.
55. *PMNT Piezoelectric Crystal, Shanghai SICCAS High Technology Corporation*. http:// www.siccas.com/. Accessed: 12 10 2016. 2016.
56. Brook, R. J.: *Concise encyclopedia of advanced ceramic materials*. Elsevier, 2012.
57. Islam, Rashed Adnan et al.: ‘Effect of gradient composite structure in cofired bilayer composites of Pb (Zr0. 56Ti0. 44) O3–Ni0. 6Zn0. 2Cu0. 2Fe2O4 system on magnetoelectric coefficient’. *Journal of materials science* (2008), vol. 43(18): pp. 6337–6343.
58. Islam, R. A. et al.: ‘Magnetoelectric properties of core-shell particulate nanocomposites’. *J. Appl. Phys.* (2008), vol. 104(10): p. 104111.
59. Lam, K. H. et al.: ‘Frequency response of magnetoelectric 1–3-type composites’. *J. Appl. Phys.* (2010), vol. 107(9): p. 093901.
60. Ma, J. et al.: ‘Magnetoelectric properties of composites of single Pb (Zr, Ti) O3 rods and Terfenol-D/Epoxy with a single-period of 1-3-Type Structure’. *Adv. Mater.* (2007), vol. 19(18): pp. 2571–2573.
61. Wang, Y. et al.: ‘An extremely low equivalent magnetic noise magnetoelectric sensor’. *Adv. Mater.* (2011), vol. 23(35): pp. 4111–4114.
62. Islam, R. A. et al.: ‘Giant magnetoelectric effect in sintered multilayered composite structures’. *J. Appl. Phys.* (2008), vol. 104(4): p. 044103.
63. Gillette, S. M. et al.: ‘Effects of intrinsic magnetostriction on tube-topology magnetoelectric sensors with high magnetic field sensitivity’. *J. Appl. Phys.* (2014), vol. 115(17): p. 17C734.
64. Bichurin, Mirza et al.: *Magnetoelectricity in composites*. CRC Press, 2011.
65. Nan, Ce-Wen et al.: ‘Multiferroic magnetoelectric composites: Historical perspective, status, and future directions’. *Journal of Applied Physics* (2008), vol. 103(3): p. 1.
66. Xu, Ying et al.: ‘Fabrication and magnetoelectric effect of 1–3 type composites with microscale (K, Na) NbO3-based Pb-free piezoceramic pillars embedded in CoFe2O4-epoxy matrix’. *Ceramics International* (2012), vol. 38: S425–S429.

67. Ryu, J. et al.: 'Effect of the Magnetostrictive Layer on Magnetoelectric Properties in Lead Zirconate Titanate/Terfenol-D Laminate Composites'. *J. Am. Ceram. Soc.* (2001), vol. 84(12): pp. 2905–2908.

68. Wang, Y. et al.: 'Enhanced magnetoelectric effect in longitudinal-transverse mode Terfenol-D/ Pb (Mg1/3 Nb2/3) O3–Pb Ti O3 laminate composites with optimal crystal cut'. *J. Appl. Phys.* (2008), vol. 103(12): p. 124511.

69. Wang, Z. et al.: 'Enhancement of capacitive type magnetoimpedance effect in ring-type magnetoelectric transducers vibrator via size-dependent resonance frequency'. *Sens. Actuators, A* (2016), vol. 247: pp. 234–238.

70. Nan, Ce Wen et al.: 'Calculations of giant magnetoelectric effects in ferroic composites of rare-earth–iron alloys and ferroelectric polymers'. *Physical Review B* (2001), vol. 63(14): p. 144415.

71. Nan, Ce-Wen et al.: 'Influence of interfacial bonding on giant magnetoelectric response of multiferroic laminated composites of Tb 1- x Dy x Fe 2 and PbZr x Ti 1- x O 3'. *Applied Physics Letters* (2003), vol. 83(21): pp. 4366–4368.

72. Dong, Shuxiang et al.: 'Giant magneto-electric effect in laminate composites'. *IEEE Transactions on Ultrasonics, Ferroelectrics, and frequency control* (2003), vol. 50(10): pp. 1236–1239.

73. Dong, Shuxiang et al.: 'Ultrahigh magnetic field sensitivity in laminates of TERFENOL-D and Pb (Mg 1/3 Nb 2/3) O 3–PbTiO 3 crystals'. *Applied Physics Letters* (2003), vol. 83(11): pp. 2265–2267.

74. Dong, Shuxiang et al.: 'Longitudinal and transverse magnetoelectric voltage coefficients of magnetostrictive/piezoelectric laminate composite: Theory'. *IEEE transactions on ultrasonics, ferroelectrics, and frequency control* (2003), vol. 50(10): pp. 1253–1261.

75. Sunithamani, S et al.: 'Experimental study and analysis of unimorph piezoelectric energy harvester with different substrate thickness and different proof mass shapes'. *Microsystem Technologies* (2017), vol. 23(7): pp. 2421–2430.

76. Gao, Xiaotong et al.: 'Vibration energy harvesting using piezoelectric unimorph cantilevers with unequal piezoelectric and nonpiezoelectric lengths'. *Applied physics letters* (2010), vol. 97(23): p. 233503.

77. Xu, J et al.: 'Multi-directional energy harvesting by piezoelectric cantilever-pendulum with internal resonance'. *Applied Physics Letters* (2015), vol. 107(21): p. 213902.

78. Aboulfotoh, Noha et al.: 'On developing an optimal design procedure for a bimorph piezoelectric cantilever energy harvester under a predefined volume'. *Mechanical Systems and Signal Processing* (2018), vol. 106: pp. 1–12.

79. Roundy, S. et al.: 'Improving power output for vibration-based energy scavengers'. *IEEE Pervasive Comput.* (2005), vol. 4(1): pp. 28–36.

80. Sodano, H. A. et al.: ‘Estimation of electric charge output for piezoelectric energy harvesting’. *Strain* (2004), vol. 40(2): pp. 49–58.

81. Kundu, Sushanta et al.: ‘Modeling and simulation of a piezoelectric vibration energy harvester’. *Procedia Engineering* (2016), vol. 144: pp. 568–575.

82. Zhu, Dibin et al.: ‘A bimorph multi-layer piezoelectric vibration energy harvester’. *PowerMEMS* (2010), vol.

83. Dai, X. et al.: ‘Modeling, characterization and fabrication of vibration energy harvester using Terfenol-D/PZT/Terfenol-D composite transducer’. *Sens. Actuators, A* (2009), vol. 156(2): pp. 350–358.

84. Zhang, Z. et al.: ‘An improved magnetoelectric vibration energy harvester for wireless sensors’. *IEEE 14th International Conference on Communication Technology (ICCT).* 2012: pp. 589–593.

85. Dai, X. et al.: ‘Energy harvesting from mechanical vibrations using multiple magnetostrictive/piezoelectric composite transducers’. *Sens. Actuators, A* (2011), vol. 166(1): pp. 94–101.

86. Bai, X. et al.: ‘Multi-modal vibration energy harvesting utilizing spiral cantilever with magnetic coupling’. *Sensors and Actuators A: Physical* (2014), vol. 209: pp. 78–86.

87. Li, M. et al.: ‘A magnetostrictive/piezoelectric laminate transducer based vibration energy harvester with resonance frequency tunability’. *Sensors.* 2011: pp. 1768–1771.

88. Li, M. et al.: ‘A resonant frequency self-tunable rotation energy harvester based on magnetoelectric transducer’. *Sens. Actuators, A* (2013), vol. 194: pp. 16–24.

89. Qiu, J. et al.: ‘A vibration energy harvester using magnet/piezoelectric composite transducer’. *J. Appl. Phys.* (2014), vol. 115(17): 17E522.

90. Yang, J. et al.: ‘Design and analysis of a 2D broadband vibration energy harvester for wireless sensors’. *Sens. Actuators, A* (2014), vol. 205: pp. 47–52.

91. Moss, S.D. et al.: ‘Wideband vibro-impacting vibration energy harvesting using magnetoelectric transduction’. *J. Intell. Mater. Syst. Struct.* (2012), vol. 24(11): pp. 1313–1323.

92. Ju, S. et al.: ‘A low frequency vibration energy harvester using magnetoelectric laminate composite’. *Smart Mater. Struct.* (2013), vol. 22(11): p. 115037.

93. Zhu, Y. et al.: ‘A magnetoelectric generator for energy harvesting from the vibration of magnetic levitation’. *IEEE Trans. Magn.* (2012), vol. 48(11): pp. 3344–3347.

94. Naifar, S. et al.: ‘Design of a vibration energy harvester by twin lateral magnetoelectric transducers’. *Instrumentation and Measurement Technology Conference (I2MTC) Proc.* 2014: pp. 1157–1162.

95. He, Wei et al.: ‘Piezoelectric energy harvester scavenging AC magnetic field energy from electric power lines’. *Sensors and Actuators A: Physical* (2013), vol. 193: pp. 59–68.

96. He, Wei et al.: ‘Energy harvesting from electric power lines employing the Halbach arrays’. *Review of Scientific Instruments* (2013), vol. 84(10): p. 105004.

97. He, W. et al.: ‘A Noncontact Magnetoelectric Generator for Energy Harvesting From Power Lines’. *IEEE Trans. Magn.* (2014), vol. 50(11): pp. 1–4.

98. He, W. et al.: ‘Energy harvesting from two-wire power cords using magnetoelectric transduction’. *IEEE Trans. Magn.* (2014), vol. 50(8): pp. 1–5.

99. Dai, X.: ‘An vibration energy harvester with broadband and frequency-doubling characteristics based on rotary pendulums’. *Sensor Actuat A-Phys.* (2016), vol. 241: pp. 161–168.

100. Spreemann, D et al.: ‘Non-resonant vibration conversion’. *Journal of Micromechanics and Microengineering* (2006), vol. 16(9): S169.

101. Ma, Tian-Wei et al.: ‘A novel parametrically excited non-linear energy harvester’. *Mechanical Systems and Signal Processing* (2012), vol. 28: pp. 323–332.

102. Malaji, PV et al.: ‘Analysis of energy harvesting from multiple pendulums with and without mechanical coupling’. *The European Physical Journal Special Topics* (2015), vol. 224(14-15): pp. 2823–2838.

103. Ylli, K et al.: ‘Investigation of pendulum structures for rotational energy harvesting from human motion’. *Journal of Physics: Conference Series.* Vol. 660. 1. IOP Publishing. 2015: p. 012053.

104. Liang, Changwei et al.: ‘Broadband pendulum energy harvester’. *Smart Materials and Structures* (2016), vol. 25(9): p. 095042.

105. Cottone, Francesco et al.: ‘Nonlinear energy harvesting’. *Physical Review Letters* (2009), vol. 102(8): p. 080601.

106. Wang, Yu-Jen et al.: ‘System design of a weighted-pendulum-type electromagnetic generator for harvesting energy from a rotating wheel’. *IEEE/ASME Transactions on Mechatronics* (2013), vol. 18(2): pp. 754–763.

107. Kadjie, Arnaud Notué et al.: ‘Effects of springs on a pendulum electromechanical energy harvester’. *Theoretical and Applied Mechanics Letters* (2014), vol. 4(6).

108. Jia, Yu et al.: ‘Parametric resonance for vibration energy harvesting with design techniques to passively reduce the initiation threshold amplitude’. *Smart Materials and Structures* (2014), vol. 23(6): p. 065011.

109. Shenck, N. S.: ‘A demonstration of useful electric energy generation from piezoceramics in a shoe’. PhD thesis. Massachusetts Institute of Technology, 1999.

110. Sodano, H. et al.: ‘Electric power generation using piezoelectric devices’. *Proceedings of 13th International Conference on Adaptive Structures and Technologies.* 2002: pp. 7–9.

111. White, N. M. et al.: ‘A novel thick-film piezoelectric micro-generator’. *Smart Mater. Struct.* (2001), vol. 10(4): p. 850.

112. Khaligh, A. et al.: ‘Hybrid energy harvesting topology for human-powered mobile electronics’. *Industrial Electronics, IECON, 34th Annual Conference of IEEE.* 2008: pp. 448–453.

113. Morimoto, K. et al.: ‘High-efficiency piezoelectric energy harvesters of c-axis-oriented epitaxial PZT films transferred onto stainless steel cantilevers’. *Sensor Actuat A-Phys.* (2010), vol. 163(1): pp. 428–432.

114. Durou, H. et al.: ‘Micromachined bulk PZT piezoelectric vibration harvester to improve effectiveness over low amplitude and low frequency vibrations’. *Proceedings of Power MEMS. Leuven, Belgium* (2010), vol.: pp. 27–30.

115. Defosseux, M. et al.: ‘Highly efficient piezoelectric micro harvester for low level of acceleration fabricated with a CMOS compatible process’. *Sensor Actuat A-Phys.* (2012), vol. 188: pp. 489–494.

116. Xu, R. et al.: ‘Screen printed PZT/PZT thick film bimorph MEMS cantilever device for vibration energy harvesting’. *Sensor Actuat A-Phys.* (2012), vol. 188: pp. 383–388.

117. Lei, A. et al.: ‘MEMS-based thick film PZT vibrational energy harvester’. *IEEE 24th International Conference on Micro Electro Mechanical Systems (MEMS).* 2011: pp. 125–128.

118. Aktakka, E. E. et al.: ‘Thinned-PZT on SOI process and design optimization for piezoelectric inertial energy harvesting’. *16th International Conference on Solid-State Sensors, Actuators and Microsystems (TRANSDUCERS).* 2011: pp. 1649–1652.

119. Lord, D. G. et al.: ‘Optical observation of closure domains in terfenol-D single crystals’. *IEEE Trans. Magn.* (1988), vol. 24(2): pp. 1716–1718.

120. Wittborn, J. et al.: ‘Magnetic domain and domain-wall imaging of submicron Co dots by probing the magnetostrictive response using atomic force microscopy’. *Appl. Phys. Lett.* (2000), vol. 76(20): pp. 2931–2933.

121. Tomiczek, A. E. et al.: ‘Characterization of composite materials with giant magnetostriction’. *Arch. Mater. Sci. Eng.* (2014), vol. 65(1).

122. Meier, T. et al.: ‘A scanning probe microscope for magnetoresistive cantilevers utilizing a nested scanner design for large-area scans’. *Beilstein J. Nanotechnol.* (2015), vol. 6(1): pp. 451–461.

123. Atulasimha, J. et al.: ‘A review of magnetostrictive iron–gallium alloys’. *Smart Mater. Struct.* (2011), vol. 20(4): p. 043001.

124. Holden, AP et al.: 'Surface deformations and domains in Terfenol-D by scanning probe microscopy'. *Journal of applied physics* (1996), vol. 79(8): pp. 6070–6072.

125. Papageorgopoulos, AC et al.: 'Magnetostriction measurements with atomic force microscopy: a novel approach'. *Journal of Magnetism and Magnetic Materials* (2004), vol. 268(1-2): pp. 198–204.

126. Harin, EV et al.: 'Atomic force microscopy measurements of magnetostriction of soft-magnetic films'. *Solid State Phenomena.* Vol. 190. Trans Tech Publ. 2012: pp. 179–182.

127. Jin Park, Jung et al.: 'Technique for measurement of magnetostriction in an individual nanowire using atomic force microscopy'. *Journal of Applied Physics* (2014), vol. 115(17): 17A919.

128. Naifar, Slim et al.: 'Investigation of the magnetostrictive effect in a terfenol-D plate under a non-uniform magnetic field by atomic force microscopy'. *Materials and Design* (2016), vol. 97: pp. 147–154.

129. Shindo, Y. et al.: 'Nonlinear bending response of giant magnetostrictive laminated actuators in magnetic fields'. *J. Mech. Mater. Struct.* (2009), vol. 4(5): pp. 941–949.

130. Alexander, J. H. et al.: 'Microstructure properties and strengthening mechanisms of the AS4-3501-6 polymeric resin with embedded terfenol-d particles'. *Conference on Smart Materials, Adaptive Structures and Intelligent Systems ASME.* 2014: V001T05A014–7699.

131. *Terfenol-D Magnetostrictive Actuator Information, Specifications, Public domain.* http://www.etrema.com/. 2016.

132. Jiles, D.: *Introduction to magnetism and magnetic materials.* CRC press, 2015.

133. *Nonlinear Magnetostrictive Transducer.* https://www.comsol.com/model/nonlinear-magnetostrictive-transducer-6063. Accessed: 10 01 2014. 2014.

134. Naifar, S. et al.: 'Modeling and simulation of magnetostriction in a twin lateral transducers energy harvester'. *11th International Multi-Conference on Systems, Signals and Devices (SSD).* 2014: pp. 1–5.

135. Erturk, A. et al.: *Piezoelectric energy harvesting.* John Wiley and Sons, 2011.

136. Kim, J. et al.: 'Evaluation of All the Material Constants of PMN-28% PT Piezoelectric Single Crystals for Acoustic Transducers'. *Sens. Mater* (2013), vol. 25: pp. 539–552.

137. *Piezoelectric single crystal.* http://www.jfe-mineral.co.jp/e$_mineral/seihin/esei-hin$034*.html*. Accessed 06 01 2017.

138. Viehland, D. D. et al.: 'Young's modulus and hysteretic losses of 0.7 Pb (Mg1/3Nb2/3) O-3-0.3 PbTiO (3): single versus polycrystalline forms'. *J. Appl. Phys.* (2003), vol. 94(12).

139. Skulski, R. et al.: ‘The electrical conductivity of PMN-PT ceramics’. *Arch. Metall. Mater.* (2009), vol. 54: pp. 935–941.

140. Butler, J. L. et al.: *Transducers and arrays for underwater sound.* Springer, 2007.

141. Hooker, M. W.: ‘Properties of PZT-Based piezoelectric Ceramics between -150 and 250 C’. (1998), vol.

142. Nayfeh, A. H. et al.: ‘Forced oscillations of systems having a single degree of freedom’. *nonlinear oscil.* (1979), vol.: pp. 161–257.

143. Marinca, V. et al.: *Nonlinear dynamical systems in engineering: Some approximate approaches.* Springer Science and Business Media, 2012.

144. Stokey, William F: ‘Vibration of systems having distributed mass and elasticity’. *Shock and vibration Handbook* (1988), vol.: pp. 7–1.

145. Naifar, Slim et al.: ‘Survey of electromagnetic and magnetoelectric vibration energy harvesters for low frequency excitation’. *Measurement* (2017), vol. 106: pp. 251–263.

146. Yang, F. et al.: ‘Magnetoelectric response of magnetostrictive/piezoelectric/-magnetostrictive laminate composite’. *2006 IEEE International Conference on Information Acquisition.* 2006: pp. 1010–1014.

147. Schröder, T. J.: ‘Realisierung eines Messplatzes für die Charakterisierung von Vibrationswandlern’. MA thesis. Technische Universität Chemnitz, 2014.

148. Iijima, Sumio: ‘Helical microtubules of graphitic carbon’. *nature* (1991), vol. 354(6348): p. 56.

149. Zhang, Mei et al.: ‘Carbon nanotube in different shapes’. *Materials today* (2009), vol. 12(6): pp. 12–18.

150. O’connell, Michael J: *Carbon nanotubes: properties and applications.* CRC press, 2006.

151. Thostenson, Erik T et al.: ‘Advances in the science and technology of carbon nanotubes and their composites: a review’. *Composites science and technology* (2001), vol. 61(13): pp. 1899–1912.

152. Berger, Claire et al.: ‘Ballistic conduction in multiwalled carbon nanotubes’. *Journal of nanoscience and nanotechnology* (2003), vol. 3(1-2): pp. 171–177.

153. Nishijima, Hidehiro et al.: ‘Novel process for fabricating nanodevices consisting of carbon nanotubes’. *Japanese Journal of Applied Physics* (1999), vol. 38(12S): p. 7247.

154. Bolotin, V. V.: *Mechanics of fatigue.* Vol. 11. CRC Press, 1999.

155. S., Mateusz: *Which Fatigue Model Should I Choose.* https:// www.comsol.com/-blogs/fatigue-model-choose/. Accessed: 10 01 2017. 2014.

156. Mateusz, S.: *Random Load Fatigue.* https://www.comsol.com/blogs/random-load-fatigue/. Accessed: 10 01 2017. 2013.

157. Zhang, Y. et al.: ‘Fatigue behavior of ferroelectric ceramics under mechanically–electrically coupled cyclic loads’. *Mater. Sci. Eng: A* (2003), vol. 351(1): pp. 81–85.

158. Hashin, Z.: ‘A reinterpretation of the Palmgren-Miner rule for fatigue life prediction’. *J. Appl. Mech.* (1980), vol. 47(2): pp. 324–328.

List of Figures

List of Tables

Scientific Reports on Measurement and Sensor Technology

1. Bouchaala, Dhouha (2016)
Investigation of Current Excitation for Personal Health and Biological Tissues Monitoring
ISBN 978-3-941003-96-9
Volltext: `http://nbn-resolving.de/urn:nbn:de:bsz:ch1-qucosa-204801`

2. Heidary Dastjerdi, Maral (2016)
Ein Beitrag zur Verbesserung der Eigenschaften magnetisch-induktiver Tastspulen
ISBN 978-3-944640-98-3
Volltext: `http://nbn-resolving.de/urn:nbn:de:bsz:ch1-qucosa-207628`

3. Guermazi, Mahdi (2016)
In-Vitro Biological Tissue State Monitoring based on Impedance Spectroscopy
ISBN 978-3-96100-003-6
Volltext: `http://nbn-resolving.de/urn:nbn:de:bsz:ch1-qucosa-206710`

4. Viehweger, Christian (2017)
Modellbasiertes Energiemanagement für die intelligente Steuerung solarversorgter drahtloser Sensorsysteme
ISBN 978-3-96100-022-7
Volltext: `http://nbn-resolving.de/urn:nbn:de:bsz:ch1-qucosa-224040`

5. Gerlach, Carina (2017)
Dispersionsoptimierung von Kohlenstoffnanoröhren für die Herstellung von Polymer-Komposit-Drucksensoren
ISBN 978-3-96100-025-8
Volltext: `http://nbn-resolving.de/urn:nbn:de:bsz:ch1-qucosa-226222`

6. Sanli, Abdulkadir (2018)
Synthesis and Characterization of Strain Sensitive Multi-walled Carbon Nanotubes/Epoxy based Nanocomposites
ISBN 978-3-96100-047-0
Volltext: `http://nbn-resolving.de/urn:nbn:de:bsz:ch1-qucosa-233763`

7. Weber, Christian (2018)
Entwicklung eines Verfahrens zur Anhaftungserkennung und Trennung von Einflussgrößen bei kapazitiven Näherungsschaltern mit Hilfe der Impedanzspektroskopie

ISBN 978-3-96100-056-2
Volltext: `http://nbn-resolving.de/urn:nbn:de:bsz:ch1-qucosa2-234856`

8. Benchirouf, Abderrahmane (2018)
Carbonaceous Nanofillers and Poly (3,4- ethylenedioxythiophene) Poly(styrenesulfonate) Nanocomposites for Wireless Sensing Applications
ISBN 978-3-96100-068-5
Volltext: `http://nbn-resolving.de/urn:nbn:de:bsz:ch1-qucosa2-319037`

9. Naifar, Slim (2019)
Model based Design of a Magnetoelectric Vibration Converter from Weak Kinetic Sources
ISBN 978-3-96100-079-1
Volltext: `http://nbn-resolving.de/urn:nbn:de:bsz:ch1-qucosa2-327748`